REDUCING UNCERTAINTIES IN AEROSOL OPTICAL PROPERTIES

WITH CAVITY RING-DOWN SPECTROSCOPY

by

JUSTIN RICHARD TOOLE

(Under the Direction of Geoffrey D. Smith)

ABSTRACT

The initial success of the Aerosol-Cavity Ring-Down Spectroscopy (A-CRDS) technique has led to recent investigations in particle morphology, aerosol mixtures, relative humidity effects, and even field studies. Uncertainties in aerosol extinction measurements are typically quoted as 1-10%; however, reported uncertainties assume the employed commercial instruments are absolutely accurate. Obtaining meaningful and precise measurements will require a complete understanding of the sources of error as instruments begin to reach their limits. An A-CRDS system was developed to improve precision and accuracy in aerosol optical property measurements with a novel calibration procedure. Scattering and absorption components of the complex refractive index are retrieved with the highest confidence level reported to date. This technique addresses systematic errors in commercial instruments and the inability to precisely characterize aerosol flows through the optical cavity. Further, this calibration method is shown to reduce absolute errors in the extinction measurements to less than 1%.

INDEX WORDS: aerosol, cavity ring-down, optical properties, refractive index, extinction cross section, squalane, squalene, dioctyl sebacate, oleic acid, differential mobility analyzer, electrostatic classifier, condensation particle counter

REDUCING UNCERTAINTIES IN AEROSOL OPTICAL PROPERTIES WITH CAVITY RING-DOWN SPECTROSCOPY

by

JUSTIN RICHARD TOOLE

B.S. North Georgia College and State University, 2003

M.S. Missouri University of Science and Technology, 2008

A Thesis Submitted to the Graduate Faculty of The University of Georgia in Partial Fulfillment of the Requirements for the Degree

MASTER OF SCIENCE

ATHENS, GEORGIA

2012

REDUCING UNCERTAINTIES IN AEROSOL OPTICAL PROPERTIES WITH CAVITY RING-DOWN SPECTROSCOPY

by

JUSTIN RICHARD TOOLE

Major Professor: Geoffrey D. Smith

Committee: I. Jon Amster
Gary E. Douberly

Electronic Version Approved:

Maureen Grasso
Dean of the Graduate School
The University of Georgia
May 2012

DEDICATION

I dedicate this work to my family, near and far, whom I love unconditionally. In particular, my wife kept me well-fed and smiling through the past 18 months, and she will always be at the forefront of my life regardless of the hours we spend apart. Finally, my daughters remind me to keep asking questions but never take the answers too seriously.

ACKNOWLEDGEMENTS

This work would not have been possible without months of groundwork laid by the initial investigations of Geoff Smith and Lindsay Renbaum-Wolff. Geoff unequivocally cares about his students and treats them with the utmost dignity and respect. Enough gratitude cannot be expressed for Geoff's professionalism and sense of humor. Lindsay's willingness to help me before and after I joined the project and her undeniable commitment to her research inspired me to complete this work. Finally, some of the experimental data used herein was collected by several others who deserve acknowledgement. Kimberly Schuldt collected a portion of the Snell's Law cell and Cavity Ring-Down measurements. Gareth Sheppard and Jason Locklin were generous enough to offer their instruments and expertise in the collection of ellipsometry data. Finally, the ellipsometry measurements reported herein were made by Jeremy Vanderslice at J.A. Woollam, Inc.

TABLE OF CONTENTS

Page

LIST OF TABLES

Page

LIST OF FIGURES

Page

CHAPTER 1

UNDERSTANDING THE EFFECT OF AEROSOLS IN THE ATMOSPHERE

1.1 The current perspective on the earth's radiative balance

The earth's atmosphere is divided into regions that form layers around the earth with respect to their altitude. From the thermosphere that is hundreds of miles from the earth's surface to the lowest troposphere where nearly all of earth's water exists, drastic changes in temperature, pressure, and composition make for unique interactions with solar radiation. In between these two layers, the stratosphere is well known for containing the higher concentrations of ozone where much of the sun's UV radiation ($\lambda < 290$ nm) is absorbed. For centuries, observations and studies have attempted to better understand the chemical and physical processes occurring throughout the earth's atmosphere[1]. Within the past several decades, scientific evidence has given rise to climate models that account for many natural and anthropogenic systems [2, 3]. These models have advanced from crude simplifications to an increasingly refined picture that now includes geography, wind and ocean currents, and limited atmospheric chemistry. It would be naïve to assume that all atmospheric conditions could ever be exactly understood, but current studies aim to reduce the uncertainties in contributors of the global radiative balance. There is no doubt that maintaining a long-term radiative balance will be required to maintain a climate amenable to life on earth.

From the effects of natural smoke and ash from a volcanic eruption to the anthropogenic air pollution in industrial regions, aerosols in the atmosphere are a significant variable in the earth's radiative balance. Aerosols are an example of a colloidal system in which solid or liquid

particles are dispersed within a surrounding medium in the gas phase. Aerosols range in size from a few nanometers to visible sizes of ten microns or more. Some particles are suspended in the air for days or weeks, so the potential for "aging" through chemical reactions is also important in characterizing the influence of particulate matter [4]. The net effect of aerosols on the climate is complicated by the various processes in which particles are involved. As depicted in Figure 1.1[3, 5-8], solar radiation (i.e. ≈300-2500 nm) is influenced by aerosols directly and indirectly through several mechanisms.

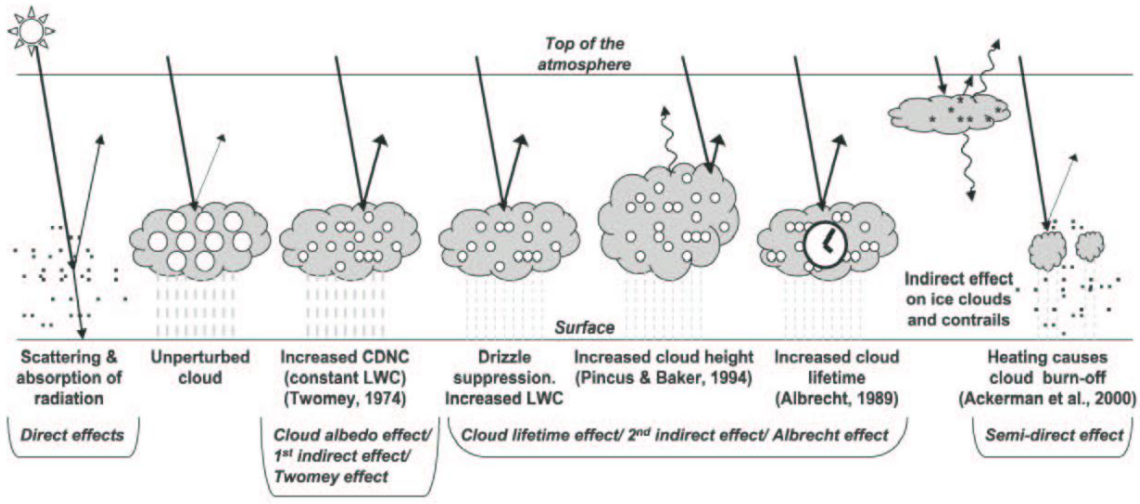

Figure 1.1. Several interactions of solar radiation and aerosols that influence the earth's radiative balance.

In recent years, attention has shifted from the role of aerosols (particularly black carbon) as a pollutant to the importance of light absorbing and scattering effects on global warming [9, 10]. Light absorbing aerosols will heat their surroundings by converting electromagnetic energy into thermal energy, and scattered light will generally produce a cooling effect[11]. The important question is not whether humans play a role in these atmospheric processes but rather how much and to what extent will this affect regional and global climate. The metric used to measure the global energy balance is radiative forcing (W m^{-2}) where a positive forcing indicates net heating.

Figure 1.2 shows the relative impact of individual anthropogenic and natural radiative forcing terms. The importance of reducing uncertainties in aerosol influences can be appreciated as the respective uncertainties of the two aerosol effects (direct and cloud albedo) are larger than their respective estimates. Also, the total uncertainty from aerosols is larger than the combination of all other anthropogenic radiative forcing measurements.

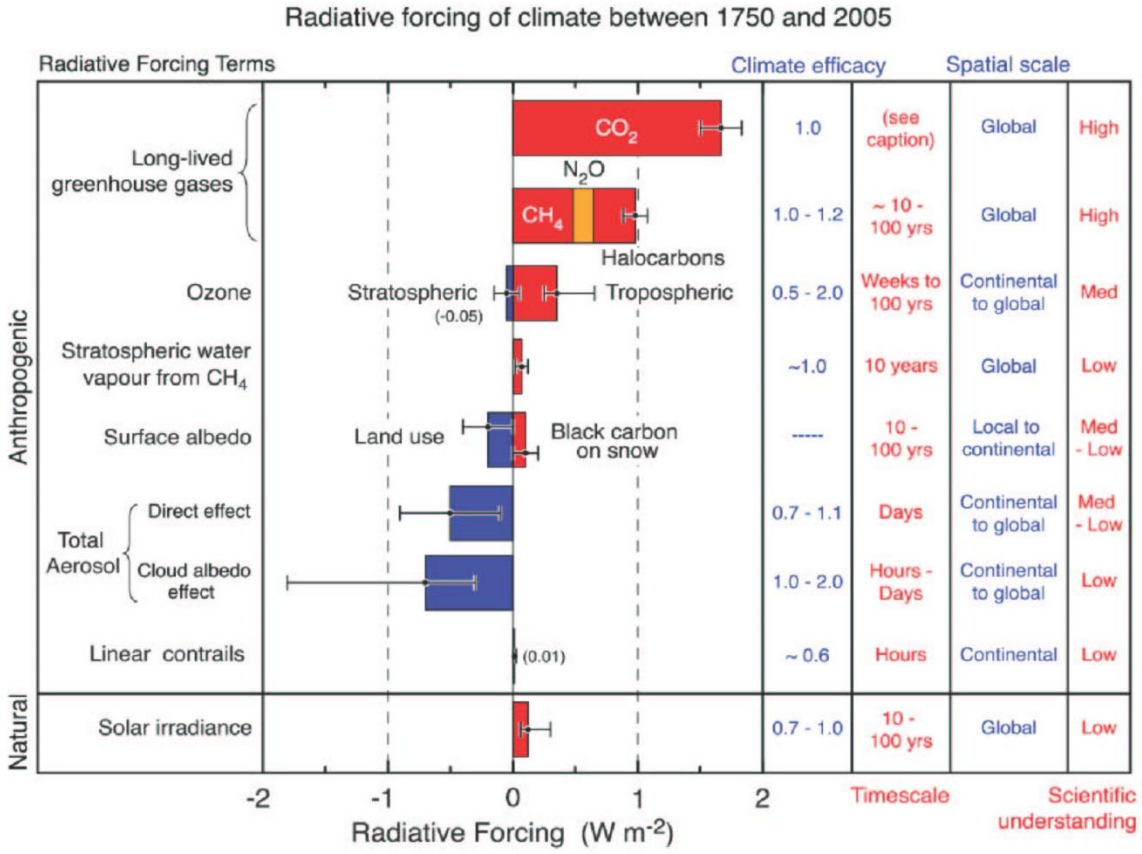

Figure 1.2. Net radiative forcing of anthropogenic and natural sources. Note the terms with the largest uncertainty are due to aerosol effects.

Climate effects will also depend on the residence time of the suspended particle and the distribution in the atmosphere[12]. The understanding of light scattering and absorption of aerosols in the atmosphere is critical for quantifying the resulting climate effects and to improve future models. By benchmarking standard models for scattering and absorbing aerosols,

experimental measurement will reduce uncertainties in the radiative forcing of aerosol influences. The goal normally is to measure optical properties accurately as they are easily parameterized into climate models.

1.2 The aerosol direct effect

The refractive index of the gas dispersion medium is approximately unity, so the refractive index of the aerosol particle is always much larger and characterized by optical scattering. The complex refractive index has a real phase velocity component and an imaginary attenuation component defined by

$$m = n + ik \tag{1.1}$$

where n is the real, scattering component and k is the imaginary, absorption component. The two terms, n and k, will account for the total light extinction (normally reported in cm^{-1}). In some cases, such as with atmospheric soot or black carbon, the absorption may be a significant portion of total light extinction, but normally the vast majority of aerosol extinction results from scattering. The extinction cross section is comprised of scattering and absorption cross sections where

$$\sigma_{ext} = \sigma_{sca} + \sigma_{abs} \tag{1.2}$$

If the cross section is considered as a shadow being cast as light passes through the particle, the wavelength and particle size will play a role in the effective area of this projected shadow. Optical scattering is observed when the particle is orders of magnitude larger than the wavelength of light, and Rayleigh-Gans scattering theory describes the interaction when particles are much smaller than the wavelength. In the regime where the wavelength and particle diameters are comparable in size, such as 20 nm – 2 μm particles and solar radiation, Lorenz-Mie theory can predict the scattering and absorption portion of the extinction. This theoretical

solution requires that the particle is spherical and homogenous, yet it has been experimentally verified for the past century to appropriately model this interaction [13].

It is worth mentioning here that the theoretical extinction for a particle will depend on its size, morphology, and refractive index at a single wavelength of light. For some species, absorption increases for a given particle size as the radiation energy increases (i.e. shorter wavelengths), and purely scattering aerosols in the visible spectrum might have some absorbance in the UV. The increasing absorption trend in the UV calls into question whether extrapolations of optical property measurements appropriately model the direct aerosol effect for the entire solar spectrum.

This is a concern for light-absorbing organic matter, also called "brown" carbon, that is commonly found in aerosols. Possible sources of brown carbon are soil humics, humic-like substances, tarry materials from combustion, and biomass burning[14]. Brown carbon optical properties deserve additional study because a significant fraction of it is soluble in water and could underestimate modeled absorption of light for cloud droplets[15]. Current optical measurements of brown carbon and other aerosol species suffer from several problems. First, there is no accurate predicting light absorption from elemental composition. Second, the complex morphology and composition of ambient aerosols is difficult to reconcile conceptually and practically. Finally, many of the current techniques that measure extinction introduce a substantial bias[14]. The improved measurement of extinction and the optical constants for aerosols will, at a minimum, improve the understanding of the direct effects of atmospheric particles on the global radiative balance.

1.3 Measurement of aerosol optical properties

Quantitatively measuring aerosol light scattering and absorption is still a challenge in both laboratory and field studies. As expected, there is no "silver bullet" technique or instrument that can sensitively and accurately measure scattering and absorption coefficients for a wide range of aerosol concentrations with immediate time response. A combination of techniques are necessary to span the range of ambient conditions, and discrepancies between techniques must be reconciled to offer information about an aerosol's true interaction with light[14, 16]. Light absorption can be determined by the so-called "difference method" where the extinction and scattering of a sample are measured with separate techniques and the absorption component is calculated as the difference. This approach is useful as long as the uncertainty of each measurement is not greater than the calculated absorption, and this is often the case for slightly and moderately absorbing aerosol species.

Aerosol light absorption techniques can be divided into two types of methodologies: 1) filter deposition and analysis and 2) *in situ* measurements of the naturally suspended aerosol [17]. Filter based techniques involve collection of aerosols on a particle filter for off-line extraction or direct comparison of to the transmission of the loaded filter to a filter blank. The flow rate per filter area over a length of time can be used to evaluate the total volume of sample air that contained the suspended particles. Unfortunately, this technique is plagued with approximations and assumptions that make precise optical measurements cumbersome. For example, the attenuation of light through the collected particulate matter is a result of both absorption and scattering, and it is impossible to parse out the light extinction with a standard Beer's Law transmission measurement. To a degree this effect can be minimized by immersing the collected filter sample in a substance with a similar refractive index as the filter medium[18]; however,

Table 1.1. Comparison of techniques that measure aerosol extinction, scattering, and absorption.

Technique / Instrument	Principle and measurement	Advantages	Disadvantages
Filter-based collection and analysis (e.g. Aethalometer, Particle Soot Absorption Photometer, and Multi-Angle Absorption Photometer)	Particulate matter is deposited on a filter and absorption is determined with transmission measurements	Real-time measurements at multiple wavelengths. Simply, cheap, and no influence of carrier gas	Particle loading errors from volatile and reacting species, sensitive to humidity and high organic carbon concentrations.
Photoacoustic Spectroscopy	Absorbing particles create a sound wave that is measured with a microphone	In situ technique with high sensitivity. Detectors are cheap and "colorblind."	Only absorption extinction is measured. Resonance cell requires precise dimensions and arrangement.
Integrating Nephelometer	Intensity of scattered light is measured over an integrating surface.	In situ measurements at multiple wavelengths. Commercially available.	Large correction factors. Truncation angle prevent detection of all scattered light.
Integrating Sphere	Collection of scattered light within a highly reflective sphere	In situ measurement that can be combined with CRDS for the same sample volume.	Similar to the nephelometer.
Cavity Ring-Down Spectroscopy (CRDS)	Extinction is measured in an optical resonator by a change in exponential decay time.	Simple design, absolute in situ measurement, and high sensitivity.	Fixed wavelength.
Remote Sensing (LIDAR, radiometers, and satellite measurements)	Effective extinction values are measured for a large sample volume	Characterizes aerosol types well and determines particle distributions well. Global coverage.	Cannot distinguish scattering from absorption. No spatial information

this still presumes that all the collected particles will have a similar scattering component which is not true for ambient samples with highly absorbing species such as black carbon. Also, the filter deposition measurements will offer little to no information as to the particle morphology, the interactions between collected layers, and time resolution within the sample period. Real-time filter instruments with instruments such as aethalometers have been developed to continuously measure the aerosol absorption coefficient from the temporal change in

transmission [19, 20]. Regardless of the technique, filter-based analysis will always be prone to artifacts as the aerosol is removed from the suspended state and concentrated on filter medium. Even in a well-conducted study, several filter-based measurements of a biomass smoke were compared with, at best, more than 20% difference in calculated absorption coefficients[21].

Though filter-based instruments are simple, cheap, and insensitive to influences of the carrier gas, a less intrusive method is to measure the absorption directly or indirectly *in situ*. Examples include photoacoustic, remote sensing, refractive index-based and incandescence techniques[17]. The only instrument that measures light absorption of an aerosol directly is the photoacousitc spectrometer (PAS)[22-25]. Briefly, photoacoustic spectroscopy quantifies light absorption of gases and aerosols through conversion of light energy to sound. Upon absorption, heat transfer to the surrounding air will create a pressure gradient which manifests itself as a propagating sound wave. A microphone detector is placed along the resonating cell and is coupled to a modulated light source so that absorption measurements are collected immediately for a sample of aerosol as it flows through the cell. The PAS has excellent detection limits with rapid time response (<0.1 Mm^{-1} for 60 s measurement)[26], but it only gathers information about absorbing species. If a complete picture of an aerosol's interaction with light is desired, PAS must be combined with other techniques that quantify scattering or measure total extinction. Comparison studies with PAS and optical extinction cells have shown excellent agreement for absorption of soot, biomass smoke particles, and ambient aerosols [27, 28] though it is less useful for typical atmospheric conditions where the extinction is dominated by scattering. When scattering dominates the extinction, obtaining the absorption coefficient with the difference method results in unacceptably large errors because it compares small differences in two larger numbers.

Laboratory comparisons using the difference method indicate that PAS techniques can determine aerosol absorption with an accuracy <10%[24, 29, 30].

Another instrument used in conjunction with absorption techniques is the nephelometer. Nephelometry is unique in that is determines the scattering coefficient, normally at three wavelengths (450, 550, and 700 nm), by directly measuring the scattering of airborne particles and integrating the detected light over nearly all angles [31, 32]. Though nephelometry is independent of particle composition and morphology, it must introduce a "truncation correction" to account for a portion of the undetectable back- and forward-scattered light. Also, absorption by particles changes the wavelength dependence of the correction by as much as 5%[33], and the calibration errors are particularly large for weakly absorbing substances with a strong wavelength dependence such as brown carbon. Variable correction factors and the additional uncertainty from extrapolation of the scattering coefficients at other wavelengths limit the precision of the nephelometer for absorbing species.

One technique that is unique in its ability to measure total extinction without the need for calibration is cavity ring-down spectroscopy (CRDS). CRDS requires a relatively simply design, delivers high sensitivity with minimal sampling time, and can be used to make *in situ* measurements of aerosols and trace gases[34, 35]. As such, many studies in the early 1990's used this technique as a sensor for trace gases in the atmosphere with parts per billion sensitivity[36-39]. Studies have progressed to measuring laboratory and ambient aerosols by continuously flowing a stream of particles through an optical cavity (CRD cell). It is possible to extract the scattering and absorption coefficients from the total extinction if a series of measurements are made for a homogenous aerosol. From these measurements, retrieving a complex refractive index of the aerosol is possible if the particles are assumed to be spherical

and their size distribution is known. A set of extinction measurements for varying particles sizes will correspond to a unique extinction curve. By comparing the aerosol cavity ring-down spectroscopy (A-CRDS) extinction measurements to Mie theory predictions, a complex refractive index can be retrieved that corresponds to a best fit combination of n and k. For current A-CRDS studies, the typical uncertainty in the real and imaginary components of the retrieved refractive index is on the order of one to two percent and ten to several hundred percent, respectively[40].

1.4 Goals of this work

Questions still remain as to the net effect of ambient aerosols on radiative forcing and global climate patterns, and measurements of the aerosol extinction, absorption, and scattering cross sections will help to better understand their role. Brown carbon substances are of particular interest due to their light absorption properties and relative abundance in continental aerosol[15, 41], and this highlights the need for more accurate and precise optical property measurement of these species. Uncertainties in refractive indices, particularly at lower visible and UV wavelengths, are large enough such that optical property extrapolations may result in poor approximations. At the outset of this project, the goal was to more precisely measure absorption and scattering coefficients of organic matter with a UV A-CRDS system. A better understanding of how oxidation and "aging" processes affect the refractive index of evolving organic substances would aid in improving climate models. To this end, the A-CRDS system has been exhaustively studied to achieve levels of precision not yet reported in the literature. Instrument accuracy has been improved such that uncertainty in the retrieved real and imaginary components of the refractive index is reduced by an order of magnitude ($< \pm 0.01$ with 95% confidence). This level of precision in extinction measurements will be necessary to differentiate

between purely scattering substances and ones with slight absorption. Extinction measurements were made exclusively at 355 nm; however, the developed experimental and computational techniques are applicable at any wavelength. These contributions will help advance the state-of-the art in measuring aerosol optical properties and address an outstanding need as expressed in a recent paper: "While it has been demonstrated that [A-CRDS] is capable of measuring extinction and scattering to within a few percent, improvements should be made to reduce error to within a few tenths of percent. This level of accuracy and precision is needed to contribute meaningfully to radiative forcing and global climate models."[42]

CHAPTER 2

IMPROVED CALIBRATION OF AN AEROSOL CAVITY RING-DOWN SYSTEM

2.1. Introduction

The development of the Cavity Ring Down Spectroscopy (CRDS) technique by O'Keefe and Deacon in 1988[43] precipitated rapid progress in atomic and molecular absorption measurements. CRDS has been widely reviewed [44-48], and the key advantages of this direct absorbance technique originate from the long effective pathlengths (>1000 m) and insensitivity to shot-to-shot intensity fluctuations. Within months of its introduction the first aerosol extinction measurements were made using this new spectroscopic technique[36], and during the following decade CRDS received considerable attention in several fields for its ability to achieve absorption sensitivity better than 10^{-8} cm^{-1} with a relatively simple optical setup [48]. In 1998 the first Aerosol Cavity Ring Down Spectroscopy (A-CRDS) system was developed to measure the extinction of ambient particulate matter[49]. Though initial results were primarily qualitative, subsequent studies quantified the extinction of particles and gases using novel CRDS systems[50-54]. A-CRDS studies investigated the interaction of ambient particulate matter and solar radiation as much effort has been given toward reducing uncertainties in the direct effect of aerosols on the earth's radiative budget[2, 3, 55]. This technique is unique in atmospheric studies because it measures real-time *in-situ* optical extinction resulting from scattering and absorption processes.

The extinction of light as it interacts with aerosols occurs solely from scattering and absorption mechanisms and is described by the complex refractive index, m, (m = n + ik)[56],

where n is the real component attributable to scattering and k is the imaginary component attributable to light absorption. The magnitudes of these two optical constants depend on the wavelength of light, size, and morphology of the particle. Lorenz-Mie theory has been used extensively to compare experimental results by modeling scattering and absorption of light from a homogenous spherical particle. A theoretical size-dependent extinction curve can be calculated for aerosols of known size distribution given values for n, k, and illumination wavelength. Recent A-CRDS studies have investigated optical properties with pulsed[25, 42, 57-66] and cw[67-74] lasers by comparing measured particle extinction at several sizes to Mie theory predictions. With an ensemble of measurements with different size parameters (by varying particle size or the illumination wavelength[75]), computational fitting routines can retrieve a best fit complex refractive index as different values of n and k will yield unique extinction curves. The promising agreement between theory and experiment has led to refined studies of aerosols that have probed particle morphology[76, 77], internal and external particle mixing[26, 58, 62, 78-82], and effects of relative humidity[57, 64, 78, 83, 84]. However, the ability to use this technique effectively is predicated on the stability of the instrumentation and on the overall uncertainty associated in measuring the extinction. Extracting proper conclusions from increasingly sophisticated measurements will require better precision and fully understanding all sources of error as instruments begin to reach their certainty limits.

Recent studies have revealed that several sources of uncertainty in A-CRDS are usually underestimated or omitted altogether, and this influences the accuracy of the retrieved complex refractive index[40, 85]. Consideration of instrumental limitations is rarely addressed once cursory validation experiments show agreement with Mie theory and reference refractive index values. Validation of the A-CRDS is often limited to measuring the extinction of a single

reference substance, and few studies considered the uncertainty in the measurement of the bulk refractive index. Deviation from predicted Mie theory extinction measurements at a given particle size and distribution are typically reported from 1-10%[42, 53, 54, 63, 65, 67]; however, individual instrument specifications can limit certainty to 10% without proper calibration[86]. More sophisticated aerosol studies require higher precision in extinction measurements to make accurate and meaningful conclusions. To facilitate these future studies, the goal here is to retrieve values of n and k with precision < 0.01 by developing a comprehensive calibration technique in lieu of validation. To date, there has been little effort in accounting for systematic instrument errors in the A-CRDS system.

In this work, the impact of the uncertainty from the particle size and distribution, bulk refractive index, and particle counting efficiency is considering in making precise extinction measurements. The refractive index is reported at 355 nm for a purely scattering organic liquid, squalane, using several independent techniques with ±0.002 uncertainty. Using squalane as a reference standard, a novel fitting algorithm simultaneously retrieves a particle size distribution and instrumental calibration factors with associated 95% confidence limits. Finally, this method provides a unique approach for determining narrow particle size distributions (σ_{geo}< 1.06) of a commercial particle sizer (DMA, differential mobility analyzer).

2.2. Materials and methods

2.2.A. Bulk refractive index measurements. The real component of the refractive index (n) of liquid samples was measured using a custom Snell's Law cell as shown in Figure 2.1. An aluminum cell consisted of three quartz windows that transmitted 355 nm light through 4.5 cm of sample. The third harmonic of a Nd:YAG pulsed laser beam (Spectra-Physics Pro250, 10Hz, long pulse) was split and entered the cell through two separate angled windows. Careful

alignment of the back reflections of each incident beam ensured the light entered the cell normal to the front windows and exited at the same point on the rear window. Using Snell's Law, the ratio of the sines of the incident (θ_1) and refraction angle (θ_2) equal the ratio of n_1 and n_2 such that[56]

$$n_1 \sin(\theta_1) = n_2 \sin(\theta_2) \quad (2.1)$$

The angle of approach (θ_1) between the two incident beams was approximately 15.26^o, and the angle of refraction (θ_2) was determined by measuring the divergence of the two beams 2.91 m away from the exit window. Beam separations were measured with an empty and sample-filled cell assuming the refractive index of air is 1.000. Refractive index measurements of squalane (99%, Sigma Aldrich) and several solvents were taken at temperatures between 22.5-24.0 ^{o} C with uncertainty in n = ± 0.002.

Table 2.1. Measured and referenced refractive index values at 355 nm.

Substance	n_{355}	Technique	Reference[87, 88]
Water	1.347[ǂ]	Snell's Law Cell	This work
	1.348	GVM and Cauchy Dispersion	Kozma (2005)
Methanol	1.342[ǂ]	Snell's Law Cell	This work
	1.342	GVM and Cauchy Dispersion	Kozma (2005)
Ethanol	1.378[ǂ]	Snell's Law Cell	This work
	1.377	GVM and Cauchy Dispersion	Kozma (2005)
Isopropanol	1.393[ǂ]	Snell's Law Cell	This work
	1.393	GVM and Cauchy Dispersion	Kozma (2005)
Acetronitrile	1.359[ǂ]	Snell's Law Cell	This work
	1.358	GVM and Cauchy Dispersion	Kozma (2005)
Squalane	1.472[ǂ]	Snell's Law Cell	This work
	1.472	Kramers-Kronig analysis of reflectance measurements	Painter (1984)
	1.471	Ellipsometer	J.A. Woollam
	1.474	Refractometer and Cauchy Dispersion extrapolation	Sorensen (1951)
Immersion Liquid 1160	1.511+0.000i	Calibrated A-CRDS	This work
	1.515+0.000i[‡]	Refractometer and Cauchy Dispersion interpolation	Cargille Laboratories

[ǂ] Uncertainty is ±0.002 for all Snell's Law Cell measurements
[‡] Uncertainty for IL 1160 is reported by Cargille Laboratories as ±0.001 at 355 nm

Here the uncertainty was limited by the ability to determine the distance between the two diverged beam spots. Additionally, the complex refractive index of squalane was determined by measuring changes in light polarization of a liquid sample with spectroscopic ellipsometry[89]. A commercial ellipsometer (J.A. Wollam Co, M-2000V) was used to analyze a sample of squalane with 190 nm to 1700 nm polarized light at 2 nm intervals. For the purely scattering substances used, the Cauchy dispersion relation is used to fit the wavelength-dependent refractive index measurements to an empirical equation

$$n_\lambda = A + \frac{B}{\lambda^2} + \frac{C}{\lambda^4} \tag{2.2}$$

where n_λ is the wavelength in micrometers and A, B, and C are constants. For the squalane, A=1.4369, B=3.6776x10^{-3} μm^2, and C=8.2890x10^{-5} μm^4 with a measured temperature of 24^{o}C. These measurements at 355 nm were further corroborated by literature values by interpolating UV reflectance data (n_{355}=1.470)[88] and extrapolating standard refractometer measurements (n_{355}=1.474)[90]. A UV-Vis measurement of pure squalane confirmed that the absorption component (k) at 355 nm was orders of magnitude less than 0.001i and is assumed to be 0.000i for all calculations.

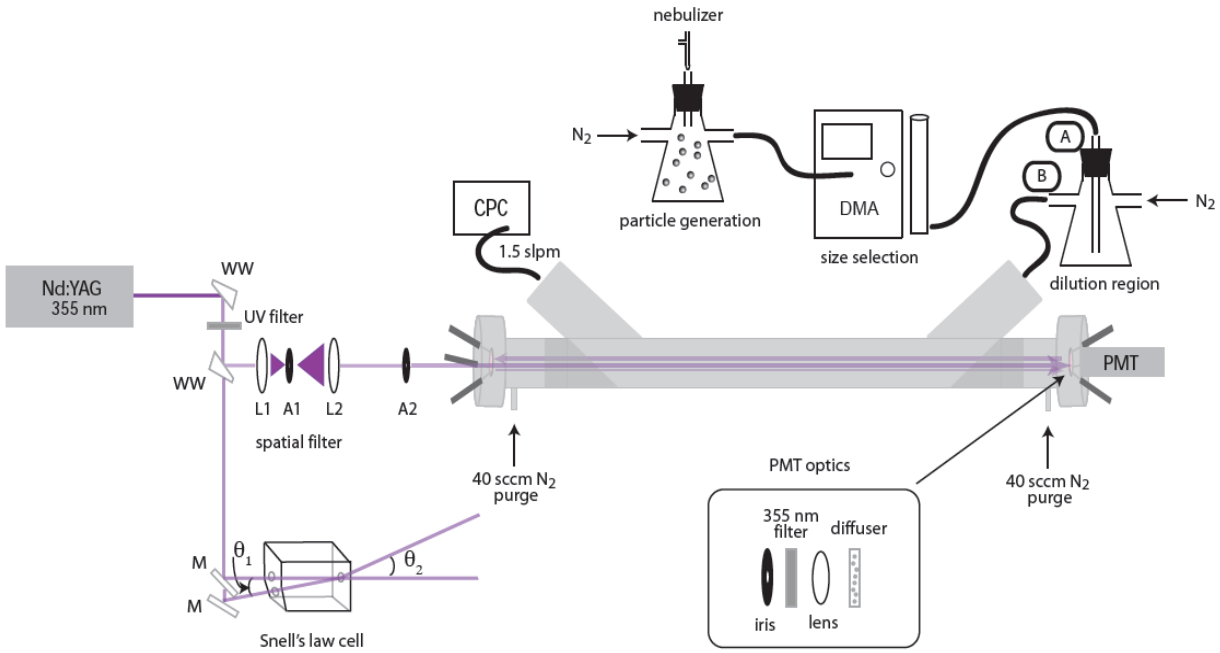

Figure 2.1. Experimental setup for the A-CRDS system and the Snell's Law Cell. WW = wedged windows, L1 = focusing lens, L2 = collimating lens, A1 = 100μm aperture, A2 = 1000μm aperture, and M = mirror.

2.2.B. Aerosol generation and size selection. A schematic diagram of the experimental setup is shown in Figure 2.1. Pure liquid samples were aerosolized by a concentric nebulizer (Type A, Environmental Express) with 0.30-0.35 LPM of dry nitrogen flow controlled by a Mass Flow Controller (MFC). The nebulizer produced a broad distribution of particle diameters between 0.05 and 1 μm that peaked at approximately 350 nm. This polydisperse aerosol was collected in a flask, and particles were drawn through an inertial impactor (0.0508 cm orifice) at a flow rate of 0.270 SLPM to eliminate larger particles. The calculated d_{50} cut-point (diameter at which only 50% of the particles penetrate the impactor) for these conditions is 995 nm[91]. A rotameter controlled an additional dilution flow into the nebulizing flask in order to select a suitable particle concentration and to prevent premature clogging of the impactor orifice. The

orifice was cleaned with methanol daily, and the impaction plate was wiped cleaned between each measurement.

The aerosol passed through a bipolar charger containing a 10mCi ^{85}Kr radioactive source (TSI 3077A) to apply an equilibrium charge distribution on the particles [92-95]. A narrow size distribution was generated with a Differential Mobility Analyzer (DMA; TSI 1080 Electrostatic Classifier) by passing particles of a selected electrical mobility[96] with a constant sheath flow of 2.7 SLPM. The DMA consists of an inner cylinder rod connected to a variable DC power supply and a grounded outer annular tube. Charged particles flowing along the cylinder are shifted radially as they traverse the electric field generated from the central rod. At the exit of the classifying region, only the portion of the aerosol consisting of the selected electrical mobility (Z_p) particles passes through a small exit slit. The monomobile aerosol was mixed in a 250mL flask and further diluted with 1.10 SLPM of dry nitrogen before flowing through the CRD cell. The sample flowrate was measured with a flowmeter (TSI 4140) between each measurement, and the final dilution flow was adjusted accordingly to achieve a consistent 0.270 SLPM aerosol flow into the DMA. Particle losses inside the cavity due to gravitational settling, inertial deposition, and diffusion are estimated as < 1% for 600-900nm particles[97], and this was confirmed by measuring average particle concentrations before and after the cell.

2.2.C. Particle counting. A butanol condensation particle counter (CPC; Model 3775, TSI) measured the particle concentration (N, cm^{-3}) exiting the cavity. The CPC enlarges particles to an optically detectable size by condensation through a region of supersaturated butanol vapor. The accuracy of the CPC is limited to 2% based on the uncertainty in the flow rate[54]; however, manufacturer specifications quote +/-10% accuracy[86]. The CPC inlet flow was maintained at 1.5 SLPM, and measurements were not recorded until flow equilibrium was reached with

concentrations ranging from 300 to 800 cm^{-3}. An empty cell ringdown time, τ_o, was recorded between each measurement once N averaged < 0.2cm^{-3} for a 120 s interval.

2.2.D CRD apparatus. The CRD sampling cell was constructed of a 1 m long ¾" diameter stainless steel tube with inlet and outlet ports at a 45° angle to permit a laminar aerosol flow through the cell. ¾" Teflon plugs with ¼" interior diameter where cut at 45° and inserted into the cell at the interior of the inlet and outlet ports. An optical cavity was formed with two highly reflective concave mirrors (Los Gatos Research, Inc., R = 99.97% at 365 nm, 20 mm diameter, 6 m radius of curvature), and mirror alignment was achieved by actuating a mirror mount against an o-ring with micrometer screws. A typical ring-down time (τ_o) of the cavity filled with dry N_2 was 2900 ns corresponding to a mirror reflectivity of 99.88% at 355 nm and an effective pathlength of 1 km. A Fast Fourier Transform (FFT) of the ring-down decay trace revealed a resonating longitudinal mode and free spectral range of 145.37 MHz corresponding to a distance between the mirrors of 103.1 cm (where $\Delta\upsilon = c/2L$)[98]. The extinction region (d) is limited to the linear portion of the beam occupied by particles assuming a laminar flow between the inlet and exit ports. With d = 88.2 cm, the ratio of the total cavity length to the occupied pathlength, R_L, was 1.169. A 40 sccm purge flow of dry N_2 was introduced at the face of each mirror to limit degradation of the mirror reflectivity from aerosol deposition, and effective particle concentrations were adjusted to account for dilution by this flow.

The third harmonic of the Nd:YAG laser emitted 8 ns laser pulses at 355nm at 10 Hz repetition. The laser pulse passed through a spatial filter consisting of a focusing lens (f = 5 cm), 100 μm pinhole aperture, and collimating lens (f = 2.5 cm). The spatial filter in conjunction with careful alignment of a 1000 μm iris and cavity mirrors promoted the excitation of the TEM_{00} mode of the cavity. Multi-exponential decay originating from off-axis alignment resulted

in mode beating and was monitored simultaneously on the oscilloscope with the FFT of the decay transient[99]. The laser pulse energy was attenuated to approximately 15 μJ before being coupled into the cavity.

2.2.E. Signal acquisition and processing. The decay time, τ, is a function of the round trip time for each pass (2L / c), the mirror reflectivities, and additional losses inside the cavity. Extinction due to particle scattering and absorption losses is determined by comparing the particle-free cavity decay time, τ_o, to the aerosol sample decay time, τ_{samp}, with

$$\alpha_{ext} = \frac{R_L}{c}\left(\frac{1}{\tau_{samp}} - \frac{1}{\tau_o}\right) \tag{2.3}$$

The exiting light passed through an optical bandpass filter, focusing lens, and diffuser and generated a current in the photomultiplier tube (PMT; Hamamatsu 6533) with a -1100V bias. Alignment of the detection system with an iris reduced noise associated with spatial differences in the quantum efficiency of the PMT. Ten decay transients were sampled at 200 MSa s^{-1} and averaged via an oscilloscope (HP 5483, 600 MHz, 50 Ω termination, 8 bit ADC). The digitized signal was transferred to a personal computer via GPIB for exponential fitting with the LRS (Linear Regression of the Sum) algorithm[100] in a custom LabVIEW program. Averaging ten decay events before the exponential fit increased the signal-to-noise ratio (SNR) and reduced the standard deviation of the decay time. The single-shot σ_τ was typically 1% of τ_o and 1.5% of τ_{samp} for a 1 second average.

The LRS and DFT-5 (Discrete Fourier Transform) algorithms were compared to the Levenburg-Marquardt fitting method in a series of real-time and off-line measurements. All three routines retrieved similar decay times, and LRS was selected because of its superior computational efficiency and reported noise immunity[101]. The extracted decay constant was

simultaneously retrieved for a 4τ region and several shorter (2 to 3τ) sub-regions for each decay event. Similar decay times for the full fit region and each comparison fit region indicated mono-exponential decay.

Finally, real-time extinction cross section measurements were collected by interfacing with the CPC (condensation particle counter) to collect particle concentrations, N, exiting the cavity to obtain

$$\sigma_{ext} = \frac{\alpha_{ext}}{N} \tag{2.4}$$

Averaging measurements for several minutes was required to obtain consistent cross section coefficients. Each reported σ_{ext} measurement was the average of four or more 120 s measurements of the selected particle diameter.

2.2.F. Fitting routine. Two fitting routines were developed to obtain a best fit for three calibration parameters and a complex refractive index, respectively, based on the experimental data. Both fitting algorithms used a chi-square method, χ^2, to evaluate how well the experimental σ_{ext} measurements compared to corresponding theoretical values, σ_{Mie}. χ^2 was evaluated for a range of fitting parameters to quantify the goodness-of-fit at incremental steps. χ^2 was determined by

$$\chi^2 = \sum_{i=1}^{N} \frac{(\sigma_{exp} - \sigma_{Mie})_i^2}{\varepsilon_i^2} \tag{2.5}$$

where the uncertainty in each measurement,ε_i, is taken as twice the standard deviation of the σ_{exp} measurement. The minimum evaluation, χ_o^2, is deemed the best fit for the given combination of fitting parameters. The first routine requires a precisely known complex refractive index such that any deviations from Mie predictions are assumed to be a result of the A-CRDS system. This method was used to simultaneously retrieve three calibration parameters: an extinction

calibration factor (C_f), particle diameter shift (Δ_{diam}), and size distribution (σ_{geo}, geometric standard deviation). C_f linearly scales all measured cross section measurements and accounts for inaccuracies from the CPC counting efficiency, determination of R_L, and inhomogeneity of the aerosol flow. The Δ_{diam} and σ_{geo} parameters are primarily a function of the DMA and address an offset in the selected modal diameter and assumed size distribution being output from the instrument. Δ_{diam} shifts all σ_{ext} measurements in the size domain and σ_{geo} varies the distribution at the modal diameter. For each of the parameters, a range of values ($0.8 \leq C_f \leq 1.1$; $-50 \leq \Delta_{diam} \leq 50$; $1.02 \leq \sigma_{geo} \leq 1.06$) and incremental step size ($C_f \pm 0.001$; $\Delta_{diam} \pm 1$nm; $\sigma_{geo} \pm 0.001$) was input such that an evaluation point occurred at each step within the three parameter ranges. Each evaluation point lies within a three-dimensional region defined by the range of values for each parameter. Chi-square boundaries within this three parameter domain can establish confidence limits by comparing the magnitude of each χ^2 to χ_o^2. A boundary with 95% confidence and one degree of freedom contains all combinations of C_f, Δ_{diam} and σ_{geo} values where $\chi^2 < 3.84 + \chi_o^2$[102].

The second fitting algorithm was similar to that reported by others[25, 40, 58, 60-62, 74, 75, 77, 81, 85] and compared experimental cross section measurements, σ_{ext}, to theoretical predictions, σ_{Mie}, using a Mie extinction calculator in a Mathematica script[103]. The second algorithm was necessary to confirm that the fitted calibration parameters in fact fit the experimental data to squalane's refractive index, but it is also required to retrieve complex refractive indices of other substances. Evaluations of χ^2 occurred at all selected combinations of n and k to retrieve a best fit complex refractive index. Normally, n and k were incrementally varied by 0.001 from 1.300 to 1.600 and 0.000i to 0.050i, respectively. Inherent in these algorithms is the assumption that monochromatic light is interacting with homogenous spherical

particles, particle size distributions are log normal, and the measurement errors are normally distributed.

2.3. Results and discussion

2.3.A. Sensitivity and detection limits. Extinction cross section, σ_{ext}, is taken as the ratio of the measured α_{ext} to the particle concentration, N, for a selected particle diameter and size distribution as defined in Equation 4. The extinction detection limit of the instrument is measured by the ability to differentiate between τ and τ_o where the $\Delta\tau_{min}$ is normally taken as the standard deviation of the empty cell decay time[104].

$$\alpha_{min} = \frac{R_L}{c}\left(\frac{\sqrt{2}\Delta\tau_{min}}{\tau_o^2\sqrt{RT}}\right) \tag{2.6}$$

Here, R is the repetition rate and T is the sampling time. For a one second average and $\Delta\tau_{min}$ of 10 ns, the detection limit for this instrument was $2.1\text{x}10^{-8}$ cm^{-1}. It has also been shown that statistical fluctuations in the number of particles in the laser beam volume may dominate the decay time variation at low particle concentrations[54]. Using Gaussian beam theory[98], the calculated beam volume here is 0.135 cm^3, and particle concentration would need to be less than 100 cm^{-3} in order for statistical fluctuations to account for more than 1% of the total uncertainty. Particle concentrations were maintained between 300 and 1000 cm^{-3} for all reported measurements. Higher repetition rates or longer sampling times will improve sensitivity at the expense of losing the shot-to-shot intensity invariance of CRDS. Likewise, purchasing more highly reflective mirrors will improve the detection limit only if the ratio of $\Delta\tau_{min}$ to τ_o^2 is reduced. Yet the ability to differentiate σ_{ext} will also depend on sources of error from the studied aerosol such as the uncertainty in the measurement of R_L (the ratio of optical and particle pathlength), the inaccuracy in the particle concentration measurement, and uncertainty in particle diameter. A critical review of A-CRDS sources of errors and uncertainties has shown that

characterization of the aerosol dominates the uncertainty in an extinction measurement and can lead to errors in a retrieved refractive index by 2% or more[40]. For example, the quoted accuracy of a typical commercial condensation particle counter (CPC) is ±10%, and the over- or under-counting of the CPC will linearly scale the calculated σ_{ext}. These uncertainties clearly necessitate careful calibration of the entire A-CRDS system if precise extinction measurements are desired.

Proper characterization of an aerosol is possible by first calibrating with reference aerosol particles of known complex refractive index and size distribution. First, we will consider the importance of precise σ_{ext} measurements in retrieving an accurate complex refractive index by examining the effect of uncertainties associated with the reference aerosol. Figure 2.2A depicts a calculated extinction curve of sub-micron spherical particles with a complex refractive index of 1.47+0.00i. This base curve (solid line) is representative of a purely scattering organic liquid, and the monodisperse size distribution is displayed as a geometric standard deviation (σ_{geo} = 1.05) typical of the DMA used in these experiments.

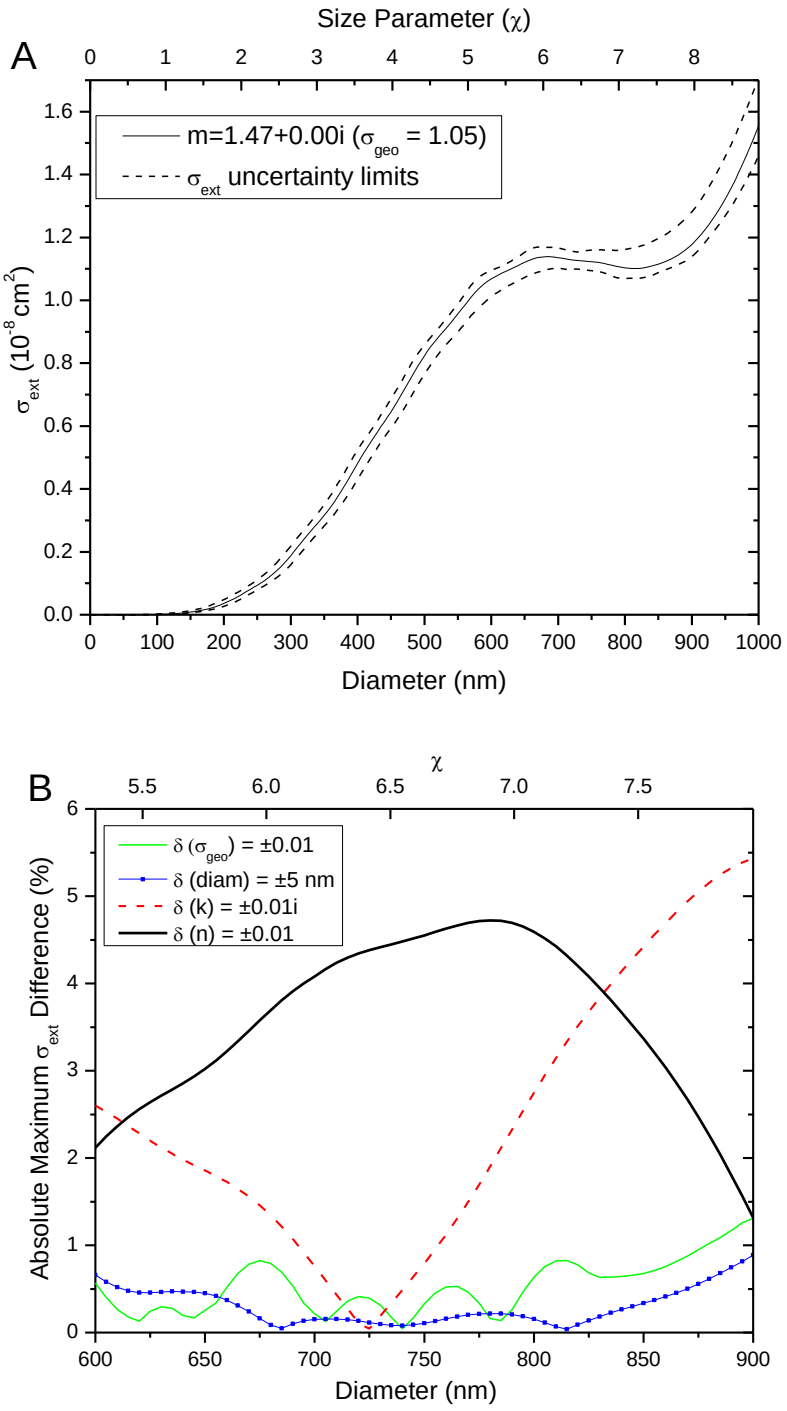

Figure 2.2. Effect of uncertainties in σ_{geo}, diameter, k, and n on extinction cross section. (A) Extinction cross section (σ_{ext}) as a function of size parameter (χ) and particle diameter given 355 nm light. The solid line represents a base case where n=1.47, k=0.00i, σ_{geo}=1.05. The dashed lines are the limits for all possible σ_{ext} values given the uncertainties of n±0.01, k±0.01, σ_{geo} ±0.01, and particle diameter ±5 nm. (B) The absolute maximum percent difference in σ_{ext} as each variable is independently adjusted from the base case to the uncertainty limit. This reveals the relative sensitivity to each variable for 600 to 900 nm particles.

Aerosol extinction is customarily displayed as a function of the size parameter, χ, which is a dimensionless ratio of particle circumference to illumination wavelength ($\chi = \pi d/\lambda$). Therefore, the corresponding modal particle diameter is shown along the lower abscissa for 355 nm light. With uncertainties in n, k, and σ_{geo} taken as ±0.01 and uncertainty in the peak diameter as ±5 nm, the range of extinction values deviate from the base curve by 5 – 10% (dashed region). Figure 2.2B reveals that the size-dependent σ_{ext} measurement will be more sensitive to the assumed uncertainties in n and k than in the size distribution and peak diameter tolerance. Selecting a particle size that corresponds to a higher variance in σ_{ext} values will result in greater sensitivity. For example, k values from 0.00i to 0.01i will differ in σ_{ext} by 0.04% ($5x10^{-12}$ cm^2) for 725 nm particles but 5.43% ($6x10^{-10}$ cm^2) for 900 nm particles. In this example, a useful extinction measurement of 725 nm particles would require a sensitivity two orders of magnitude greater than that of 900 nm particles to give similar information about the value of k. Conversely, improved precision of n and k in a calibration substance will allow for detection of noticeable differences in the particle distribution and peak diameter.

In the given example, n and k are responsible for the overall uncertainty in a measured extinction; however the impact of the particle distribution should not be overlooked in all cases. If the complex refractive index could be precisely known, one might suppose that a more monodisperse particle source would improve extinction sensitivity as the σ_{ext} curve begins to show more oscillating “ripple effects”.

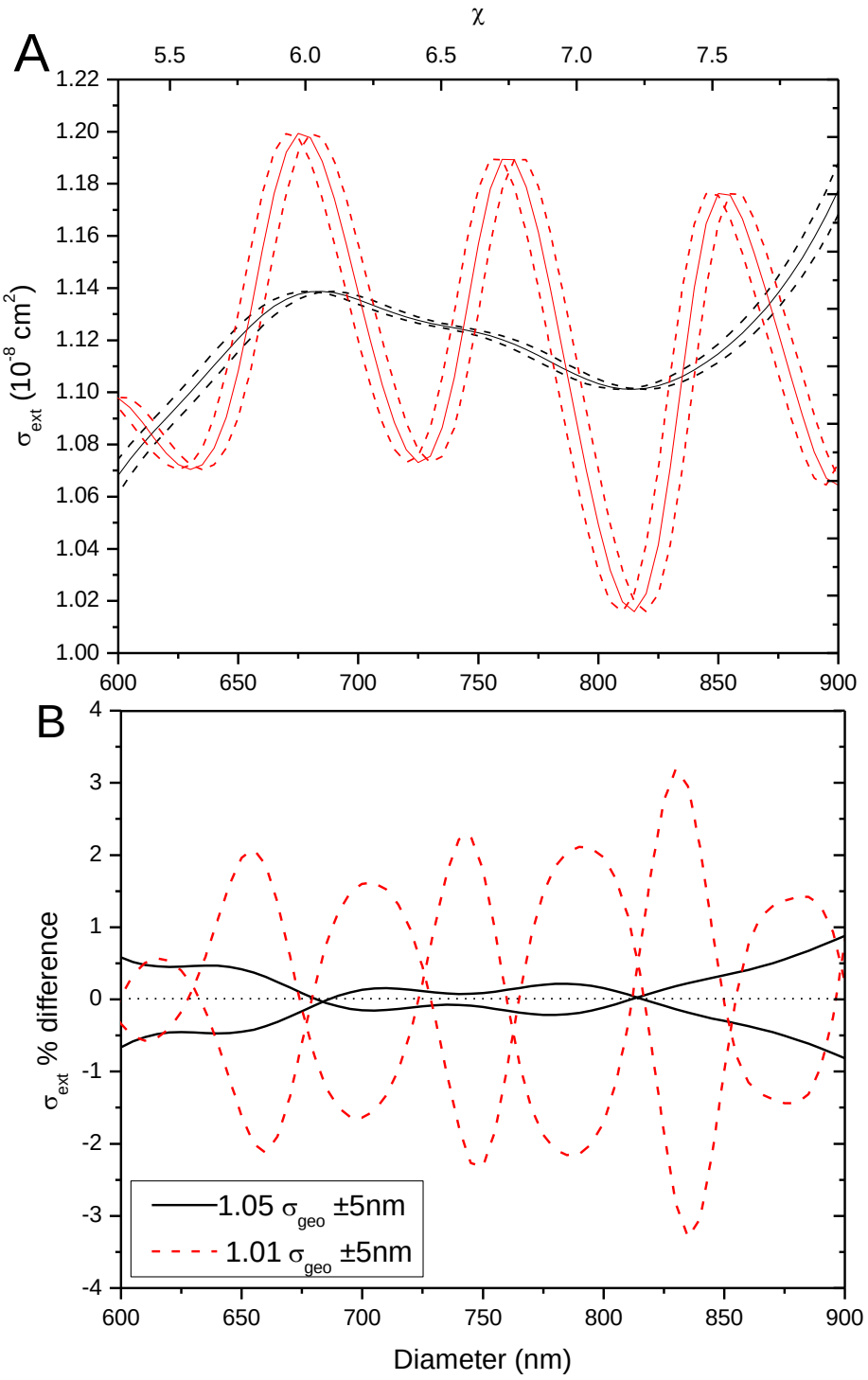

Figure 2.3. Effect of σ_{geo} and size tolerance. (A) Extinction curves are shown for m = 1.47 + 0.00i with σ_{geo} = 1.05 (black curves) and σ_{geo} = 1.01 (red curves). The dashed lines represent a positive and negative shift in diameter (Δ_{diam}) of 5 nm. (B) The percent difference in σ_{ext} for ±5 nm size shifts. The broader distribution reduces the effect of a mean diameter uncertainty.

Unfortunately a narrower size distribution becomes limited by the uncertainty in the peak particle size whereas a broader distribution will provide a smoothing effect and reduce errors associated with tolerances on the peak diameter. For the example shown in Figure 2.3B, narrowing the geometric standard deviation from 1.05 to 1.01 with mean diameter tolerances of ±5 nm will increase σ_{ext} uncertainty from <1% to 2-3%. These kinds of narrow size distributions are not merely theoretical comparisons. Often aqueous suspensions of polystyrene latex (PSL) microspheres are used to validate an A-CRDS system because PSLs have certified tolerances by direct comparison to National Institute of Standards and Technology Standard Reference Materials[105-107]. This monodisperse distribution of aerosolized PSLs is attractive as it is normally narrower than the ideal output of the DMA. The standard deviations of PSL diameter and size tolerances are typically 1% of the mean diameter for submicron particles because of transmission electron microscope measurement error and variability of the standard[108, 109]. Also note that the multi-valued nature of the extinction curve, the unique PSL size distribution for each batch, and the requirement to use a separate PSL solution for each size-dependent σ_{geo} measurement adds complexity in employing such materials for A-CRDS calibration techniques.

An ideal calibration substance would be spherical and have a precisely known complex refractive index, size distribution, and mean diameter. Squalane, or spinacane, ($C_{30}H_{62}$) has been used as a calibration substance in various applications for its physical properties[110]. This branched, saturated hydrocarbon is a liquid paraffin at room temperature and can be nebulized because of its relatively low viscosity. It has no electric dipole moment and is safely used as a cosmetic additive. In conjunction with a DMA under acceptable flow rates, any number of mean particle diameters can be selected to target more sensitive regions of the extinction curve. The aerosol size distribution is controlled by adjusting the flow of dry nitrogen through the nebulizer

and in the dilution region to create sufficient concentrations of nanometer sized particles without the influence of potential multiply-charged particles. Because squalane is not volatile (vapor pressure of $1.5x10^{-9}$ mmHg at STP) and is hygroscopic and inert, the refractive index of the particles is consistent with bulk measurements. The measured refractive index at 355 nm used in the A-CRD experiments throughout this study is based on the bulk Snell's Law Cell and ellipsometry measurements made here.

2.3.B. Simultaneous fitting of three calibration parameters. The A-CRDS system was calibrated daily using squalane particles to account for systematic errors in the measurement of σ_{ext} by introducing three adjustable parameters: C_f, Δ_{diam}, and σ_{geo}. C_f adjusts all measurements in the σ_{ext} domain, Δ_{diam} adjusts the selected particle peak diameter, and σ_{geo} is the log normal geometric size distribution of the Mie predicted extinction curve. Thus a χ^2 fitting evaluation will occur at each combination of the three calibration terms within a user-defined range. The results of the retrieved best fit values for the three parameters is displayed in Table 2.2 for each squalane trial spanning the course of several months. Smaller χ_o^2 values indicate a better overall fit for a given number of measured points.

Table 2.2. Compilation of squalane A-CRDS trials with retrieved best fit parameters. 95% confidence ranges for the three calibration parameters are shown in parentheses. N_s is the number of different particle size measurements.

Trial	Date	C_f	Δ_{diam} (nm)	σ_{geo}	χ_o^2	N_s
1	17NOV	0.952 (0.949-0.954)	18 (14-21)	1.045 (1.039-1.054)	10.22	7
7	2DEC	0.860 (0.857-0.862)	30 (22-34)	1.049 (1.041-1.060)	13.64	10
10	8DEC	0.933 (0.931-0.935)	20 (18-22)	1.037 (1.035-1.040)	10.34	10
13	22DEC	1.005 (1.001-1.008)	22 (15-27)	1.041 (1.037-1.046)	1.16	6
21	2FEB	0.984 (0.983-0.988)	15 (13-18)	1.040 (1.037-1.043)	14.11	10

Calibration factor, C_f. The most significant improvement in the retrieval of an accurate refractive index occurs with the introduction the calibration parameter, C_f. This term is a linear scalar of the experimentally determined extinction cross section and could be a result of systematic errors in α_{ext} or particle concentration. The value of the best fit C_f ranged from 0.860 to 1.005 with day-to-day variations of 1 to 10%. As depicted in Figure 2.4, all σ_{ext} measurements for a given trial appear to deviate linearly from the calculated Mie extinction curve, but the variation among trials is as much as 10%. C_f will not account for size-dependent errors as all σ_{ext} measurements in a trial are scaled with the same term. Possible sources of this systematic error are over or under-counting (counting inefficiency) of the CPC, uncertainty in the measurement of R_L, particle losses inside and after the CRD cell, and flow effects that lead to inhomogeneity of the aerosol sample. It will be shown that this parameter is sufficient to account for the majority of daily changes in the system.

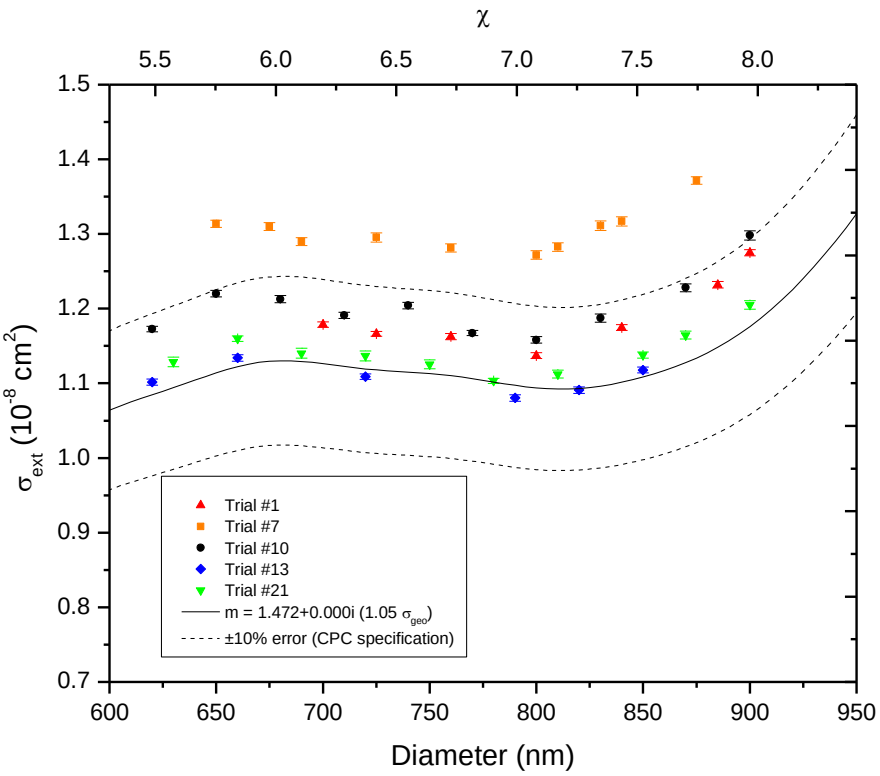

Figure 2.4. Day-to-day fluctuations of five squalane trials. The measurements shown were taken over the course of several months. The solid line is the theoretical curve for the measured refractive index of squalane (m=1.472+0.000i and 1.05 σ_{geo}). The dashed lines represent the ±10% uncertainty in σ_{ext} corresponding to the manufacturer's stated uncertainty of particle counting by the CPC.

Though it is not the purpose of this paper to attribute all possible errors, several sources are considered here. First, the error in the measurement of the effective pathlength of the aerosol in the CRD cell and understanding the flow of particles through the cavity are not trivial. Fluid dynamic simulations model the flow regimes but, to our knowledge, experimentally characterizing the aerosol in the entire beam volume has not been reported in A-CRDS. It is worth noting that the particles are assumed to be statistically homogenous and have an equal probability of occupying any point within the laser beam volume. This assumption inherently cannot be achieved as the aerosol must flow radially into and out of the beam, and even in laminar conditions, the uncertainty leads to errors in the calculated R_L. This effect would not

occur with an infinitely narrow beam; however, the limiting assumption is that the aerosol flow is consistent for the duration of each measurement. Attenuation (i.e. extinction) of light from spatially correlated particles will be underestimated as the particles no longer obey Poisson statistics[111, 112]. Concentration and effective pathlength fluctuations will require longer sampling times to achieve effective random character. This required meticulous procedure and waiting approximately ten minutes between measurements for all the flows to reach equilibrium. The overall flowrate was determined by the fixed intake of the CPC, so daily fluctuations in R_L would be anticipated from errors in the selected 1.5 SLPM flow. Trial 22 and 23 also show the influence of different mixing and dilution setups on the magnitude of C_f.

Table 2.3. Squalane A-CRDS trials with same-day comparisons of different DMAs, flow conditions, and CPCs. The 95% confidence range in each term is shown in parentheses.

Trial	Date	C_f	Δ_{diam} (nm)	σ_{geo}	χ_o^2	N_s	Comments
13	22DEC	0.996 (0.993-0.999)	32 (26-37)	1.055 (1.048-1.061)	4.55	6	DMA#2
14	22DEC	1.005 (1.001-1.008)	22 (15-27)	1.041 (1.037-1.046)	1.16	6	DMA#1
15	23DEC	0.975 (0.971-0.978)	17 (10-22)	1.041 (1.037-1.047)	7.19	6	DMA#1
16	23DEC	0.972 (0.968-0.975)	31 (23-37)	1.056 (1.049-1.064)	4.31	6	DMA#2
17	28DEC	0.988 (0.984-0.991)	32 (25-38)	1.051 (1.044-1.058)	8.45	6	DMA#2
18	28DEC	0.991 (0.988-0.994)	32 (27-37)	1.053 (1.047-1.058)	4.72	6	DMA#2
19	29DEC	0.977 (0.971-0.981)	16 (3-24)	1.040 (1.032-1.046)	7.84	6	DMA#1
20	29DEC	0.984 (0.980-0.988)	22 (14-30)	1.044 (1.038-1.052)	3.07	6	DMA#1
21	2FEB	0.984 (0.983-0.988)	15 (13-18)	1.040 (1.037-1.043)	14.11	10	Fitting only 630-900 nm diameter measurement
22	15FEB	0.941 (0.938-0.944)	32 (24-38)	1.040 (1.036-1.047)	5.52	4	Standard mixing arrangement
23	15FEB	0.982 (0.979-0.985)	32 (22-40)	1.037 (1.032-1.044)	0.06	4	Alternative mixing arrangement
24	7MAR	0.974 (0.970-0.977)	16 (10-22)	1.039 (1.036-1.042)	1.38	6	CPC#1
25	7MAR	1.060 (1.056-1.065)	23 (17-29)	1.039 (1.035-1.044)	3.40	6	CPC#2

Different mixing regimes were ensured by switching the inlet (A) and outlet port (B) of the flask (Figure 2.1). Though only anecdotal evidence, the best fit C_f for the trials varied by 4%, and this difference is the largest recorded *same-day* variation observed for an identical CPC. Note that only C_f, and not Δd or σ_{geo}, was influenced by changing the particle mixing regime. It is recommended that dilution and mixing conditions are thoroughly considered because longer residence times might reduce concentration variability but will increase the likelihood of agglomeration and particle loss.

The largest contribution of uncertainty in these A-CRDS measurements results from assuming that the CPC measures particle concentration with perfect accuracy. Despite the counting differences in calibrated commercial CPC's and daily changes in flow conditions, the counting efficiency remained stable throughout daily operation[113]. A simple test of the CPC counting efficiency was conducted by direct comparison with another identical model CPC (temporarily provided by the manufacturer).

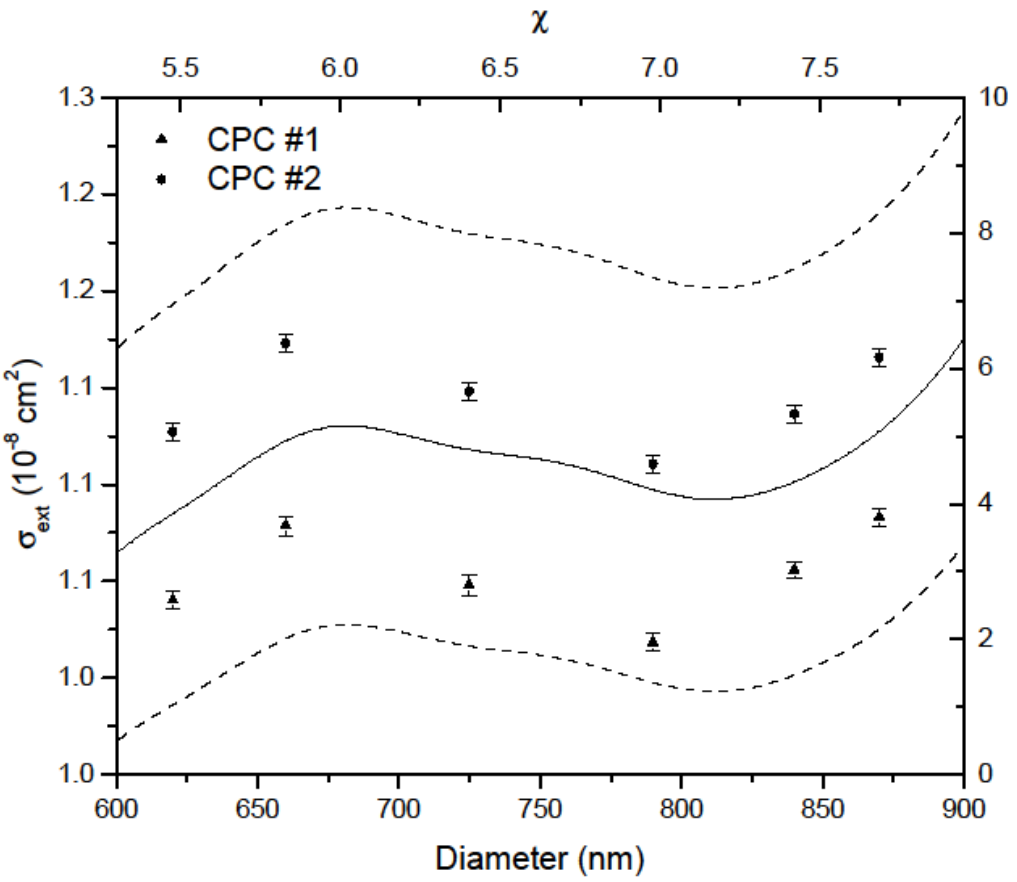

Figure 2.5. Same-day experimental data for two CPCs. The dashed lines represent a ±10% error in the measured σ_{ext}. The best fit C_f is 0.974 for CPC#1 (▲) and 1.060 for CPC#2 (●).

As shown in Figure 2.5, the ±10% accuracy limit of the CPC encompasses all measurements, but there is a clear distinction between the two CPCs' counting efficiency. Despite the significant difference in C_f for the two CPC's (Trial 24 and 25), Δ_{diam} and σ_{geo} are nearly identical and fall well within the typical range of values for this experiment.

DMA peak diameter correction, Δ_{diam}. The recorded particle diameter (or size parameter) for a σ_{ext} measurement is based on the assumed mean diameter of particles output in a narrow distribution from the DMA. The fitting parameter, Δ_{diam}, shifts the predicted mean diameter (in nm) of all measurements in the size domain. The term "size" is used to refer to the geometric

mean diameter of the peak particle output of the DMA. The simultaneous fitting algorithm consistently converged on a best fit value for Δ_{diam} of +15 to +25 nm and was not correlated to the magnitude of C_f. A shift of 20 nm in the assumed peak particle size will result in as much as 5% error in squalane's σ_{ext} measurements, so systematic errors exist in the selected particle size. The mobility equivalent particle diameter, d_m, is determined by the DMA software with

$$d_m = \frac{2neVLC}{3\mu q_{sh} \ln\frac{r_2}{r_1}} \tag{2.7}$$

where n is the number of elementary charges, e is electronic charge, V = the average rod voltage, C is the Cunningham slip correction, μ is gas viscosity, q_{sh} is the sheath flow and r_2, r_1, and L are physical dimensions of the DMA. The mobility diameter of a charged particle will necessarily equal the volume equivalent diameter (d_{ve}) for a spherical particle, though d_m for non-spherical morphologies will necessarily be larger than d_{ve}[114]. Plausible sources of the observed size offset include calibration errors in the DMA sheath flow and an inappropriate Cunningham Slip Correction Factor. Other conditions within the DMA must be responsible for the positive Δ_{diam} as the liquid particles are presumed to be spherical. The DMA software computes the required rod voltage based on the user-selected d_m and sheath flow rate. The applied voltage assumes a particle with one elementary charge and accounts for the ambient temperature, pressure, and the physical dimensions of the DMA. A previous study has measured a 1.9% difference in the DMA's selected d_m and 100 nm Standard Reference Materials[115]. This systematic error was attributed to the shorter "effective" aerosol pathlength, and this is reasonable as the particles will encounter non-uniform field lines at the entrance and exit. Also, the flow regime of gas around the particle depends on the particle diameter, type of carrier gas, and temperature and pressure[91].

The Cunningham Slip Correction Factor is introduced to account for the reduction in drag forces on the particle as the relative gas velocity increases in the transition and molecular regime[116] where

$$C = 1 + Kn\left[\alpha + \beta \exp\left(\frac{-\gamma}{Kn}\right)\right] \tag{2.8}$$

The constants α, β, and γ are empirical constants that are determined from the particles and flow system studied. The Knudsen number (Kn) is the dimensionless ratio of the mean free path to the particle radius ($Kn = \lambda/r = 2\lambda/d$) and quantifies the flow regime[97]. For $Kn \gg 1$, the free molecular regime describes a particle moving with discrete collisions with gas molecules. For $Kn \ll 1$, the continuum regime describes a particle that is moving through a continuous gas fluid. Normally, the DMA is operated in the variable transition regime ($0.1<Kn<1$) where errors in the presumed particle diameter will influence the calculated drag force. Also pressure and temperature inaccuracies of the DMA will propagate into errors in Kn. The DMA software uses values for α, β, and γ that were experimentally determined from PSL measurements[117]. Using values for α, β, and γ from measurements of oil droplets[118], the selected mobility diameter(i.e. applied voltage) will transmit a mean diameter ~8 nm larger than calculated by the DMA for particle sizes between 600 and 900 nm. This implies that the drag force experienced by the oil particles is less than that of solid particles given similar flow regime conditions.

DMA size distribution, σ_{geo}. The final calibration parameter, σ_{geo}, accounts for uncertainty in the DMA's output size distribution. Each experimental measurement is compared to the theoretical size equivalent for a particular distribution such that the resolution of the DMA is assumed to have no size dependence over the particle sizes selected. As the size distribution widens the theoretical extinction curve will begin to smooth, and conversely a narrower distribution will result in more pronounced oscillatory behavior. As demonstrated in Figure

2.3A, the ripple structure of an incorrectly assumed size distribution will result in measurable positive and negative differences in σ_{ext}. Retrieved best fit σ_{geo} values ranged from 1.034 to 1.059 which is similar to reported values for this type of DMA[60, 119-122]. In this regard, this procedure independently characterizes a single DMA through A-CRDS measurements.

The DMA resolution, or "transfer function" as derived by Knutson and Whitby[96], is defined as the probability that a charged particle of a given mobility will traverse a given electric field and exit the DMA. Resolution is primarily degraded from diffusional broadening and instrument imperfections such as flow turbulence, variability of the electric field at the aerosol inlet/exit, and misalignment of the high voltage rod[123-126]. With a sheath to sample flow ratio of 10:1 and the particle diameter range selected, the effects of diffusional broadening are negligible for d_m>100 nm[127]. Unfortunately, two "identical" commercial DMAs do not exhibit identical transfer functions, so attempts to characterize a DMA typically involve comparison with a similar DMA in a tandem configuration (TDMA) with a CPC. The first DMA is used as a monodisperse particle generator, while the second DMA and CPC measure the output particle concentrations over a size range. However, this approach inherently assumes that both DMAs have identical transfer functions and deconvolution requires computational approximations[128] or a third DMA[113]. A single DMA's transfer function could potentially be characterized by measuring the σ_{geo} for a series of A-CRDS measurements if sensitivity was sufficient.

To test the ability to differentiate two transfer functions, eight trials were conducted with two DMAs using identical flow conditions (Trial#'s 13-20). The resultant best fit parameters show that C_f changes by < 1% when the two DMAs are exchanged in the same day indicating that C_f is independent of the DMA. The statistically significant difference of the σ_{geo} and Δ_{diam} is confirmed with 99% confidence by comparing the best fit values for the eight alternating DMA

trials. We assumed the true DMA transfer function is constant day-to-day and the best fit parameters are normally distributed about a mean. Of the eight comparison trials, DMA#1 had a best fit range for σ_{geo} and Δ_{diam} of 1.040 – 1.044 and 16 – 22 nm, respectively, whereas the same best fit parameters for DMA#2 ranged from 1.051 – 1.056 and 31 – 32 nm. The day-to-day consistency in the σ_{geo} and Δ_{diam} parameters indicate that a single calibration measurement could characterize the DMAs actual peak diameter output and size distribution.

2.3.C. Influence of multiply-charged particles. The Mie curve is a function of the size parameter (χ) and not geometric diameter, so wavelengths other than 355 nm will have different equivalent sizes to obtain similar sensitivities. Regardless, the extinction values along the Mie curve with the lowest gradient in σ_{ext} will be most sensitive to C_f while the values with the steepest gradient will be most sensitive to changes in Δ_{diam}. In general, sensitivity to variation in n and k is better at higher size parameters (i.e. larger particles) where there are larger differences in σ_{ext} for all three parameters. One of the most significant advantages of nebulizing the pure squalane is that measureable concentrations of particles larger than 500 nm are possible. This is not always the case with atomization of a solution, a common technique for generating aerosols, that results in smaller particles.

Selecting larger particles with the DMA reduces the influence of multiply-charged particles with equivalent electrical mobility and disproportionate extinction cross section. For a selected voltage and sheath flow, larger particles with multiple charges (and equivalent electrical mobility to that of the singly-charged particle) would be permitted to pass the DMA and lead to positive errors in the measured σ_{ext}. The contribution of multiply-charged particles will depend primarily on the relative concentrations of larger particles being generated in the aerosol source. The polydisperse output of the nebulizer peaks at 300-400 nm with concentrations diminishing

precipitously for diameters greater than 800 nm. Considering the nebulizer output, the impactor cut point (d_{50} = 995 nm), and the relative probability of a larger particle carrying multiple charges through the bipolar charger[94, 95], it is estimated that the concentration of multiply-charged particles will be less than 0.2% of the singly-charged particle concentrations for selected particles diameters > 600nm. Predicted error in the measured σ_{ext} was experimentally confirmed by collecting σ_{ext} measurements for squalane at smaller sizes.

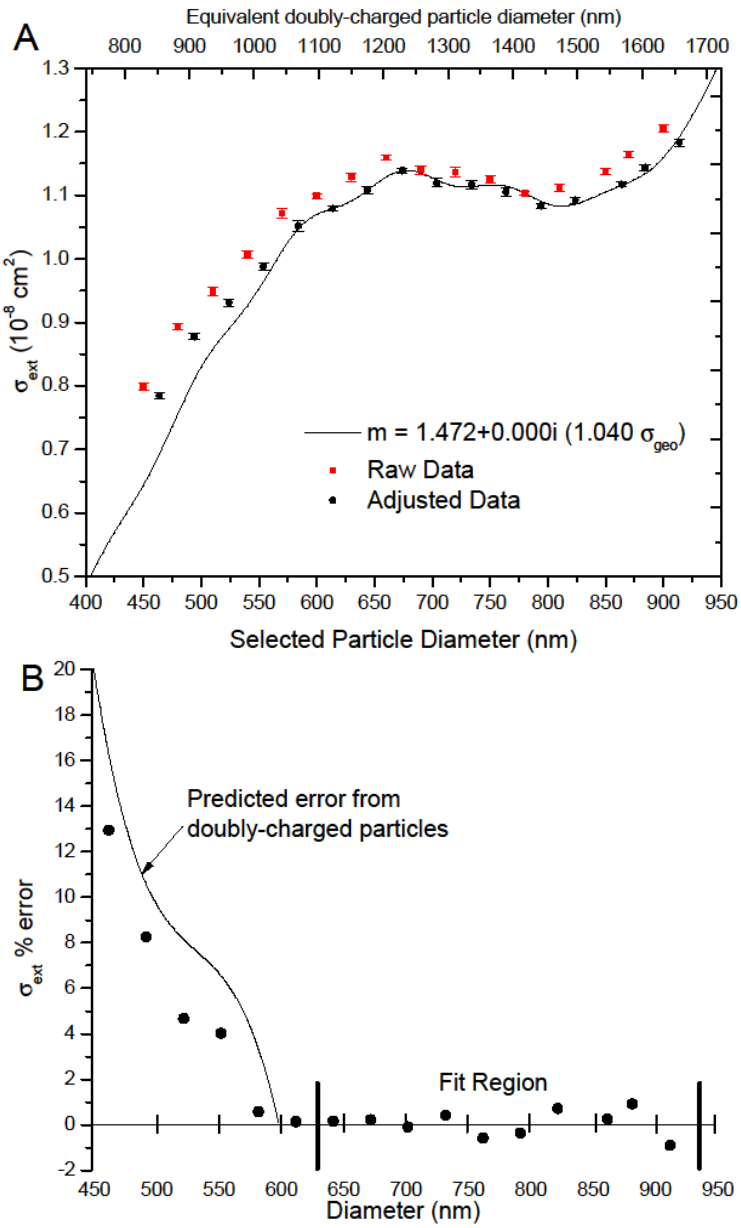

Figure 2.6. Selecting a fit region that avoids multiply-charged particles. (A) Collected data (red squares) and adjusted data (black circles) for Trial #21. The fit parameters were retrieved for 630 – 900 nm diameter measurements. (B) The residual for the fit experimental data depicts the influence of multiply-charged particles at smaller particle diameters.

The calibrated results and σ_{ext} errors are shown in Figure 2.6 by fitting the 630 – 900 nm diameter measurements. The equivalent doubly-charge particle diameter is less than $2d_p$ because the Cunningham slip correction is size dependent. The simultaneous fit χ_o^2 for the largest ten

sizes is 14.11, and the χ_o^2 by fitting the smallest ten sizes (presumably with larger multiply-charged particle influence) is 79.69. The multiply-charged particle influence is clearly avoided by direct nebulization and selecting particle sizes in the tail of the distribution.

2.3.D. Independent Fitting of Calibration Parameters. Normally, the values for each of the three parameters are simultaneously retrieved with the χ^2 minimization algorithm described above; however, each parameter could be introduced in a step-wise fashion to analyze their relative importance in improving the overall fit. A step-wise fitting procedure will improperly weight the first parameter at the expense of the other two. Assuming the parameters are independent, a better overall fit will be reached with a simultaneous fit because initial parameter fitting will not dominate the result. However, if the DMA is well characterized, then only an individual fitting step will be necessary to retrieve a best fit C_f value.

The magnitude of the best fit C_f is determined by retrieving χ_o^2 as the ensemble of points are incrementally scaled and compared to respective Mie solutions. Taking Trial 10 as an example for this single parameter calibration procedure, the residual of each point is noticeably smaller after each σ_{ext} measurement is reduced with a C_f of scalar of 0.930, and χ_o^2 is improved from 3783 to 149.0 (Figure 2.7A). A single variable χ^2 minimization calculation only requires theoretical extinction values for each measurement and can be performed on a simple spreadsheet immediately as data is collected. The fit is further improved by incrementally shifting the DMA-selected mean diameter with a Δ_{diam} parameter. The best fit for this parameter is retrieved by finding a new χ_o^2 as the data is shifted along the particle diameter axis after the C_f scalar is applied.

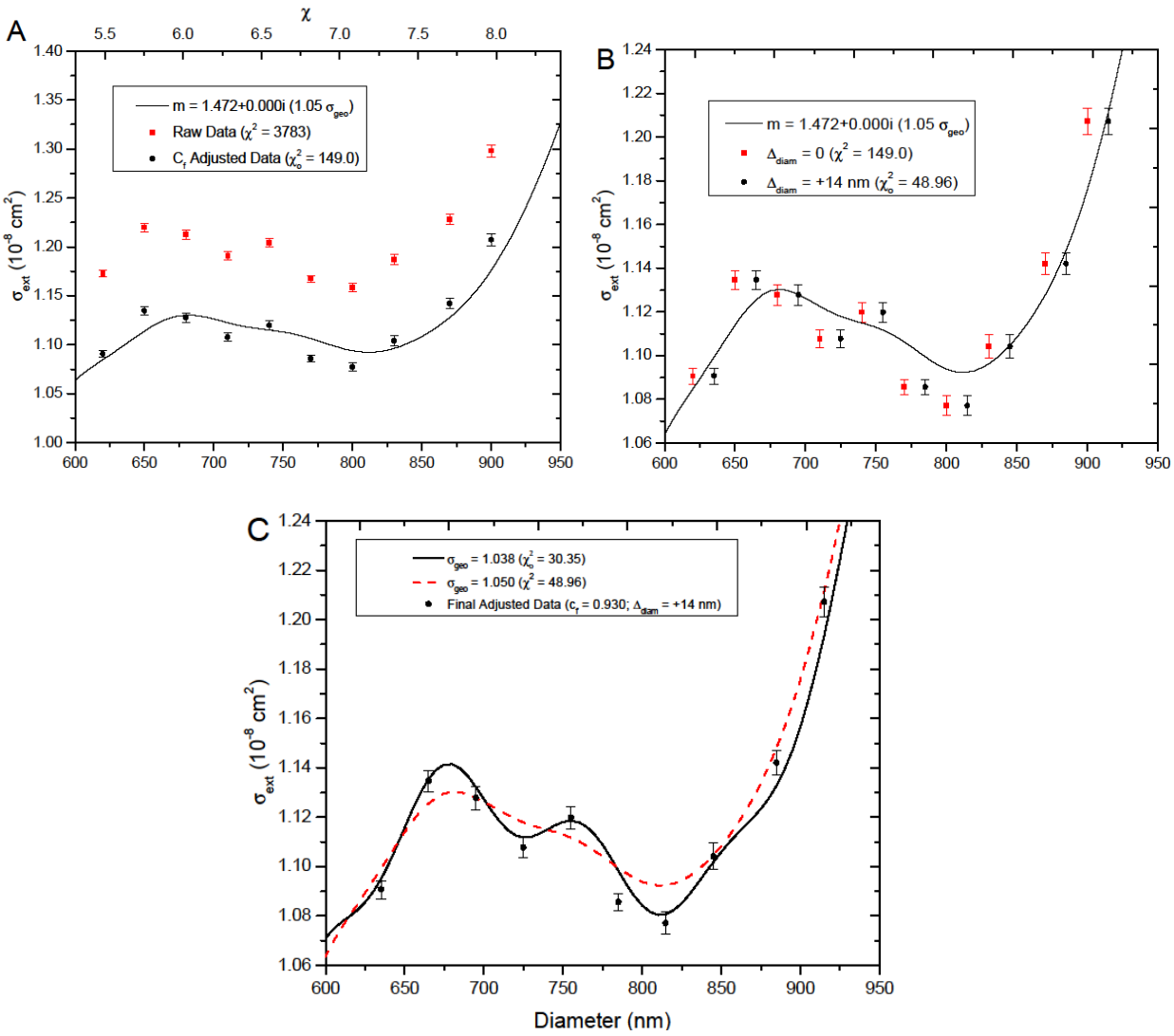

Figure 2.7. Step-wise calibration. Each parameter is shown with raw data (red circles) and the fit data (black circles) for each subsequent step. (A) Step 1 – Raw experimental σ_{ext} data for Trial 10 (8DEC) is displayed along with the scaled data with best fit C_f applied. (B) Step 2 – χ_o^2 is further reduced by incrementally shifting the previously scaled data by Δ_{diam} to obtain a new best fit. (C) Step 3 –The shifted data is compared to a range of size distribution curves to reach a best fit parameter for σ_{geo}.

Figure 2.7B shows the best fit adjustment (Δ_{diam} = +14 nm) as χ_o^2 is now reduced from 149.0 to 48.96. Finally, a new χ_o^2 is obtained with the previously shifted data by incrementally adjusting the geometric standard deviation from 1.020 to 1.090 with a 0.001 step size. Figure 2.7C shows the original theoretical extinction curve (σ_{geo} = 1.05) and a curve corresponding to the best fit

size distribution (σ_{geo} = 1.038). With the addition of the third parameter, χ_o^2 was further reduced from 49.0 to 30.4 corroborating the visual appearance of the improved fit. Despite the improvement after each step, the simultaneous fit for the same data will yield a better fit (χ^2 = 10.34). However, the similarities in the results for the step-wise procedure and a simultaneous fit indicate that C_f is appropriately the most significant calibration factor for extinction cross sections. For the example in Figure 2.7A, the χ_o^2 is reduced from 3783 to 149.0 when the C_f scalar is solely fit to the example raw data. If Δ_{diam} or σ_{geo} parameters are exclusively introduced to achieve a best fit, the χ_o^2 is only reduced to 2691 and 3358, respectively. The Δ_{diam} parameter contributes more than the σ_{geo} to the reduction of χ_o^2 for the given example though the improvement is not substantial in this case. The importance of each parameter will depend on the complex refractive index and the size region where measurements are taken on the extinction curve.

By using different CPCs and DMAs it has been shown that the CPC primarily influences C_f (Trials 24 and 25) while the DMA is responsible for differences in σ_{geo} and Δ_{diam} (Trials 13 – 20). Of course, adding fitting terms to any data will improve the fit, but the important question is whether this approach is valid in attributing systematic errors that can be verified experimentally and are acceptable given stable conditions. If the raw data from Trial 10 is used to retrieve a complex refractive index of squalane without any calibration the best fit result is 1.454+0.001i. The retrieval of squalane's refractive index will undoubtedly be improved if the simultaneous fit parameters adjust the measured σ_{ext} to the theoretical extinction values, so the meaningfulness of this technique must be confirmed by how well it converges on n and k for different substances.

2.4. Conclusions

A novel A-CRDS technique has been developed to retrieve calibration parameters and reduce the systematic errors in extinction measurements. Squalane was selected as an ideal calibration liquid for this application, and its refractive index was precisely measured with a Snell's Law cell and spectroscopic ellipsometry to enhance its use as a standard. The possibility of using another liquid as a calibration substance is only limited by the ability to make a consistent aerosol source and the uncertainty in its refractive index. Collecting extinction measurements of the calibration substance will permit the simultaneous retrieval of all three calibration terms; however, single variable fitting can vastly improve σ_{ext} accuracy with minimal computational requirements. Only σ_{ext} measurements at four different diameters are usually required to converge on an accurate 3-term fit, so this technique can achieve improved results with as little as one hour for calibration. The calibration terms, C_f, Δ_{diam}, and σ_{geo}, primarily depend on daily aerosol flow changes and commercial instrument calibration errors. The C_f parameter scales the raw σ_{ext} data and can be attributed to the CPC counting efficiency error and uncertainty in the aerosol flow. The other two parameters, Δ_{diam} and σ_{geo}, are primarily influenced by the DMA. Therefore, this is a potential independent calibration technique for a CPC or DMA. This method is also the first known attempt to accurately characterize a DMA's transfer function from a spectroscopic technique.

In further studies it will be necessary to consider the uncertainties in the bulk refractive index of the calibration standard so that uncertainties may be propagated to the final retrieved complex refractive index of another sample. The improved accuracy of this technique would be particularly beneficial for laboratory A-CRDS studies that investigate properties of minimally absorbing substances, coated particles, or mixed aerosols. For example, this technique will

allow for more accurate retrieval of optical properties of laboratory substances with uncertainty in n and k <0.01.

CHAPTER 3

RETRIEVING PRECISE REFRACTIVE INDICES WITH A CALIBRATED AEROSOL CAVITY RING-DOWN SYSTEM

3.1. Introduction

Aerosols play an important role in the global climate and radiative balance by absorbing and scattering light and influencing cloud formation. The optical properties of particles suspended in the atmosphere depend on their morphology, size (relative to the wavelength of light), and complex refractive index. The real and imaginary components of the complex refractive index are determined by the scattering and absorption, respectively. Extinction, the combined scattering and absorption of light, , is particularly important for particles. In the atmosphere, the net effect of aerosols predominately reduces total radiative forcing as expected from the scattering (particularly "back-scattering") of solar radiation[2, 3]. However, the net warming or cooling effect on the atmosphere will depend on the ratio of absorption and scattering[1]. In order to address the uncertainties in this direct aerosol effect, cavity ring-down spectroscopy (CRDS) techniques have been used to measure total aerosol extinction.

The potential to apply CRDS to the study of aerosols and particulate matter has long since been proven in laboratory[40, 49, 50, 53, 54, 58, 60-62, 74, 75, 85, 129] and field[42, 57, 63, 64, 67] studies. The Aerosol-CRDS technique has moved well beyond the proof-of-concept and validation stage, and studies have proven the viability of separating the scattering and absorbing components of extinction by fitting the data and retrieving a complex refractive index. Mie theory is invoked to compare measurements to theoretical values for different combinations of

real and imaginary components. Each complex refractive index has a unique extinction curve, and a best fit can be retrieved by minimizing the errors with a chi-square minimization algorithm.

Precise experimental measurements require a stable system and a homogenous aerosol from which extinction is measured for varying particle sizes or illumination wavelength. The ratio of particle circumference (πd) to wavelength is conventionally used to define the size parameter, χ. The sensitivity of A-CRDS to the real and imaginary components of the complex refractive index is not uniform for all particle sizes, and the total uncertainty for a given size parameter has several sources such as the tolerance in particle diameter, size distribution, measured particle concentration and effective pathlength of the particle flow. As discussed thoroughly in Chapter 2, the commercial instruments used for A-CRDS may require calibration, and failing to account for systematic errors can increase uncertainty in extinction measurements by 10% or more. Higher levels of precision in extinction measurements are required to reduce uncertainties in the retrieved complex refractive indices. A first step in this regard will be to calibrate the entire system so that systematic errors do not lead to inaccurately retrieved scattering and absorption values. Three instrument calibration parameters, C_f, Δ_{diam}, and σ_{geo}, were previously shown to improve the refractive index fit. It is now worthwhile to consider the ability of this calibration process to improve the refractive index fit for subsequently measured substances. It is important that uncertainty is propagated into the reported complex refractive index for meaningful interpretation, but this is not always done. If reported at all, the uncertainty ranges from 1 to 3% for the real component and a few to over a hundred percent for the imaginary component[40, 65]. Additionally, the highest confidence level reported to date in the retrieved complex refractive index range is 1σ (68%)[61, 74].

The goal here is to develop a valid computational technique that will precisely retrieve a complex refractive index with a confidence level of 95%. The calibration technique described previously will be used with squalane, a purely scattering refractive index reference standard. In this work, the additional uncertainty in the bulk measurement of squalane's refractive index and the uncertainty in the σ_{ext} resulting from the three calibration parameters will be propagated into the retrieved complex refractive index. measurements. It will be shown that the average absolute error in the calibrated measurements of σ_{ext} are reduced from 5 – 10% to less than 1%, and retrieved complex refractive indices are consistently within 0.005 of independent precision reference measurements.

3.2. Materials and methods

3.2.A. Bulk refractive index measurements. Refractive index measurements of squalane (99%, Sigma Aldrich), bis-ethylhexyl sebacate (DOS; 98%, Sigma Aldrich), squalene (98%, Sigma Aldrich), and methanol (99%, Sigma Aldrich) were taken at temperatures 24.0±1.5 C. The complex refractive index of each liquid was determined with spectroscopic ellipsometry at J.A. Woolam laboratories. A commercial ellipsometer (J.A. Wollam Co, M-2000V) was used to analyze each sample with 190 nm to 1700 nm polarized light at 2 nm intervals. For the purely scattering substances, the Cauchy dispersion relation is used to fit the wavelength-dependent refractive index measurements to the empirical equation

$$n_\lambda = A + \frac{B}{\lambda^2} + \frac{C}{\lambda^4} \tag{3.1}$$

where n_λ is the wavelength of light and A, B, and C are constants. Results from these measurements are shown below with comparison literature values for Squalane.

Table 3.1. Fitted constants using the Cauchy dispersion formula.

Substance	A	B (nm^2)	C (nm^4)	n_{355}	Reference
Squalane	1.43694	3677.6378	8.28899×10^7	1.471	This work
	1.44923	-2086.7547	5.85333×10^8	1.470	Painter (1984) †
	1.44034	4325.5006	-4.38217×10^6	1.474	Sorensen (1951‡
Methanol	1.31902	3226.8865	1.95969×10^7	1.346	This work
DOS	1.43733	3383.6460	9.41919×10^7	1.470	This work
Squalene*	1.47742	4609.3723	2.53278×10^8	1.530	This work
IL 1160	1.4663765	4997.30	1.487527×10^8	1.515	Cargille Laboratories

†: UV reflectance and transmission measurements with Kramers-Kronig anlysis
‡: Extrapolated fit from precise refractometer measurements at visible wavelengths
*: Constants were fitted at wavelengths where it did not measurably absorb (λ>250nm)

The refractive index of each substance was also independently measured using a custom Snell's Law cell discussed in Chapter 2. Briefly, the refraction of light from the sample was directly measured by the divergence of two identical laser beams passing through the sample. Three lasers were used to determine the refractive index at 355 nm (the third harmonic of a Nd:YAG pulsed laser beam (Spectra-Physics Pro250, 10Hz, long pulse)), 532 nm (a 50 mW green diode laser), and 633 nm (a 10 mW helium-neon laser (Hughes 3225H)). The laser beams were carefully aligned by tracing the back-reflections of each incident beam. This procedure ensured that the light entered the cell normal to the front windows and exited at the same point on the rear window. The refractive index for squalane at each of the three wavelengths matched the ellipsometry measurements within ±0.002. Throughout this work squalane's refractive index at 355 nm is reported as 1.472 ±0.002 with no absorption component. The largest difference in the measured refractive index for the two techniques for methanol, DOS, and squalene was 0.001, 0.003, and 0.006, respectively.

3.2.B. Pulsed A-CRDS system. The cavity ring-down spectroscopy system is described in detail in Section 2.2., so only a brief summary will be described here. Nanosecond pulses of 355 nm light are captured in an optical cavity consisting of two highly reflective mirrors (R≈0.9988). The TEM_{00} mode of the cavity is preferentially excited by careful alignment, a spatial filter, and a series of optics at the photomultiplier tube. The detected light intensity decays exponentially in time from losses within the cavity. Ten decay transients are averaged and digitized on an oscilloscope and transferred to a personal computer for fitting. By measuring the decay time of the nitrogen filled cavity, τ_o, and the decay time of the particle laden flow, τ_{samp}, an extinction coefficient is determined by

$$\alpha_{ext} = \frac{R_L}{c}\left(\frac{1}{\tau_{samp}} - \frac{1}{\tau_o}\right) \tag{3.2}$$

where R_L is the ratio of particle and optical pathlengths and c is the speed of light. Particles were consistently generated from pure liquid samples with a concentric nebulizer under dry nitrogen flow. Concentrations were controlled by diluting the aerosol to desired levels with additional dry nitrogen, and a monodisperse distribution of the aerosol is selected with a differential mobility analyzer (DMA). Once the aerosols are size-selected by electrical mobility, they flow at 1.5 SLPM into the CRD cell and attenuate the resonating light through scattering and absorbing processes. A butanol condensation particle counter (CPC) measured the particle concentration exiting the cavity so that the particle extinction cross section is determined by

$$\sigma_{ext} = \frac{\alpha_{ext}}{N} \tag{3.3}$$

where N is the particle number density. A σ_{ext} measurement is determined every second by taking the ratio of the cavity extinction (cm^{-1}) to the measured particle concentration(cm^{-3}), and each reported σ_{ext} is the average of four 120 s measurements. Considerable time is given before and after a measurement to ensure particle equilibrium is reached such that a consistent particle

path through the cavity is maintained. A small dilution purge flow is introduced at the face of each mirror to prevent degradation of reflectivity from particle deposition.

3.2.C. Fitting routine. The retrieval of a complex refractive index is accomplished by first calibrating the A-CRDS system with a substance of known optical properties. Squalane was selected for this role as a refractive index standard because it is liquid, inert, non-volatile, and hygroscopic. This calibration technique was accomplished by introducing three fitting parameters: C_f, Δ_{diam}, and σ_{geo}. C_f is an extinction cross section scalar, Δ_{diam} is a size shift to the selected particle diameter, and σ_{geo} defines the size distribution of the aerosol. It was previously shown that the improvement in the fit was not merely mathematically induced, as each parameter was primarily the result of systematic errors in instrument calibration. That is, the calibration terms account for real errors and are not used as a tool to artificially improve a fit. It was also revealed that day-to-day variations in C_f were on the order of several percent and require a daily calibration step before experimental trials.

The chi-squared (χ^2) minimization fitting method is used to determine best fit parameters for two distinct evaluations. The first evaluation is used to retrieve the three calibration terms, and the second evaluation retrieves a best fit for the complex refractive index (i.e. n and k) for a set of calibrated data. For both procedures, an experimental σ_{ext} value is compared to the predicted Mie value, σ_{Mie}, for a given aerosol's peak diameter and size distribution with

$$\chi^2 = \sum_{i=1}^{N_s} \frac{(\sigma_{exp} - \sigma_{Mie})_i^2}{\varepsilon_i^2} \tag{3.4}$$

where ε_i is the uncertainty in the experimental σ_{ext} for a particular peak particle diameter and N_s is the total number of particle size measurements. The best fit, χ_o^2, corresponds to the set of parameters in which the summed weighted residuals are minimized. It can be seen that χ^2 will scale with N_s, so the magnitude of χ_o^2/N_s will reveal information about the relative goodness of

the best fit regardless of the number of measurements. In both fitting routines, a range for the fitting parameters is selected with a corresponding incremental step size. Therefore, the χ^2 for each evaluation point for a given set of parameters (for example, n = 1.450 and k = 0.002) can be compared to χ_o^2 to create relative confidence limits. In the case of the calibration procedure, the 95% confidence region will be bound in the three-dimensional fitting parameter domain by a single contour. Assuming each parameter is independent, the 95% contour limit is met for all evaluations where $\chi^2 < 3.84 + \chi_o$ for one degree of freedom[102]. Each evaluation within this contour is displayed in Figure 3.1 whereby a global maximum and minimum for each parameter (axis) can be retrieved. This graphical representation is similarly shown for the refractive index retrieval where a two dimensional contour will encompass all combinations of n and k where $\chi^2 < 6.18 + \chi_o$ corresponding to two degrees of freedom.

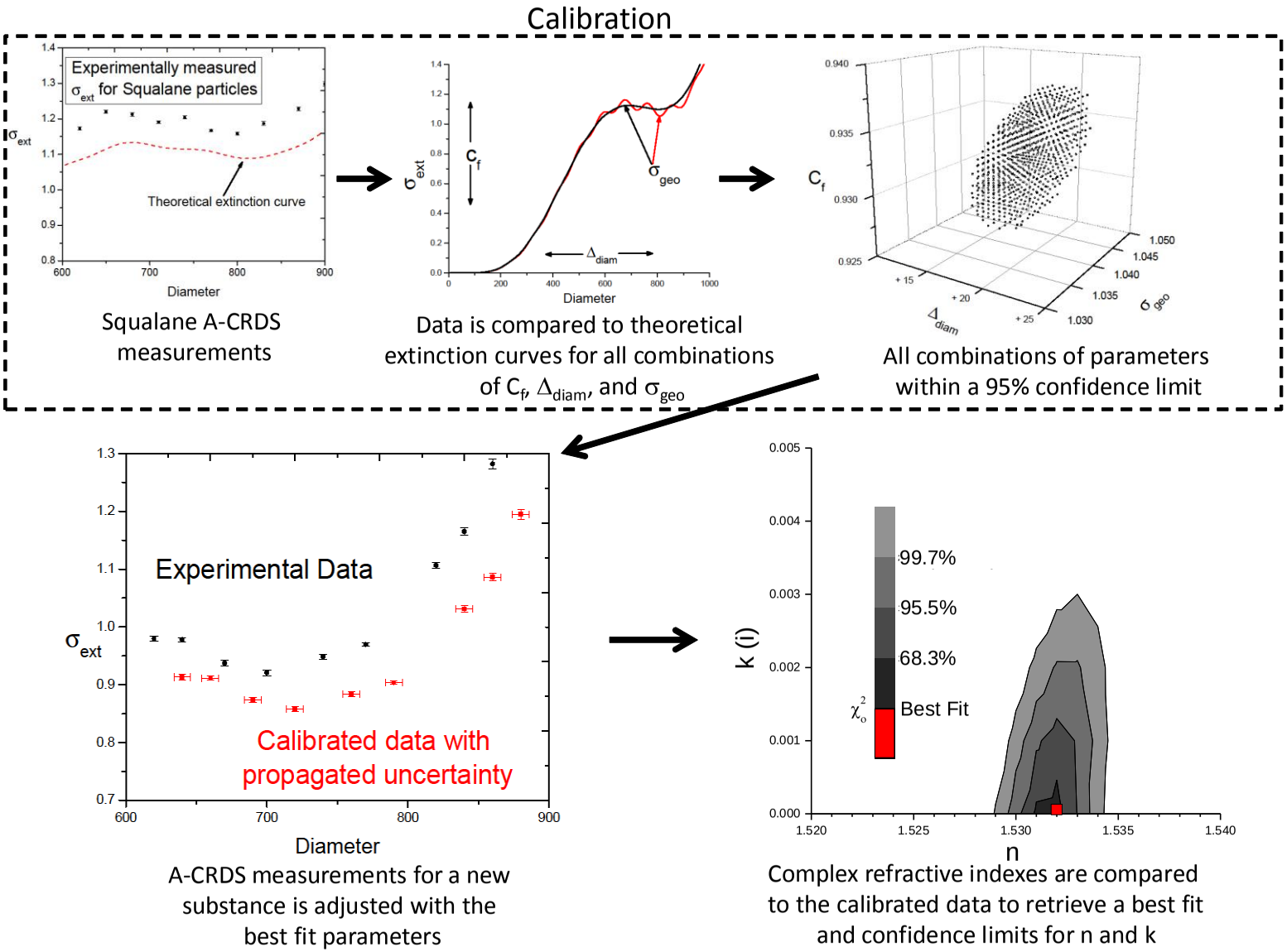

Figure 3.1. Flowchart of calibration and fitting a complex refractive index.

Normally, the total uncertainty was taken as twice the standard deviation of the σ_{ext} measurement for both fitting routines. However when retrieving calibration parameters with squalane, the true 95% confidence region should be expanded to account for the additional uncertainty in the reference refractive index, ε_{sq}, by

$$\chi^2 = \sum_{i=1}^{N_s} \frac{(\sigma_{exp} - \sigma_{Mie})_i^2}{\varepsilon_i^2 + \varepsilon_{sq}^2} \tag{3.5}$$

This additional uncertainty term was evaluated as half the range in extinction cross sections for values of n from 1.470 to 1.474. This term will vary marginally with each selected particle diameter and the size distribution.

The total uncertainty associated with the range of C_f, Δ_{diam}, and σ_{geo} values was further propagated into the final complex refractive index retrieval algorithm. The uncertainty from the range of C_f values could be directly propagated as the calibrated extinction cross section is scaled equally for each measurement

$$\sigma_{cal} = C_f \sigma_{ext} \tag{3.6}$$

The uncertainty from the range in Δ_{diam} and σ_{geo} was calculated as a single term by evaluated the theoretical maximum and minimum σ_{ext} for combinations of the two parameters. The previously determined 95% confidence range for both parameters was subdivided into four evaluation steps so that a total of sixteen total σ_{ext} values were simulated. Uncertainty from the combined terms was taken as half the total range thus giving a final evaluation of

$$\chi^2 = \sum_{i=1}^{N_s} \frac{(\sigma_{cal} - \sigma_{Mie})_i^2}{C_f \varepsilon_i^2 + \varepsilon_{C_f}^2 + \varepsilon_{\Delta_{diam},\sigma_{geo}}^2} \tag{3.7}$$

3.3. Results and discussion

3.3.A. Wavelength and size dependence of the refractive index. The bulk refractive indices of several purely scattering substances were measured at various wavelengths with a Snell's Law cell and ellipsometry. With both techniques the wavelength dependence of the refractive index can be fit to the empirical Cauchy Dispersion equation as long as the substance is purely scattering. Regardless, the real component of the refractive index will increase with decreasing wavelength of interacting light.

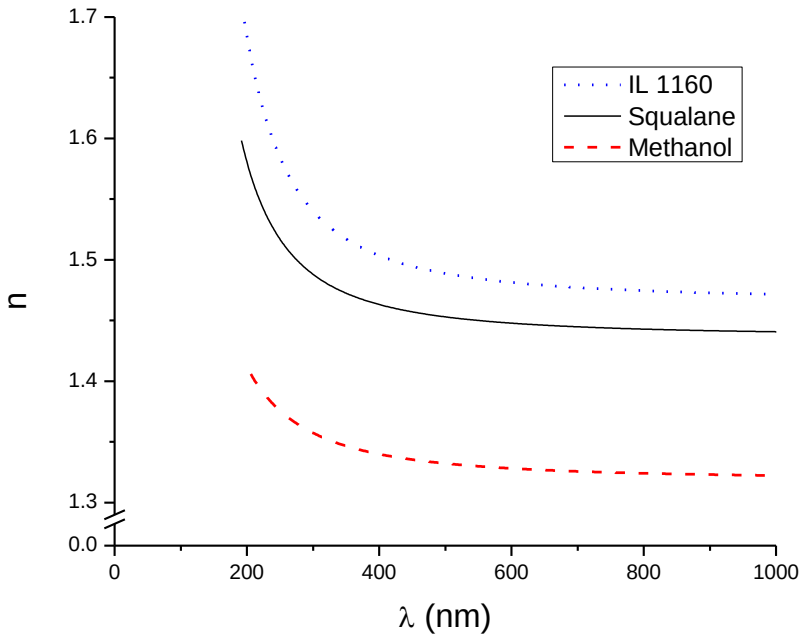

Figure 3.2. Ellipsometry measurements of the refractive index as a function of wavelength.

Two important features observed in Figure 3.2 are the asymptotic behavior at longer wavelengths and the rapid increase at lower wavelengths (<400 nm). This behavior makes extrapolations of refractive index measurements into the UV region problematic. Adding to this concern,

absorption also increases with higher energy light, so the importance of direct measurement cannot be overstated if precise measurements are desired. In this work, squalane is used as a calibration standard as its refractive index is precisely measured for a large range of wavelengths, and the resulting Cauchy dispersion constants allow for its use as an A-CRDS calibration liquid for practically any desired illumination wavelength. For the same reason, practically any liquid could be used in this technique so long as it is homogeneous, stable, and has a low vapor pressure.

It would be short-sighted to presume that the bulk refractive index could be applied to all particles of decreasing size as eventually the substance cannot be physically reduced without affecting its optical properties[56]. In the region well-characterized by Mie theory studied here, the bulk refractive index will indeed reflect the bulk measurements as the particle size is similar to the wavelength. However, the size of the particle will greatly influence the extinction for a fixed wavelength of light. Figure 3.3 demonstrates this size dependence for three liquids studied here at 355 nm light. Despite modest differences in these three substances, the extinction differences are substantial at sizes larger than 600 nm.

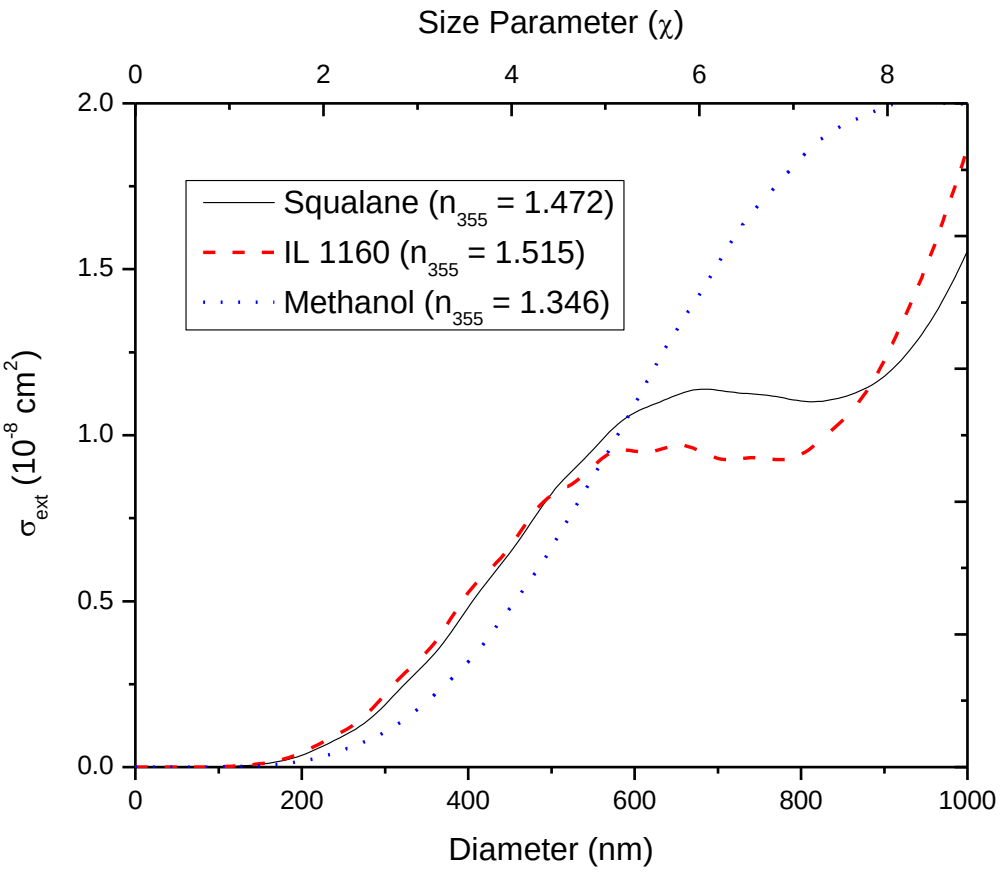

Figure 3.3. Extinction curves for three measured refractive indices at 355 nm. The extinction values are calculated using Mie theory and a standard size distribution (σ_{geo} = 1.05).

If one wanted to differentiate refractive indices from extinction measurements, it is clear that higher sensitivity would be required for smaller particles. These example extinction curves are unique such that precise measurements along the curve will fit a particular refractive index. Though only purely scattering substances are shown here, n and k could be simultaneously retrieved by fitting measurements to a unique extinction curve.

3.3.B. Retrieving precise optical constants. In order to increase precision in the complex refractive index, the A-CRDS system is calibrated with squalane by defining the expected extinction curve and converging on a best fit by stepping through a range of calibration

parameters. Other A-CRDS studies normally validate their system with polystyrene latex spheres (PSLs) and accept errors on the order of a few percent[54, 58, 61, 63, 65, 74, 81], and PSLs have been shown to have a large tolerance in size and a considerable uncertainty in the refractive index[85]. Without calibration, average extinction errors for squalane trials were usually 5 – 8%, but systematic errors as larger than 10% were observed. This is comparable to the error reported in other A-CRDS measurements and was consistent for different wavelengths with CW and pulsed laser systems.

Table 3.2. Typical uncalibrated A-CRDS results. The errors shown are the average absolute error in the extinction measurement with each size measurement weighted equally.

Substance	λ (nm)	m_{ref} †	m_{fit} ‡	Avg absolute extinction error	Reference
Squalane	355	1.472 + 0.000i	1.454+0.001i	7.8%	This work
Nigrosin	532	1.70 +0.31i	Not reported	6.5%‡	Radney (2009)
Nigrosin	532	1.70 + 0.31i	1.72 + 0.28i (CW) 1.65 + 0.24i (pulsed)	3.8% 5.2%	Lang-Yona (2009)
$(NH_4)_2SO_4$	532	1.52 + 0.00i	1.52+0.00i (CW) 1.52 + 0.01i (pulsed)	2.6% 2.4%	Lang-Yona (2009)
Suwanee River Fulvic Acid (SRFA)	532	1.634 + 0.02i	1.520 + 0.02i (CW) 1.65 + 0.24i (pulsed)	24%* 8.1%	Lang-Yona (2009)
PSL	532	Not reported	1.60 + 0.01i (CW) 1.60 + 0.01i (pulsed)	4.5% 9.6%	Lang-Yona (2009)
PSL	560	1.5947 + 5 x 10^{-4}i	1.627 + 5 x 10^{-4}i**	11%	Miles (2010)
PSL	532	1.598 + 0i	Not reported	7.0%	Pettersson (2004)
DOS	532	1.4555 + 0i	1.455 + 0i	4.1%	Pettersson (2004)
DOS	355	1.470+0.000i	1.454+0.000i	6.2%	This work

†: Refractive index reported by author
‡: Limited to only two measurements that showed the best agreement with Mie theory
*: Discrepancies in the CW and pulsed measurements are attributed to SRFA sample differences
**: Fit was determined n only (k was fixed as 5 x 10^{-4}i)

As seen in Table 3.2., this level of precision was usually high enough to retrieve a refractive index to within 0.01 for n and k. To demonstrate the improvement in the proposed technique, a

comparison of the retrieved refractive index before and after calibration is depicted in Figure 3.4A. Of course the calibrated data should fit the refractive index from which it is converging, but it is interesting to note the improvement of the best fit. Initial errors in n and k are -0.018 and +0.001i, respectively, and χ_o^2 is reduced from 2860 to 8.601 by calibrating.

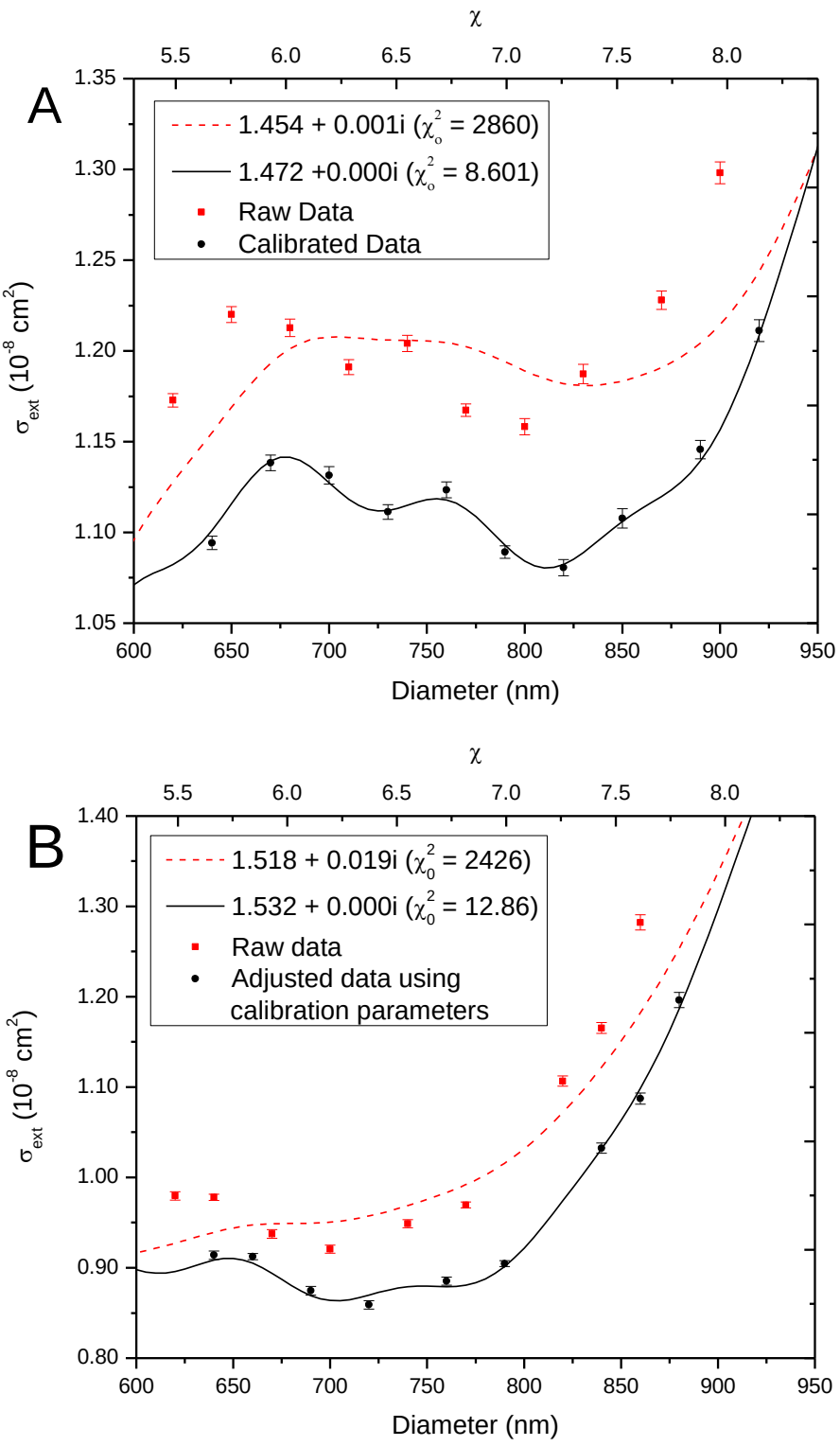

Figure 3.4. Fitted raw and calibrated data for squalane and squalene. A) Squalane measurements before and after calibration parameters are retrieved. B) Same-day measurements of squalene before and after calibration. In both cases, the best fit refractive index is shown.

To verify that this approach is valid, the same three calibration terms are applied to subsequent measurements of other aerosols. In the example shown above (Figure 3.4B), squalene is measured for a similar size range, and the calibrated terms retrieved with squalane are applied to the raw data. Once again, the best fit is noticeably better as χ_o^2 is reduced from 2426 to 12.86. The retrieved complex refractive index of 1.532 + 0.000i shows excellent agreement with the bulk measurement (n=1.530). Finally, the effect of calibration in retrieving a more accurate complex refractive index can be seen by the magnitude of error in the value of k. Squalene does not absorb at 355 nm, and yet the best fit for the raw data is 0.019i. Errors such as these could lead to false conclusions about the absorption properties of aerosols.

Table 3.3. Retrieved complex refractive indices after calibration.

Substance	n + ki	χ_o^2 / N_s	Avg Absolute σ_{ext} % Error	n_{ref}
Squalane**	$1.473^{+0.001}_{-0.001} + 0.000i^{+0.002i}_{-0.000i}$	1.22	0.72%	1.472† 1.471‡
DOS	$1.474^{+0.003}_{-0.002} + 0.000i^{+0.004i}_{-0.000i}$	0.49	0.67%	1.469† 1.470‡
Oleic Acid	$1.482^{+0.002}_{-0.001} + 0.000i^{+0.003i}_{-0.000i}$	0.87	0.89%	1.483†
Squalene (A)	$1.529^{+0.004}_{-0.003} + 0.000i^{+0.003i}_{-0.000i}$	0.54	0.90%	1.530‡
Squalene (B)	$1.532^{+0.001}_{-0.002} + 0.000i^{+0.002i}_{-0.000i}$	1.43	0.69%	
IL 1160	$1.510^{+0.007}_{-0.007} + 0.000i^{+0.006i}_{-0.000i}$	0.72	0.78%	1.515*

†: Snell's Law cell measurement
‡: Spectroscopic ellipsometer measurement
*: Reported refractive index from manufacturer
**: A second set of independent squalane measurements were taken after calibration

A-CRDS extinction measurements were collected for squalane and four other purely scattering liquids. In one trial, squalane was used to fit the calibration terms, and an independent trial of new squalane measurements were used to fit n and k. Squalene was measured on two

separate days and the similarities between the two measurements show the reproducibility of this technique. The retrieved complex refractive index was well within the uncertainty of the bulk measurement for all samples. IL 1160 is produced as a refractive index standard by mixing different proportions of phthalate esters, and it is speculated that the larger errors are due to the inhomogeneities of the aerosolized sample. A compilation of results is shown above in Table 3.2. The average absolute σ_{ext} error is less than one percent for each trial, and the χ_o^2/N_s is comparable in each case. The total number of particle size measurements ranged from 6 – 10 though it was observed that fewer were necessary to converge on the retrieved complex refractive index.

The uncertainty limits for the retrieved refractive index can also be displayed in a two dimensional n-k plane by plotting all χ^2 values at each evaluation point and comparing the values to the best fit (Figure 3.5). The relative sensitivity to the magnitude of n and k can be appreciated, and clearly the experimentally retrieved refractive indices show excellent agreement with the bulk reference.

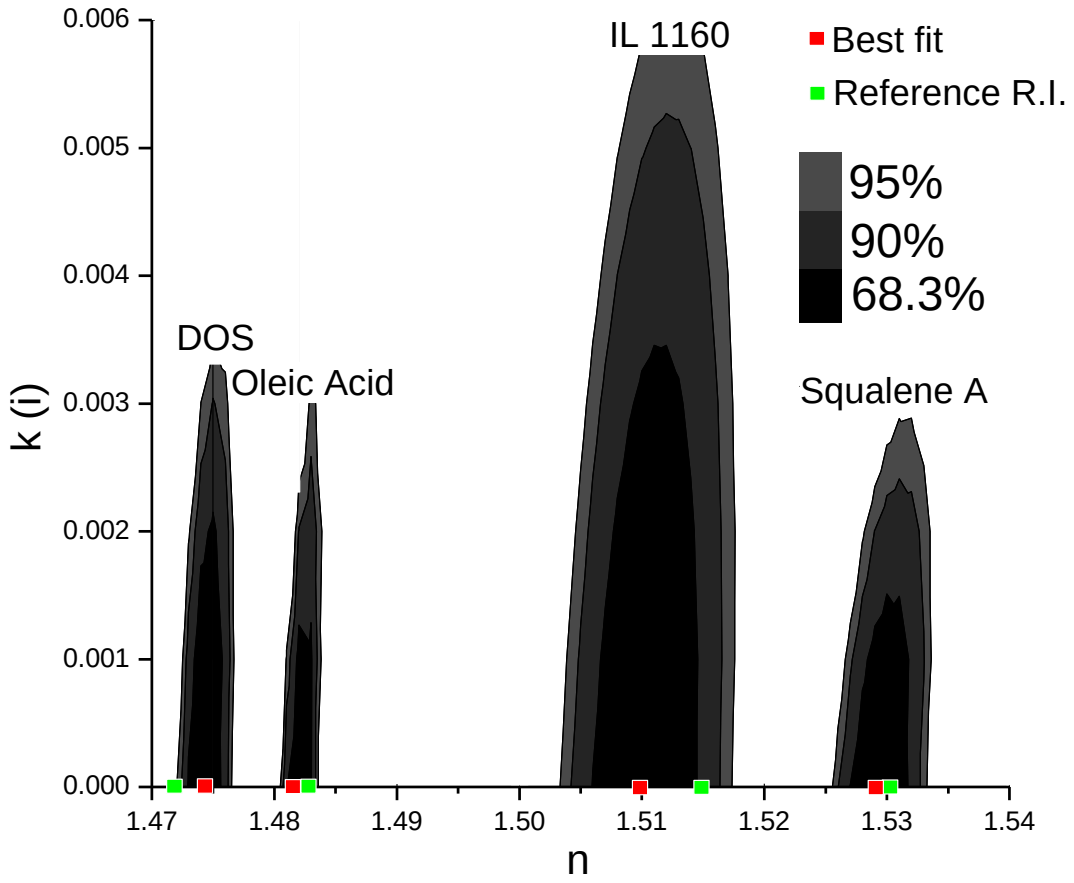

Figure 3.5. Complex refractive index contour plots of four trials. The outermost contour represents a 95% confidence limit.

3.4. Conclusions

A new A-CRDS technique has been demonstrated for determining optical properties of aerosols with the best precision reported to date. All trials had extinction cross section measurements with average absolute error of less than 1%. By collecting measurements at particle sizes most sensitive to changes in n and k, 95% confidence limits in the retrieved n and k are nearly an order of magnitude better than typically reported uncertainties. In fact, it is possible that the limiting factor in the measurement of optical properties may be the purity of the sample.

The feasibility of applying this calibration technique in other A-CRDS investigations is without question. The precision reported here was achieved with modestly reflective mirrors and a basic pulsed CRD setup. Faster repetition rates from CW modulated lasers could be used to reduce overall sampling time, though the trials reported here could be completed in a few hours. The total experimental time required can also be reduced by introducing a three-way valve system to immediately switch aerosol flows when purging the CRD cell and introducing particles.

This technique naturally leads to studies where measuring small changes in n and k are required. For example, the oxidation and aging process of species such as brown carbon could be studied to measure slight increases in absorption in the UV region. One could measure refractive indices over time to measure the effect of chemical interactions on optical properties, and the combination of this technique with mass spectrometry could shed light on the composition as well. This would also be useful to compare the results of the calibrated extinction measurements in studies where particles have been coated with liquids of different optical properties. Certainly, calibration could change the results of such measurements when Δ_{diam} is the same order of magnitude as the coating layers on submicron particles. Regardless of the investigation, improved precision in characterizing aerosol optical properties will aid the understanding of their implications on the atmosphere.

CHAPTER 4

CONCLUSIONS AND FUTURE DIRECTIONS

4.1. Conclusions

The initial goal in the development of this UV A-CRDS instrument was to make precision extinction measurements of organic liquids to shed light on the true absorption characteristics at lower wavelengths. Current aerosol models insufficiently account for the absorption of aerosols such as brown carbon, and in-situ particle measurements can provide a clearer measure of their impact on the global radiative balance[130]. And though light absorbing substances have not yet been measured, the instrument has now been well characterized so that statistical uncertainties have been separated from systematic errors. This precision is necessary to differentiate small, real increases in absorption from day-to-day changes in the measured extinction from instrument fluctuations and flow conditions.

The calculated light extinction inside a resonating optical cavity is an absolute measurement. The comparison of the empty cell ring-down time to a faster exponential decay when additional losses exist should not require calibration. The calculated sensitivity of this instrument may be deceiving when applying these measurements to aerosols. The assumptions of the flow conditions, in terms of long-term stability and effective particle paths, as well as errors in the measured particle concentration can dominate the measurement uncertainties. Here, we have calibrated an A-CRDS system by using liquid squalane particles as a refractive index standard. The excellent fit of the empirical Cauchy dispersion equation to Snell's law cell and ellipsometry measurements allows for the application of squalane (or any other measured liquid) as a calibrant

at any wavelength. This calibration method with squalane was shown to apply to subsequent extinction measurements for other liquid particles. Average absolute σ_{ext} errors were reduced from 5-10% to less than 1% after calibration parameters adjusted the measured raw measurement. For the first time, the uncertainty at each step was propagated into the fitting algorithm that retrieves a complex refractive index. Furthermore, the results reported here were achieved with modestly reflective CRD mirrors. Comparably-priced mirrors are available for visible wavelengths with reflectivities several orders of magnitude better than the ones used in this study.

The calibration technique is also a universal approach for A-CRDS studies that use a DMA and CPC. A unique result of the calibration study is the ability to simultaneously characterize a single DMA with this technique. In previous studies, the size distribution of size-selected aerosols was approximated and there was little discussion in the literature about the effect of the uncertainty of the narrowness of the size distribution [34, 35, 54, 58, 74]. Even when the output of the DMA was considered in a tandem DMA arrangement, the transfer function and peak size accuracy was not deconvolved[60]. Clearly, as precision is improved, uncertainty in the presumed size distribution will become a larger source of error in the retrieved refractive index.

The errors in A-CRDS are often reported in terms of the retrieved refractive index, and this is not an appropriate measure of the instrument's capabilities. First, n and k are retrieved *simultaneously* by comparison to their respective extinction curve. The uncertainty in each term will be unique, so uncertainty limits for n and k will be a more useful metric than a percent error. Second, extinction curves that are predicted with Mie theory have oscillatory behavior for monodisperse particles. For this reason some extinction measurements would be identical at sizes where the different extinction curves intersect. That is to say a quoted sensitivity to n or k

is meaningless without information about the particle sizes measured. Finally, the true measure of the instrument is its ability to differentiate σ_{ext} measurements, and this value does not depend on the complex refractive index of the aerosol.

4.2. Future directions

Moving forward in better characterizing the optical properties of aerosols, the A-CRDS techniques described here should be compared with other in-situ scattering and absorption measurements. The technology is available to simultaneously flow particles through the CRD cell and a photoacoustic (PAS) cell or nephelometer to directly measure the absorbing and scattering components of extinction[26, 64]. Also, absorption of a bulk liquid sample can be measured at several concentrations with a UV-Vis spectrophotometer to measure a molar absorptivity (ε, cm^{-1} M^{-1}). The absorption coefficient (α_{abs}, cm^{-1}) is related to the imaginary component of the refractive index at a given wavelength with[56]:

$$\alpha_{ext} = \frac{4\pi k}{\lambda} \tag{4.1}$$

Therefore, changes in the absorption of a bulk measurement could be compared to the retrieved refractive index. A useful example would be the increased absorption of an increasingly oxidized organic substance. In a way, A-CRDS measurements of these substances might provide a glimpse at how atmospheric aerosol "aging" changes its optical properties in time. Improved absorption measurements will have important implications for the modeled aerosol direct effect on net radiative forcing.

To gain more information about how optical properties are influenced by aerosol composition, A-CRDS studies could be combined with mass spectrometry. Soft ionization techniques[131] will allow organic aerosols to be studied simultaneously as particle are reacted. This could potentially describe relationships between functional groups and polarizability of the

electron cloud to their optical properties. A multi-wavelength CRD system in conjunction with PAS, nephelometry, and mass spectrometry may appear to be a daunting experimental setup, and it surely would be, but such investigations will be required to improve the understanding of the interaction of aerosols with light in the atmosphere.

Past studies of optical properties of mixed and coated particles should be revisited with a calibrated instrument such that inappropriate conclusions are not reached. It is important that one does not assign systematic measurement errors to statistical uncertainty. All too often the uncertainty limit is explained by the investigator in terms of a required ring-down time instead of considering other assumptions. Highly-reflective mirrors required for CRDS are available from the deep UV to the mid IR[46], so the applications of this instrument are limited by the imagination of the investigator. The most compelling attributes of the A-CRDS system are its simplicity, versatility, and high sensitivity. The purpose of this work was to obtain higher levels of precision, and in doing so, investigations of the morphology and physical properties of aerosols may be better understood with the techniques described. Hopefully, these techniques will facilitate such future developments in the field of atmospheric chemistry.

CHAPTER 5

REFERENCES

1. Finlayson-Pitts, B.P., J., *Chemistry of the Upper and Lower Atmosphere: Theory, Experiments, and Applications*1999, London, UK: Academic Press.

2. Ramaswamy, V.B., Olivier; Haigh, J.; Hauglustaine, D.; Haywood, J.; Myhre, G.; Nakajima, Takahito; Shi, Guangyu; Solomon, S.; Betts, Robert E.; Charlson, R.; Chuang, C. C.; Daniel, J. S.; Del Genio, Anthony D.; Feichter, J.; Fuglestvedt, J.; Forster, P. M.; Ghan, Steven J.; Jones, A.; Kiehl, J. T.; Koch, D.; Land, C.; Lean, J.; Lohmann, Ulrike; Minschwaner, K.; Penner, Joyce E.; Roberts, D. L.; Rodhe, H.; Roelofs, G.-J.; Rotstayn, Leon D.; Schneider, T. L.; Schumann, U.; Schwartz, Stephen E.; Schwartzkopf, M. D.; Shine, K. P.; Smith, Steven J.; Stevenson, D. S.; Stordal, F.; Tegen, I.; van Dorland, R.; Zhang, Y.; Srinivasan, J.; Joos, Fortunat, *IPCC Third Assessment Report Climate Change 2001: The Scientific Basis*2001: Houghton, J. T. et al; Cambridge University Press, New York, NY, United States(US).

3. Forster, P.R., V.; Artaxo, P.; Berntsen, T.; Betts, R.; Fahey, D. W.; Haywood, J.; Lean, J.; Lowe, D. C.; Myhre, G.; Nganga, J.; Prinn, R.; Raga, G.; Schulz, M.; Van Dorland, R., *Changes in Atmospheric Constituents and in Radiative Forcing. In Climate Change 2007: The Physical Science Basis. .* Contribution of Working Group I to the Fourth Assessment Report of the IntergoVernmental Panel on Climate Change, ed. S. Solomon, Qin, D., Manning, M., Chen, Z., Marquis, M., Averyt, K. B., Tignor, M., Miller, H. L.2007, New York: Cambridge University Press.

4. Rogge, W.F., et al., *Quantification of Urban Organic Aerosols at a Molecular-Level - Identification, Abundance and Seasonal-Variation.* Atmospheric Environment Part a-General Topics, 1993. **27**(8): p. 1309-1330.

5. Twomey, S., *Pollution and Planetary Albedo.* Atmospheric Environment, 1974. **8**(12): p. 1251-1256.

6. Pincus, R. and M.B. Baker, *Effect of Precipitation on the Albedo Susceptibility of Clouds in the Marine Boundary-Layer.* Nature, 1994. **372**(6503): p. 250-252.

7. Albrecht, B.A., *Aerosols, Cloud Microphysics, and Fractional Cloudiness.* Science, 1989. **245**(4923): p. 1227-1230.

8. Ackerman, A.S., et al., *Effects of aerosols on cloud albedo: Evaluation of Twomey's parameterization of cloud susceptibility using measurements of ship tracks.* Journal of the Atmospheric Sciences, 2000. **57**(16): p. 2684-2695.

9. Ramanathan, V., et al., *Atmospheric brown clouds: Impacts on South Asian climate and hydrological cycle.* Proceedings of the National Academy of Sciences of the United States of America, 2005. **102**(15): p. 5326-5333.

10. Hansen, J.E., et al., *Climate forcings in the Industrial era.* Proceedings of the National Academy of Sciences of the United States of America, 1998. **95**(22): p. 12753-12758.

11. Chylek, P. and J. Wong, *Effect of Absorbing Aerosols on Global Radiation Budget.* Geophysical Research Letters, 1995. **22**(8): p. 929-931.

12. Jacobson, M.Z., *Global direct radiative forcing due to multicomponent anthropogenic and natural aerosols.* Journal of Geophysical Research-Atmospheres, 2001. **106**(D2): p. 1551-1568.

13. Lock, J.A. and G. Gouesbet, *Generalized Lorenz-Mie theory and applications.* Journal of Quantitative Spectroscopy & Radiative Transfer, 2009. **110**(11): p. 800-807.

14. Andreae, M.O. and A. Gelencser, *Black carbon or brown carbon? The nature of light-absorbing carbonaceous aerosols.* Atmospheric Chemistry and Physics, 2006. **6**: p. 3131-3148.

15. Hoffer, A., et al., *Optical properties of humic-like substances (HULIS) in biomass-burning aerosols.* Atmospheric Chemistry and Physics, 2006. **6**: p. 3563-3570.

16. McMurry, P.H., *A review of atmospheric aerosol measurements.* Atmospheric Environment, 2000. **34**(12-14): p. 1959-1999.

17. Moosmuller, H., R.K. Chakrabarty, and W.P. Arnott, *Aerosol light absorption and its measurement: A review.* Journal of Quantitative Spectroscopy & Radiative Transfer, 2009. **110**(11): p. 844-878.

18. Ballach, J., et al., *Development of an improved optical transmission technique for black carbon (BC) analysis.* Atmospheric Environment, 2001. **35**(12): p. 2089-2100.

19. Hansen, A.D.A., H. Rosen, and T. Novakov, *The Aethalometer - an Instrument for the Real-Time Measurement of Optical-Absorption by Aerosol-Particles.* Science of the Total Environment, 1984. **36**(Jun): p. 191-196.

20. Bond, T.C., T.L. Anderson, and D. Campbell, *Calibration and intercomparison of filter-based measurements of visible light absorption by aerosols.* Aerosol Science and Technology, 1999. **30**(6): p. 582-600.

21. Reid, J.S., et al., *Comparisons of techniques for measuring shortwave absorption and black carbon content of aerosols from biomass burning in Brazil.* Journal of Geophysical Research-Atmospheres, 1998. **103**(D24): p. 32031-32040.

22. Truex, T.J. and J.E. Anderson, *Mass Monitoring of Carbonaceous Aerosols with a Spectrophone.* Atmospheric Environment, 1979. **13**(4): p. 507-509.

23. Yasa, Z., et al., *Photoacoustic Investigation of Urban Aerosol-Particles.* Applied Optics, 1979. **18**(15): p. 2528-2530.

24. Arnott, W.P., et al., *Photoacoustic spectrometer for measuring light absorption by aerosol: instrument description.* Atmospheric Environment, 1999. **33**(17): p. 2845-2852.

25. Lack, D.A., et al., *Aerosol absorption measurement using photoacoustic spectroscopy: Sensitivity, calibration, and uncertainty developments.* Aerosol Science and Technology, 2006. **40**(9): p. 697-708.

26. Lack, D.A., et al., *Absorption Enhancement of Coated Absorbing Aerosols: Validation of the Photo-Acoustic Technique for Measuring the Enhancement.* Aerosol Science and Technology, 2009. **43**(10): p. 1006-1012.

27. Schnaiter, M., et al., *Measurement of wavelength-resolved light absorption by aerosols utilizing a UV-VIS extinction cell.* Aerosol Science and Technology, 2005. **39**(3): p. 249-260.

28. Petzold, A., et al., *Evaluation of multiangle absorption photometry for measuring aerosol light absorption.* Aerosol Science and Technology, 2005. **39**(1): p. 40-51.

29. Arnott, W.P., et al., *Photoacoustic and filter-based ambient aerosol light absorption measurements: Instrument comparisons and the role of relative humidity.* Journal of Geophysical Research-Atmospheres, 2003. **108**(D1).

30. Sheridan, P.J., et al., *The Reno Aerosol Optics Study: An evaluation of aerosol absorption measurement methods.* Aerosol Science and Technology, 2005. **39**(1): p. 1-16.

31. Anderson, T.L., et al., *Performance characteristics of a high-sensitivity, three-wavelength, total scatter/backscatter nephelometer.* Journal of Atmospheric and Oceanic Technology, 1996. **13**(5): p. 967-986.

32. Massoli, P., et al., *Uncertainty in Light Scattering Measurements by TSI Nephelometer: Results from Laboratory Studies and Implications for Ambient Measurements.* Aerosol Science and Technology, 2009. **42**(11): p. 1064-1074.

33. Bond, T.C., D.S. Covert, and T. Muller, *Truncation and Angular-Scattering Corrections for Absorbing Aerosol in the TSI 3563 Nephelometer.* Aerosol Science and Technology, 2009. **43**(9): p. 866-871.

34. Brown, S.S., *Absorption spectroscopy in high-finesse cavities for atmospheric studies.* Chemical Reviews, 2003. **103**(12): p. 5219-5238.

35. Atkinson, D.B., *Solving chemical problems of environmental importance using cavity ring-down spectroscopy.* Analyst, 2003. **128**(2): p. 117-125.

36. Ramponi, A.J., et al., *High-Sensitivity Atmospheric Transmission Measurements Using a Cavity Ringdown Technique.* Applied Optics, 1988. **27**(22): p. 4606-4608.

37. Okeefe, A. and O. Lee, *Trace Gas-Analysis by Pulsed Laser-Absorption Spectroscopy.* American Laboratory, 1989. **21**(12): p. 19-22.

38. Berden, G., R. Peeters, and G. Meijer, *Cavity-enhanced absorption spectroscopy of the 1.5 mu m band system of jet-cooled ammonia.* Chemical Physics Letters, 1999. **307**(3-4): p. 131-138.

39. Jongma, R.T., et al., *Trace Gas-Detection with Cavity Ring down Spectroscopy.* Review of Scientific Instruments, 1995. **66**(4): p. 2821-2828.

40. Miles, R.E.H., et al., *Sources of Error and Uncertainty in the Use of Cavity Ring Down Spectroscopy to Measure Aerosol Optical Properties.* Aerosol Science and Technology, 2011. **45**(11): p. 1360-1375.

41. Arola, A., et al., *Inferring absorbing organic carbon content from AERONET data.* Atmospheric Chemistry and Physics, 2011. **11**(1): p. 215-225.

42. Radney, J.G., et al., *Laboratory Validation of Aerosol Extinction Coefficient Measurements by a Field-Deployable Pulsed Cavity Ring-Down Transmissometer.* Aerosol Science and Technology, 2009. **43**(1): p. 71-80.

43. Okeefe, A. and D.A.G. Deacon, *Cavity Ring-down Optical Spectrometer for Absorption-Measurements Using Pulsed Laser Sources.* Review of Scientific Instruments, 1988. **59**(12): p. 2544-2551.

44. Scherer, J.J., et al., *Cavity ringdown laser absorption spectroscopy: History, development, and application to pulsed molecular beams.* Chemical Reviews, 1997. **97**(1): p. 25-51.

45. Zalicki, P. and R.N. Zare, *Cavity Ring-down Spectroscopy for Quantitative Absorption-Measurements.* Journal of Chemical Physics, 1995. **102**(7): p. 2708-2717.

46. Wheeler, M.D., et al., *Cavity ring-down spectroscopy.* Journal of the Chemical Society-Faraday Transactions, 1998. **94**(3): p. 337-351.

47. Mazurenka, M., Orr-Ewing, A., Peverall, R., and Ritchie, G., *Cavity Ring-down and Cavity Enhanced Spectroscopy Using Diode Lasers.* Annu. Rep. Prog. Chem., Sect. C, 2005. **101**: p. 100-142.

48. Busch, K.W., Busch, M. A., ed. *Cavity Ringdown Spectroscopy: An Ultratrace-Absorption Measurement Technique*. ACS Symposium Series1999, Oxford University Press: Washington, DC.

49. Sappey, A.D., et al., *Fixed-frequency cavity ringdown diagnostic for atmospheric particulate matter.* Optics Letters, 1998. **23**(12): p. 954-956.

50. Vander Wal, R.L. and T.M. Ticich, *Cavity ringdown and laser-induced incandescence measurements of soot.* Applied Optics, 1999. **38**(9): p. 1444-1451.

51. Naus, H. and W. Ubachs, *Experimental verification of Rayleigh scattering cross sections.* Optics Letters, 2000. **25**(5): p. 347-349.

52. Thompson, J.E., B.W. Smith, and J.D. Winefordner, *Monitoring atmospheric particulate matter through cavity ring-down spectroscopy.* Analytical Chemistry, 2002. **74**(9): p. 1962-1967.

53. Bulatov, V., M. Fisher, and I. Schechter, *Aerosol analysis by cavity-ring-down laser spectroscopy.* Analytica Chimica Acta, 2002. **466**(1): p. 1-9.

54. Pettersson, A., et al., *Measurement of aerosol optical extinction at 532nm with pulsed cavity ring down spectroscopy.* Journal of Aerosol Science, 2004. **35**(8): p. 995-1011.

55. Haywood, J. and O. Boucher, *Estimates of the direct and indirect radiative forcing due to tropospheric aerosols: A review.* Reviews of Geophysics, 2000. **38**(4): p. 513-543.

56. Bohren, C.F.a.H., D. R., *Absorption and Scattering of Light by Small Particles*1998, New York: Wiley.

57. Baynard, T., et al., *Design and application of a pulsed cavity ring-down aerosol extinction spectrometer for field measurements.* Aerosol Science and Technology, 2007. **41**(4): p. 447-462.

58. Riziq, A.A., et al., *Optical properties of absorbing and non-absorbing aerosols retrieved by cavity ring down (CRD) spectroscopy.* Atmospheric Chemistry and Physics, 2007. **7**(6): p. 1523-1536.

59. Rudic, S., et al., *Optical properties of micrometer size water droplets studied by cavity ringdown spectroscopy.* Applied Optics, 2007. **46**(24): p. 6142-6150.

60. Spindler, C., A.A. Riziq, and Y. Rudich, *Retrieval of aerosol complex refractive index by combining cavity ring down aerosol spectrometer measurements with full size distribution information.* Aerosol Science and Technology, 2007. **41**(11): p. 1011-1017.

61. Dinar, E., et al., *The complex refractive index of atmospheric and model humic-like substances (HULIS) retrieved by a cavity ring down aerosol spectrometer (CRD-AS).* Faraday Discussions, 2008. **137**: p. 279-295.

62. Riziq, A.A., et al., *Extinction efficiencies of coated absorbing aerosols measured by cavity ring down aerosol spectrometry.* Atmospheric Chemistry and Physics, 2008. **8**(6): p. 1823-1833.

63. Nakayama, T., et al., *Measurements of aerosol optical properties in central Tokyo during summertime using cavity ring-down spectroscopy: Comparison with conventional techniques.* Atmospheric Environment, 2010. **44**(25): p. 3034-3042.

64. Langridge, J.M., et al., *Aircraft Instrument for Comprehensive Characterization of Aerosol Optical Properties, Part I: Wavelength-Dependent Optical Extinction and Its Relative Humidity Dependence Measured Using Cavity Ringdown Spectroscopy.* Aerosol Science and Technology, 2011. **45**(11): p. 1305-1318.

65. Nakayama, T., et al., *Laboratory studies on optical properties of secondary organic aerosols generated during the photooxidation of toluene and the ozonolysis of alpha-pinene.* Journal of Geophysical Research-Atmospheres, 2010. **115**.

66. Li, L., et al., *Monitoring optical properties of aerosols with cavity ring-down spectroscopy.* Journal of Aerosol Science, 2011. **42**(4): p. 277-284.

67. Strawa, A.W., et al., *The measurement of aerosol optical properties using continuous wave cavity ring-down techniques.* Journal of Atmospheric and Oceanic Technology, 2003. **20**(4): p. 454-465.

68. Moosmuller, H., R. Varma, and W.P. Arnott, *Cavity ring-down and cavity-enhanced detection techniques for the measurement of aerosol extinction.* Aerosol Science and Technology, 2005. **39**(1): p. 30-39.

69. Richman, B.A., et al., *Novel detection of aerosols: combined cavity ring-down and fluorescence spectroscopy.* Optics Express, 2005. **13**(9): p. 3376-3387.

70. Hallar, A.G., et al., *Atmospheric Radiation Measurements Aerosol Intensive Operating Period: Comparison of aerosol scattering during coordinated flights.* Journal of Geophysical Research-Atmospheres, 2006. **111**(D5).

71. Butler, T.J.A., J.L. Miller, and A.J. Orr-Ewing, *Cavity ring-down spectroscopy measurements of single aerosol particle extinction. I. The effect of position of a particle within the laser beam on extinction.* Journal of Chemical Physics, 2007. **126**(17).

72. Sanford, T.J., et al., *Albedo measurements and optical sizing of single aerosol particles.* Aerosol Science and Technology, 2008. **42**(11): p. 958-969.

73. Butler, T.J.A., et al., *Optical-Feedback Cavity Ring-Down Spectroscopy Measurements of Extinction by Aerosol Particles.* Journal of Physical Chemistry A, 2009. **113**(16): p. 3963-3972.

74. Lang-Yona, M., et al., *Complex Refractive Indices of Aerosols Retrieved by Continuous Wave-Cavity Ring Down Aerosol Spectrometer.* Analytical Chemistry, 2009. **81**(5): p. 1762-1769.

75. Miles, R.E.H., et al., *Measurements of the wavelength dependent extinction of aerosols by cavity ring down spectroscopy.* Physical Chemistry Chemical Physics, 2010. **12**(15): p. 3914-3920.

76. Adler, G., et al., *Effect of intrinsic organic carbon on the optical properties of fresh diesel soot.* Proceedings of the National Academy of Sciences of the United States of America, 2010. **107**(15): p. 6699-6704.

77. Mellon, D., et al., *Measurements of Extinction by Aerosol Particles in the Near-Infrared Using Continuous Wave Cavity Ring-Down Spectroscopy.* Journal of Physical Chemistry A, 2011. **115**(5): p. 774-783.

78. Khalizov, A.F., et al., *Enhanced Light Absorption and Scattering by Carbon Soot Aerosol Internally Mixed with Sulfuric Acid.* Journal of Physical Chemistry A, 2009. **113**(6): p. 1066-1074.

79. Freedman, M.A., et al., *Optical Properties of Internally Mixed Aerosol Particles Composed of Dicarboxylic Acids and Ammonium Sulfate.* Journal of Physical Chemistry A, 2009. **113**(48): p. 13584-13592.

80. Lack, D.A. and C.D. Cappa, *Impact of brown and clear carbon on light absorption enhancement, single scatter albedo and absorption wavelength dependence of black carbon.* Atmospheric Chemistry and Physics, 2010. **10**(9): p. 4207-4220.

81. Lang-Yona, N., et al., *Interaction of internally mixed aerosols with light.* Physical Chemistry Chemical Physics, 2010. **12**(1): p. 21-31.

82. Lang-Yona, N., et al., *The chemical and microphysical properties of secondary organic aerosols from Holm Oak emissions.* Atmospheric Chemistry and Physics, 2010. **10**(15): p. 7253-7265.

83. Brem, B.T., et al., *Laboratory-Measured Optical Properties of Inorganic and Organic Aerosols at Relative Humidities up to 95%.* Aerosol Science and Technology, 2012. **46**(2): p. 178-190.

84. Trainic, M.A.R., A.; Lavi, A.; Rudich, Y., *Role of Interfacial Water in the Heterogenous Uptake of Glyoxal by Mixed Glycine and Ammonium Sulfate Aerosols.* Journal of Physical Chemistry A, 2012.

85. Miles, R.E.H., et al., *Influence of Uncertainties in the Diameter and Refractive Index of Calibration Polystyrene Beads on the Retrieval of Aerosol Optical Properties Using Cavity Ring Down Spectroscopy.* Journal of Physical Chemistry A, 2010. **114**(26): p. 7077-7084.

86. TSI, I., *CPC Operation and Service Manual (Rev. G)*. Model 37752010.

87. Kozma, I.Z., P. Krok, and E. Riedle, *Direct measurement of the group-velocity mismatch and derivation of the refractive-index dispersion for a variety of solvents in the ultraviolet.* Journal of the Optical Society of America B-Optical Physics, 2005. **22**(7): p. 1479-1485.

88. Painter, L.R., et al., *Vacuum Ultraviolet Optical-Properties of Squalane and Squalene.* Journal of Applied Physics, 1984. **55**(3): p. 756-759.

89. Azzam, R.M.A.a.B., N. M., *Ellipsometry and Polarized Light*1997, Amsterdam: North-Hollard.

90. Sorensen, N.A., et al., *Studies Related to Pristane .6. Synthesis of Digeranyl with Some Remarks on the Physical Constants of Crocetane.* Acta Chemica Scandinavica, 1951. **5**(5): p. 757-765.

91. Hinds, W.C., *Aerosol Technology: Properties, Behavoir, and Measurement of Airborne Particles*1999, New York: Wiley.

92. Fuchs, N.A., *On the Stationary Charge Distribution on Aerosol Particles in a Bipolar Ionic Atmosphere.* Pure and Applied Geophysics, 1963. **56**(1): p. 185-193.

93. Wiedensohler, A., et al., *Investigation of the Bipolar Charge-Distribution at Various Gas Conditions.* Journal of Aerosol Science, 1986. **17**(3): p. 413-416.

94. Wiedensohler, A., *An Approximation of the Bipolar Charge-Distribution for Particles in the Sub-Micron Size Range.* Journal of Aerosol Science, 1988. **19**(3): p. 387-389.

95. Kim, J.H., et al., *Slip correction measurements of certified PSL nanoparticles using a nanometer differential mobility analyzer (nano-DMA) for Knudsen number from 0.5 to 83.* Journal of Research of the National Institute of Standards and Technology, 2005. **110**(1): p. 31-54.

96. KNUTSON, E. and K. WHITBY, *Aerosol classification by electric mobility: apparatus, theory, and applications.* Journal of Aerosol Science, 1975. **6**: p. 443-451.

97. Baron, P.A., and Willeke, K., *Aerosol Measurement: Principles, Techniques, and Applications (2nd ed.)*2001, New York: Wiley.

98. Berden, G.a.E., R., *Cavity Ring-Down Spectroscopy: Techniques and Applications*2009, Oxford: Wiley.

99. Lee, D.H., et al., *Optimization of the mode matching in pulsed cavity ringdown spectroscopy by monitoring non-degenerate transverse mode beating.* Applied Physics B-Lasers and Optics, 2002. **74**(4-5): p. 435-440.

100. Halmer, D., et al., *Fast exponential fitting algorithm for real-time instrumental use.* Review of Scientific Instruments, 2004. **75**(6): p. 2187-2191.

101. Everest, M.A. and D.B. Atkinson, *Discrete sums for the rapid determination of exponential decay constants.* Review of Scientific Instruments, 2008. **79**(2).

102. Press, W.H.e.a., *Numerical Recipes: The Art of Scientific Computing*. Third Edition ed2007, New York, NY: Cambridge University Press.

103. Lompado, A.; Available from: http://diogenes.iwt.uni-bremen.de/vt/laser/wriedt/Mie_Type_Codes/body_mie_type_codes.html.

104. Brown, S.S., et al., *Simultaneous in situ detection of atmospheric NO3 and N2O5 via cavity ring-down spectroscopy.* Review of Scientific Instruments, 2002. **73**(9): p. 3291-3301.

105. Maron, S.H., C. Moore, and A.S. Powell, *Electron Microscopy of Synthetic Latices.* Journal of Applied Physics, 1952. **23**(8): p. 900-905.

106. Bradford, E.B. and J.W. Vanderhoff, *Electron Microscopy of Monodisperse Latexes.* Journal of Applied Physics, 1955. **26**(7): p. 864-871.

107. Yamada, Y., K. Miyamoto, and A. Koizumi, *Size Determination of Latex-Particles by Electron-Microscopy.* Aerosol Science and Technology, 1985. **4**(2): p. 227-232.

108. Duke, S.D., Layendecker, E. B. , *Technical Note TN-010.02A: Internal Standard Method for Size Calibration of Sub-micrometer Spherical Particles by Electron Microscopy.* Thermo Scientific, 2003.

109. Mulholland, G.W., et al., *Measurement of 100 nm and 60 nm particle standards by differential mobility analysis.* Journal of Research of the National Institute of Standards and Technology, 2006. **111**(4): p. 257-312.

110. Sax, K.J. and F.H. Stross, *Squalane - a Standard.* Analytical Chemistry, 1957. **29**(11): p. 1700-1702.

111. Kostinski, A.B., *On the extinction of radiation by a homogeneous but spatially correlated random medium.* Journal of the Optical Society of America a-Optics Image Science and Vision, 2001. **18**(8): p. 1929-1933.

112. Larsen, M.L., *Spatial distributions of aerosol particles: Investigation of the Poisson assumption.* Journal of Aerosol Science, 2007. **38**(8): p. 807-822.

113. Martinsson, B.G., M.N.A. Karlsson, and G. Frank, *Methodology to estimate the transfer function of individual differential mobility analyzers.* Aerosol Science and Technology, 2001. **35**(4): p. 815-823.

114. DeCarlo, P.F., et al., *Particle morphology and density characterization by combined mobility and aerodynamic diameter measurements. Part 1: Theory.* Aerosol Science and Technology, 2004. **38**(12): p. 1185-1205.

115. Kinney, P.D., et al., *Use of the Electrostatic Classification Method to Size 0.1 Mu-M Srm Particles - a Feasibility Study.* Journal of Research of the National Institute of Standards and Technology, 1991. **96**(2): p. 147-176.

116. Allen, M.D. and O.G. Raabe, *Re-Evaluation of Millikan Oil Drop Data for the Motion of Small Particles in Air.* Journal of Aerosol Science, 1982. **13**(6): p. 537-547.

117. Allen, M.D. and O.G. Raabe, *Slip Correction Measurements of Spherical Solid Aerosol-Particles in an Improved Millikan Apparatus.* Aerosol Science and Technology, 1985. **4**(3): p. 269-286.

118. Rader, D.J., *Momentum Slip Correction Factor for Small Particles in 9 Common Gases.* Journal of Aerosol Science, 1990. **21**(2): p. 161-168.

119. Hering, S.V. and P.H. Mcmurry, *Optical Counter Response to Monodisperse Atmospheric Aerosols.* Atmospheric Environment Part a-General Topics, 1991. **25**(2): p. 463-468.

120. Alshawa, A., et al., *Hygroscopic Growth and Deliquescence of NaCl Nanoparticles Coated with Surfactant AOT.* Journal of Physical Chemistry A, 2009. **113**(26): p. 7678-7686.

121. Anttila, T., et al., *Size-dependent activation of aerosols into cloud droplets at a subarctic background site during the second Pallas Cloud Experiment (2nd PaCE): method development and data evaluation.* Atmospheric Chemistry and Physics, 2009. **9**(14): p. 4841-4854.

122. Harmon, C.W., et al., *Hygroscopic Growth and Deliquescence of NaCl Nanoparticles Mixed with Surfactant SDS.* Journal of Physical Chemistry B, 2010. **114**(7): p. 2435-2449.

123. Stolzenburg, M.R., *An Ultrafine Aerosol Size Distribution Measuring System*, 1988, University of Minnesota, MN.

124. Chen, D.R. and D.Y.H. Pui, *Numerical modeling of the performance of differential mobility analyzers for nanometer aerosol measurements.* Journal of Aerosol Science, 1997. **28**(6): p. 985-1004.

125. Eichler, T., L. de Juan, and J.F. de la Mora, *Improvement of the resolution of TSI's 3071 DMA via redesigned sheath air and aerosol inlets.* Aerosol Science and Technology, 1998. **29**(1): p. 39-49.

126. Karlsson, M.N.A. and B.G. Martinsson, *Methods to measure and predict the transfer function size dependence of individual DMAs.* Journal of Aerosol Science, 2003. **34**(5): p. 603-625.

127. Fissan, H., et al., *Analytical and empirical transfer functions of a simplified spectrometre de mobilite electrique circulaire (SMEC) for nano particles.* Journal of Aerosol Science, 1998. **29**(3): p. 289-293.

128. Li, W.L., L. Li, and D.R. Chen, *Technical note: A new deconvolution scheme for the retrieval of true DMA transfer function from tandem DMA data.* Aerosol Science and Technology, 2006. **40**(12): p. 1052-1057.

129. Smith, J.D. and D.B. Atkinson, *A portable pulsed cavity ring-down transmissometer for measurement of the optical extinction of the atmospheric aerosol.* Analyst, 2001. **126**(8): p. 1216-1220.

130. Jacobson, M.Z., *Isolating nitrated and aromatic aerosols and nitrated aromatic gases as sources of ultraviolet light absorption.* Journal of Geophysical Research-Atmospheres, 1999. **104**(D3): p. 3527-3542.

131. Hearn, J.D. and G.D. Smith, *A chemical ionization mass spectrometry method for the online analysis of organic aerosols.* Analytical Chemistry, 2004. **76**(10): p. 2820-2826.

APPENDIX A

MIE THEORY CALCULATIONS AND χ^2 MINIMIZATION ALGORITHMS

A.1. Theoretical extinction curves

The basis for all calculations is the theoretical extinction of a particle using Lorentz-Mie theory. A Mathematica script (Lampado 2003) is used to calculate the extinction cross section for a given particle diameter and illumination wavelength. "Mie files" were created for each complex refractive index ($1.300 \leq n \leq 1.700$ and $0.000i \leq k \leq 0.200i$) with an extinction cross section calculated for each particle diameter from 5 nm to 1200 nm in 5 nm steps. The text files use the naming convention "n####k#". Therefore a complex refractive index of 1.530+ 0.000i has a Mie file labeled "n1530k0". These files would strictly apply to the extinction curve of an exact particle size, so a log-normal distribution of the particle sizes will take into account the effective extinction cross section at any peak particle diameter. To simulate the effect of a distribution of particle sizes around a peak (i.e. mean diameter), a Mathematica script applies a log-normal distribution to the Mie file cross sections for each 5 nm size bin. Shown in Figure A.1., the only required inputs to this Mathematica script are: 1) the directory path for the referenced Mie files, 2) the geometric standard deviation (σ_1), and 3) the Mie file of the appropriate complex refractive index. The effective extinction curve is plotted for particles ranging from 0 to 1200 nm in diameter, but the tail edges of broader distributions will be clipped near the limits of the plot. For example, a peak particle diameter of 1100 nm with $\sigma_{geo} = 1.05$ will have a significant portion (>5%) of particles larger than 1200 nm. Finally, the new extinction curves can be exported as .csv files for graphical comparison with data.

Log – normal Particle Size Distribution

```
In[43]:= Off[General::spell1];
         SetDirectory["C:\\New Mie Files"]
Out[44]= C:\New Mie Files

In[45]:= σ1 = 1.040;          (* geometric standard deviation *)

In[46]:= ext = ReadList["n1472k0", Number];
         mielist = {};

         Do[size1[a_] := Exp[-(Log[a] - Log[step])^2/2/Log[σ1]^2]/Sqrt[2π]/a/Log[σ1];
          Do[s1[i] = Sum[size1[j], {j, i-2, i+2, 1}], {i, 5, 1200, 5}];
          mielist = Append[mielist, {step, Sum[s1[l]*ext[[l/5]], {l, 5, 1200, 5}]}], {step, 5, 1200, 5}]

In[49]:=
         ListPlot[{mielist}, PlotRange→{{0, 1000}, {0, 1.8}}]
```

Out[49]=

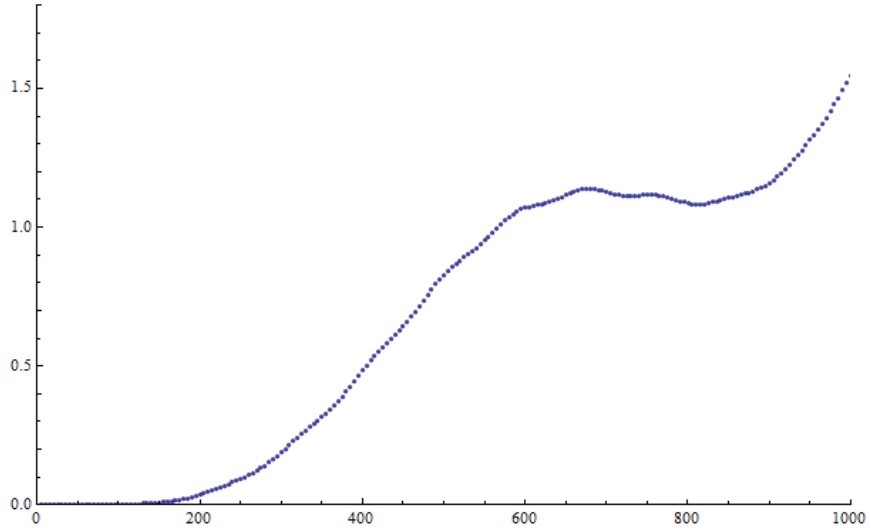

Figure A.1. Log-normal distribution script. The graph plots effective cross section given a specific complex refractive index and geometric standard deviation of particle diameters.

A.2. Calibration parameter retrieval

The three calibration parameters are retrieved with the Mathematica script shown below. Note that the range in n and k for squalane is ±0.002 and 0.000i, respectively. The range and incremental step for the three parameters are normally selected such that a course evaluation is conducted followed by a precise evaluation. The output will show the first combination of parameters with $\chi^2 < 1000$, and each subsequent parameter set that has a lower χ^2.

Squalane Calibration with CRD

Set Path for Importing Mie files (λ = 355 nm)

In[1]:=
```
Off[General::spell1];
SetDirectory["C:/New Mie files"]
```

Out[2]=
```
C:\New Mie files
```

Read in CRD Measured Cross Sections

Reads in a CSV file containing: nominal particle size selected with electrostatic classifier (in nm), CRD measured cross section (in μm^2), error estimate on cross section (in μm^2) (95% confidence interval, calculated from standard deviation of 1-second cross section measurements)

It is assumed that the cross sections have been calculated using the R_L value obtained from cell length measurements.

In[3]:=
```
filein = "Squalane_11_22B";
data = Import[filein <> ".csv"];
ns = Length[data];
Do[d[i] = data[[i, 1]]; cs[i] = data[[i, 2]] * 10^8; e[i] = data[[i, 3]] * 10^8, {i, 1, ns}]
Do[Print[d[i], " ", cs[i], " ", e[i]], {i, 1, ns}]
```

```
650 1.18059 0.00592
680 1.16122 0.00777
710 1.14068 0.0074
740 1.13602 0.00611
770 1.11528 0.00796
800 1.10341 0.00703
830 1.12798 0.00787
870 1.19466 0.00926
900 1.23653 0.00926
```

Define log - normal size distribution function

In[8]:=
```
size[dia_, gsd_, a_] := Exp[-(Log[a] - Log[dia])^2 / 2 / Log[gsd]^2] / Sqrt[2 π] / a / Log[gsd]
```

Define Ranges for Fitting

Parameters for size range to integrate over.

* THESE VALUES SHOULD USUALLY NOT BE CHANGED *

lowerd = 1 and upperd = 240 will include all sizes tabulated in the Mie files. step = 5 indicates a step size of 5 nm (this should not be altered).

In[9]:=
```
lowerd = 1;
upperd = 240;
step = 5;
```

Parameters for scanning over real part of index of refraction

* THESE VALUES SHOULD USUALLY NOT BE CHANGED *

minimum value = 1400 (i.e. n = 1.400), maximum value = 1700 (i.e. n = 1.700)

nstep must be an integer

In[12]:=
```
nlower = 1470;
nupper = 1474;
nstep = 5;
```

Parameters for scanning over imaginary part of index of refraction

* THESE VALUES SHOULD USUALLY NOT BE CHANGED *

minimum value = 0 (i.e. k = 0.000), maximum value = 200 (i.e. k = 0.200)

for k <= 0.050, kstep must be an integer

for k > 0.050, kstep must be a multiple of 10 (i.e. steps of 0.010 in k)

In[15]:=
```
klower = 0;
kupper = 0;
kstep = 1;
```

Parameters for scanning over correction to particle size selected with the electrostatic classifier (i.e. Δd)

This value is added to the particle diameter. It accounts for mis-calibration of the electrostatic classifier.

minimum value = -50, maximum value = 50

initial values should be: delatdlower = -50, deltadupper = 50, deltadstep = 10

In[90]:=
```
deltadlower = 10;
deltadupper = 30;
deltadstep = 2;
```

Parameters for scanning over correction to cross section measured with CRD (i.e. c)

This value multiplies the measured cross section directly. It accounts for uncertainty in R_L, CPC particle counting efficiency and possible particle loss within or after the CRD cell.

initial values should be: clower = 0.800, cupper = 1.200, cstep = 0.050

In[83]:=
```
clower = 0.960;
cupper = 0.984;
cstep = 0.002;
```

Parameters for scanning over geometric standard deviation (i.e. gsd)

This value is used in calculating the log-normal distribution of particle diameters in order to calculate a weighted cross section.

minimum value = 1.020, maximum value = 1.090

initial values should be: gsdlower = 1.020, gsdupper = 1.090, gsdstep = 0.010

In[86]:=
```
gsdlower = 1.030;
gsdupper = 1.054;
gsdstep = 0.002;
```

Loop Over Values of c, Δd, gsd to Minimize χ^2

Uncertainty in n is propagated in the χ^2 minimization by calculating the difference in the Mie cross section over the range of n. This difference is stored in diffext and used with the given size distribution to calculate an uncertainty on the Mie cross section.

As the values of gsd, Δd and c are stepped through, any fit that is better than all previous fits will be displayed. Initially, poor fits will be displayed, but as the scanning is carried out better and better fits will emerge.

At the end of the steps, the minimum χ^2 and best fit values of gsd, Δd and c are displayed. 95% confidence intervals are also shown (in parentheses) for gsd, Δd and c.

In[89]:=
```
outlist = {};
temp = 0;
best = 1000;
bestm = 1;

steps = (gsdupper - gsdlower) / gsdstep *
    (cupper - clower) / cstep * (deltadupper - deltadlower) / deltadstep;
Print["Number of steps: ", steps, "     Estimated time: ", steps * 0.03, " seconds"]

diffext = Abs[(Import["n" <> ToString[nupper, FormatType → TextForm] <> "k0", "Table"] -
       Import["n" <> ToString[nlower, FormatType → TextForm] <> "k0", "Table"])] / 2.;

time = Timing[
   Do[
    infile = "n" <> ToString[n, FormatType → TextForm] <> "k" <>
      ToString[j, FormatType → TextForm] ; ext = Import[infile, "Table"];
    Do[Print["*** gsd = ", k, " ***"];
     Do[
      size2 = Table[Table[size[d[j] + deltad, k, i], {i, 5, 1200, 5}], {j, 1, ns}];
      Do[
       Do[
        temp = temp + (Sum[size2[[p]][[l]] * ext[[l]],
                {l, lowerd, upperd, 1}] * step - cs[p] * c) ^ 2 / ((e[p] * c) ^ 2 +
              (Sum[size2[[p]][[l]] * diffext[[l]], {l, lowerd, upperd, 1}] * step) ^ 2),
        {p, 1, ns}];
       sumsq = temp[[1]]; temp = 0; outlist = Append[outlist, {k, c, deltad, sumsq}];
       best = If[sumsq < best, sumsq, best];
       bestm = If[sumsq == best, (n * 10^-3 + I j * 10^-3), bestm];
       If[sumsq == best, Print["gsd: ", k, "    c: ", c, "    Δd: ", deltad, "    χ²: ",
```

```
          best]; gsdbest = k; cbest = c; deltadbest = deltad],
        {c, clower, cupper, cstep}],
       {deltad, deltadlower, deltadupper, deltadstep}],
      {k, gsdlower, gsdupper, gsdstep}],
     {n, IntegerPart[(nupper + nlower) / 2], IntegerPart[(nupper + nlower) / 2], nstep},
     {j, IntegerPart[(kupper + klower) / 2], IntegerPart[(kupper + klower) / 2], kstep}]];

outfile = "fit.csv";
Export[outfile, outlist]
fitlist = {};
fitlistgsd = {};
fitlistc = {};
fitlistdeltad = {};
Do[If[outlist[[i]][[4]] < best + 3.84, fitlist = Append[fitlist, outlist[[i]]];
   fitlistgsd = Append[fitlistgsd, outlist[[i]][[1]]];
   fitlistc = Append[fitlistc, outlist[[i]][[2]]]; fitlistdeltad =
    Append[fitlistdeltad, outlist[[i]][[3]]], ""], {i, 1, Length[outlist]}];
Print["χmin²: ", best]
Print["gsd: ", gsdbest, "   (", Min[fitlistgsd], " - ", Max[fitlistgsd], ")"]
Print["c: ", cbest, "   (", Min[fitlistc], " - ", Max[fitlistc], ")"]
Print["deltad: ", deltadbest, "   (",
 Min[fitlistdeltad], " - ", Max[fitlistdeltad], ")"]
Print["Number of steps: ", steps, "    Time: ", time[[1]],
 " seconds      Time/step: ", time[[1]] / steps, " seconds"]
Export[filein <> "_fitdata.csv", Table[{d[i] + deltadbest, cs[i] * cbest}, {i, 1, ns}]]
```

```
Number of steps: 1440.     Estimated time: 43.2 seconds

*** gsd = 1.03 ***

gsd: 1.03   c: 0.96   Δd: 10   χ²: 36.5061

gsd: 1.03   c: 0.962   Δd: 10   χ²: 34.277

gsd: 1.03   c: 0.964   Δd: 10   χ²: 32.829

gsd: 1.03   c: 0.966   Δd: 10   χ²: 32.158

gsd: 1.03   c: 0.962   Δd: 12   χ²: 31.3914

gsd: 1.03   c: 0.964   Δd: 12   χ²: 29.5026

gsd: 1.03   c: 0.966   Δd: 12   χ²: 28.3898

gsd: 1.03   c: 0.968   Δd: 12   χ²: 28.0488

gsd: 1.03   c: 0.964   Δd: 14   χ²: 27.1047

gsd: 1.03   c: 0.966   Δd: 14   χ²: 25.555

gsd: 1.03   c: 0.968   Δd: 14   χ²: 24.776

gsd: 1.03   c: 0.97   Δd: 14   χ²: 24.7636

gsd: 1.03   c: 0.966   Δd: 16   χ²: 23.6059

gsd: 1.03   c: 0.968   Δd: 16   χ²: 22.3948

gsd: 1.03   c: 0.97   Δd: 16   χ²: 21.949
```

```
*** gsd = 1.04 ***
*** gsd = 1.042 ***
*** gsd = 1.044 ***
*** gsd = 1.046 ***
*** gsd = 1.048 ***
*** gsd = 1.05 ***
*** gsd = 1.052 ***
*** gsd = 1.054 ***
```

Out[98]= fit.csv

χ_{min}^2: 7.76774

gsd: 1.038 (1.034 - 1.048)

c: 0.974 (0.968 - 0.98)

deltad: 22 (16 - 26)

Number of steps: 1440. Time: 87.125 seconds Time/step: 0.0605035 seconds

Out[109]= Squalane_11_22B_fitdata.csv

Plot 3 - D Contour Plot of Fit Results

Plots the 95% confidence region for the fit based on 1 degree of freedom. This means that the extreme values in each of gsd, Δd and c represent the 95% confidence interval for that parameter.

If the 95% confidence region for all 3 parameters (simultaneous) is desired, then {best + 3.84} should be changed to {best + 7.81}.

In[110]:=
```
ListContourPlot3D[outlist, Contours → {best + 3.84},
 PlotRange → {{gsdlower, gsdupper}, {clower, cupper}, {deltadlower, deltadupper}}]
```

Out[110]=

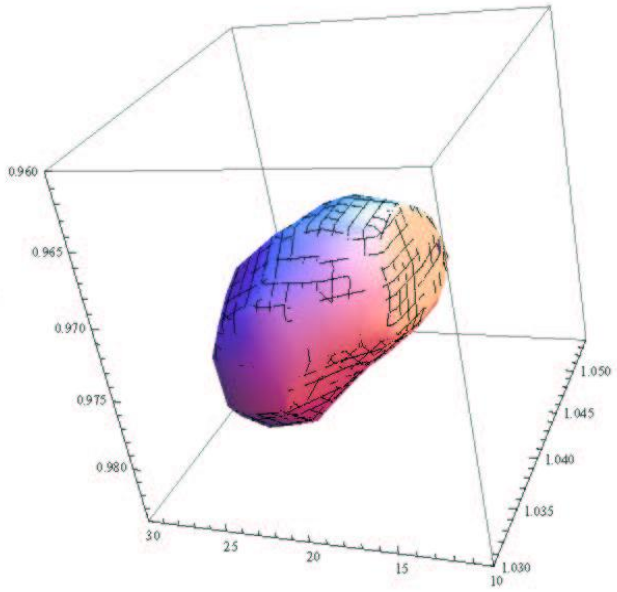

Plot Fit with Original and Adjusted Measurements

In[111]:=
```
infile = "n" <> ToString[IntegerPart[(nlower + nupper) / 2], FormatType → TextForm] <>
    "k" <> ToString[IntegerPart[(klower + kupper) / 2], FormatType → TextForm] ;
ext2 = ReadList[infile, Number];
```

Plot of Qext vs. particle diameter comparing the original measured values (closed red circles), the measured values corrected by cbest only (open red circles) and the measured values corrected by cbest and deltadbest (open blue triangles).
Also shown for comparison is the Mie calculated calculated Qext with a log-normal distribution with gsdbest (blue line).

In[113]:=
```
ext3 = Table[
    {i, 5 * Sum[ext2[[j]] * size[i, gsdbest, j * 5] * 4 * 10^6 / Pi / (j * 5)^2, {j, 1, 240, 1}]},
    {i, 5, 1200, 5}];

(* Plot Q_ext vs. particle diameter *)
Show[ListPlot[Table[{d[i], cs[i] * 4 * 10^6 / Pi / (d[i])^2}, {i, 1, ns}],
  PlotRange → {{600, 1000}, {1.8, 4}}, PlotMarkers → {"●"},
  PlotStyle → {Red, Thick, PointSize[Large]}], ListPlot[
  Table[{d[i] + deltadbest, cs[i] * cbest * 4 * 10^6 / Pi / (d[i] + deltadbest)^2}, {i, 1, ns}],
  PlotRange → {{600, 1000}, {1.5, 4}}, PlotMarkers → {"△"},
  PlotStyle → {Thick, PointSize[Large]}],
 ListPlot[Table[{d[i], cs[i] * cbest * 4 * 10^6 / Pi / (d[i])^2}, {i, 1, ns}],
  PlotRange → {{600, 1000}, {1.5, 4}}, PlotMarkers → {"⊙", 10},
  PlotStyle → {Red, Thick, PointSize[Large]}],
 ListPlot[ext3, PlotRange → {{600, 1000}, {1.5, 4}}, Joined → True]]
```

Out[114]=

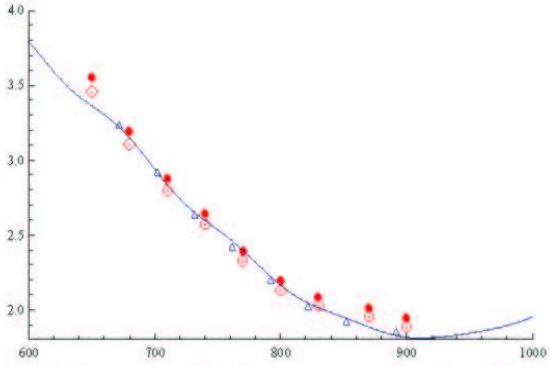

Plot of σ_{ext} vs. particle diameter comparing the original measured values (closed red circles), the measured values corrected by cbest only (open red circles) and the measured values corrected by cbest and deltadbest (open blue triangles).
Also shown for comparison is the Mie calculated calculated σ_{ext} with a log-normal distribution with gsdbest (blue line).

In[117]:=
```
ext3 =
  Table[{i, 5 * Sum[ext2[[j]] * size[i, gsdbest, j * 5], {j, 1, 240, 1}]}, {i, 5, 1200, 5}];

(* Plot σ_ext vs. particle diameter *)
Show[ListPlot[Table[{d[i], cs[i]}, {i, 1, ns}], PlotRange → {{600, 1000}, {1.0, 1.3}},
  PlotMarkers → {"●"}, PlotStyle → {Red, Thick, PointSize[Large]}], ListPlot[
  Table[{d[i] + deltadbest, cs[i] * cbest}, {i, 1, ns}], PlotRange → {{600, 1000}, {1.5, 4}},
  PlotMarkers → {"△", 10}, PlotStyle → {Thick, PointSize[Large]}],
 ListPlot[Table[{d[i], cs[i] * cbest}, {i, 1, ns}], PlotRange → {{600, 1000}, {1.5, 4}},
  PlotMarkers → {"⊙", 10}, PlotStyle → {Red, Thick, PointSize[Medium]}],
 ListPlot[ext3, PlotRange → {{600, 1000}, {0, 1.5}}, Joined → True]]
```

A.3. Complex refractive index retrieval

After the squalane calibration program is used to retrieve the best fits for C_f, Δ_{diam}, and σ_{geo} with 95% confidence limits, these values are input into the complex refractive index retrieval script. The raw data is read into the program similarly with a .csv file with the selected size in nm, the measured extinction cross section in cm^2, and the standard deviation of the cross section measurement in cm^2. These values will be converted and compared to the theoretical values with units of μm^2. The "upper" and "lower" inputs are the limits of the refractive index that will be compared to the measurements. The cerror is the larger difference with the best fit C_f and the upper and lower limits. Unlike the squalane calibration script, the χ^2 for each complex refractive index is displayed regardless of its magnitude compared to the previous evaluations. All evaluations meeting the tolerance criteria will be output at the end of the χ^2 values as {n, k, χ^2}. The total fit data file is exported as fit.csv, and it is used to plot a 2D contour map of n versus k. The outermost contour can be selected (shown here as $\chi^2 + 4$) to encompass the region of desired confidence given the two independent parameters: n and k. The final graph below shows the raw experimental data, shifted data, and the theoretical curve given a selected "infile".

Log – normal Particle Size Distribution

```
Off[General::spell1];
SetDirectory["/Users/geoffreysmith/Documents/Lab Details/New Mie files"]
```

```
/Users/geoffreysmith/Documents/Lab Details/New Mie Files
```

```
data = Import["Juice_12_15.csv"];
ns = Length[data];
Do[d[i] = data[[i, 1]]; cs[i] = data[[i, 2]] * 10^8; e[i] = data[[i, 3]] * 10^8, {i, 1, ns}]

Do[Print[d[i], " ", cs[i], " ", e[i]], {i, 1, ns}]

size[dia_, gsd_, a_] := Exp[-(Log[a] - Log[dia])^2 / 2 / Log[gsd]^2] / Sqrt[2 π] / a / Log[gsd]
size2 = Table[Table[size[d[j]][1.04][i], {i, 5, 1200, 5}], {j, 1, ns}];
```

```
625 1.06151 0.0068

650 1.05632 0.0058

675 1.02601 0.0045

700 1.01803 0.0046

730 1.03197 0.0045

810 1.09549 0.0065

830 1.1434 0.0053

850 1.18305 0.007

870 1.25518 0.0097

770 1.02744 0.0056
```

```
step = 5;
lowerd = 1;
upperd = 240;
best = 1000;
bestm = 1;
tolerance = 5;
temp = 0;

outlist = {};

lower = 1506;
upper = 1514;
nstep = 1;

klower = 0;
kupper = 10;
kstep = 1;

cbest = 0.924;
cerror = 0.009;

deltadbest = 27;
deltadlower = 14;
deltadupper = 36;
deltadsteps = 3;
deltastep = (deltadupper - deltadlower) / deltadsteps;

gsdbest = 1.036;
gsdlower = 1.025;
```

```
gsdupper = 1.047;
gsdsteps = 3;
gsdstep = (gsdupper - gsdlower) / gsdsteps;

size2 = Table[size[d[i] + deltadlower + deltastep * j, gsdlower + k * gsdstep, 1],
    {i, 1, ns}, {j, 0, gsdsteps}, {k, 0, deltadsteps}, {l, 5, 1200, 5}];

Do[ecs2[i] = (e[i] * cbest) ^2 + (cs[i] * cerror) ^2, {i, 1, ns}];

temp = 0;

outlist = {};
sumsqlist = {};

Timing[
 Do[
  infile =
   "n" <> ToString[n, FormatType → TextForm] <> "k" <> ToString[j, FormatType → TextForm] ;
  ext = Import[infile, "Table"]; Print["*** ", infile, " ***"]; sumsq = 0;
  Do[cslist = {};
   Do[
    Do[cslist = Append[cslist,
        5 * Sum[size2[[p]][[deltad]][[gsd]][[l]] * ext[[l]], {l, 80, 240, 1}]],
     {deltad, 1, deltadsteps + 1, 1}],
    {gsd, 1, gsdsteps + 1, 1}];
   mieerror = (Max[cslist] - Min[cslist]) / 2;
   sumsq +=
    4 * (cs[p] * cbest - 5 * Sum[size[d[p] + deltadbest, gsdbest, 1 * 5] * ext[[l]], {l, 80,
            240, 1}]) ^2 / (ecs2[p] + mieerror ^2),
   {p, 1, ns}]; Print[sumsq[[1]]]; outlist = Append[outlist,
    {n / 1000., j / 1000., sumsq[[1]]}],
  {n, lower, upper, nstep}, {j, klower, kupper, kstep}]]

Do[sumsqlist = Append[sumsqlist, outlist[[i]][[3]]], {i, 1, Length[outlist]}];
outfile = "fit.csv";
Export[outfile, outlist];
Do[If[sumsqlist[[i]] < Min[sumsqlist] + 4, Print[outlist[[i]]]], {i, 1, Length[sumsqlist]}]
```

```
*** n1506k0 ***

17.5973

*** n1506k1 ***

21.683

*** n1506k2 ***

27.4422

*** n1506k3 ***

34.888

*** n1506k4 ***

44.0358

*** n1506k5 ***

54.7108

*** n1506k6 ***

66.5295
```

```
*** n1514k9 ***
42.6642
*** n1514k10 ***
51.734
{27.5707, Null}
{1.509, 0., 4.32346}
{1.509, 0.001, 5.94378}
{1.51, 0., 3.02224}
{1.51, 0.001, 3.95291}
{1.51, 0.002, 6.2715}
{1.511, 0., 3.22417}
{1.511, 0.001, 3.53952}
{1.511, 0.002, 5.15869}
{1.512, 0., 4.88429}
{1.512, 0.001, 4.65665}
{1.512, 0.002, 5.65172}
```

```
best = Min[sumsqlist];
ListContourPlot[outlist, Contours → Range[best, best + 4, 0.4],
 PlotRange → {{lower / 1000, upper / 1000}, {0, 0.003}},
 PerformanceGoal → "Quality", PlotLabel → Squalane]
```

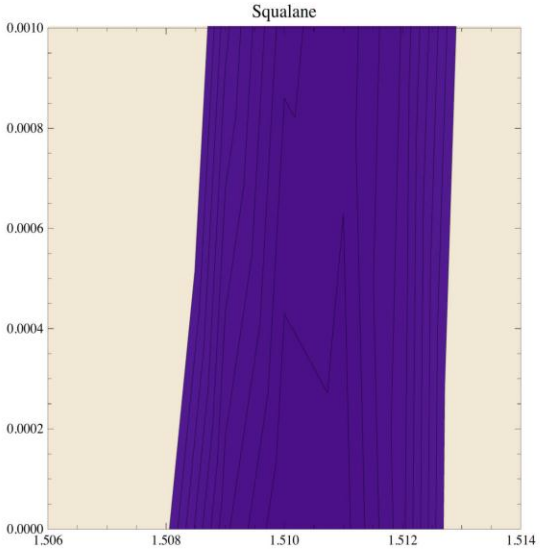

```
infile = "n1513k2"; (* index of refraction file to be used for reference compound *)
ext2 = ReadList[infile, Number];

ext3 = Table[
    {i, 5 * Sum[ext2[[j]] * size[i, gsdbest, j * 5] * 4 * 10^6 / Pi / (j * 5)^2, {j, 1, 240, 1}]},
    {i, 5, 1200, 5}];

(* Plot Q_ext vs. particle diameter *)
Show[ListPlot[Table[{d[i], cs[i] * 4 * 10^6 / Pi / (d[i])^2}, {i, 1, ns}],
  PlotRange → {{600, 1000}, {1.5, 4}}, PlotMarkers → {"●"},
  PlotStyle → {Red, Thick, PointSize[Large]}], ListPlot[
  Table[{d[i] + deltadbest, cs[i] * cbest * 4 * 10^6 / Pi / (d[i] + deltadbest)^2}, {i, 1, ns}],
  PlotRange → {{600, 1000}, {1.5, 4}}, PlotMarkers → {"△"},
  PlotStyle → {Thick, PointSize[Large]}],
 ListPlot[ext3, PlotRange → {{600, 1000}, {1.5, 4}}, Joined → True]]

(* Plot extinction cross section in micron^2/particle vs. particle diameter *)
(* Show[ListPlot[Table[{d[i],cs[i]},{i,1,ns}],PlotRange→{{600,1000},{0,1.5}},
  PlotMarkers→{"●"},PlotStyle→{Red,Thick,PointSize[Large]}],
 ListPlot[Table[{d[i]-deltad,cs[i]},{i,1,ns}],PlotRange→{{600,1000},{0,1.5}},
  PlotMarkers→{"△"},PlotStyle→{Thick,PointSize[Large]}],
 Plot[fext2[x],{x,600,1000},PlotRange→{{600,1000},{0,1.5}}]] *)
```

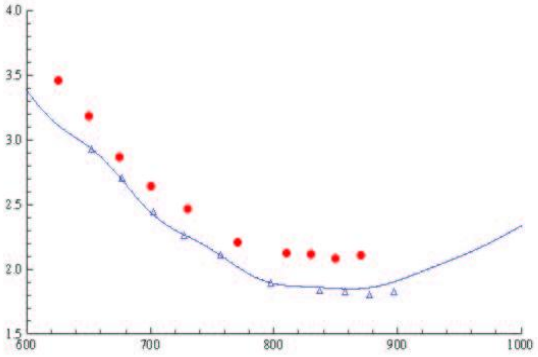

APPENDIX B

LABVIEW PROGRAMS

B.1. The primary A-CRDS σ_{ext} program

All the intricacies involved in the programming of the current VI cannot be addressed in a reasonable amount of time. The evolution of the current program spans several programmers and varies considerably since its inception in 2009. In lieu of pages of descriptions, the key features of the front panel are described to allow a new user to make aerosol cross section measurements without needing to trace every control and indicator. The front panel is divided into three sections: the primary control panel, real-time recording of τ and particle concentration, and extinction cross section calculation.

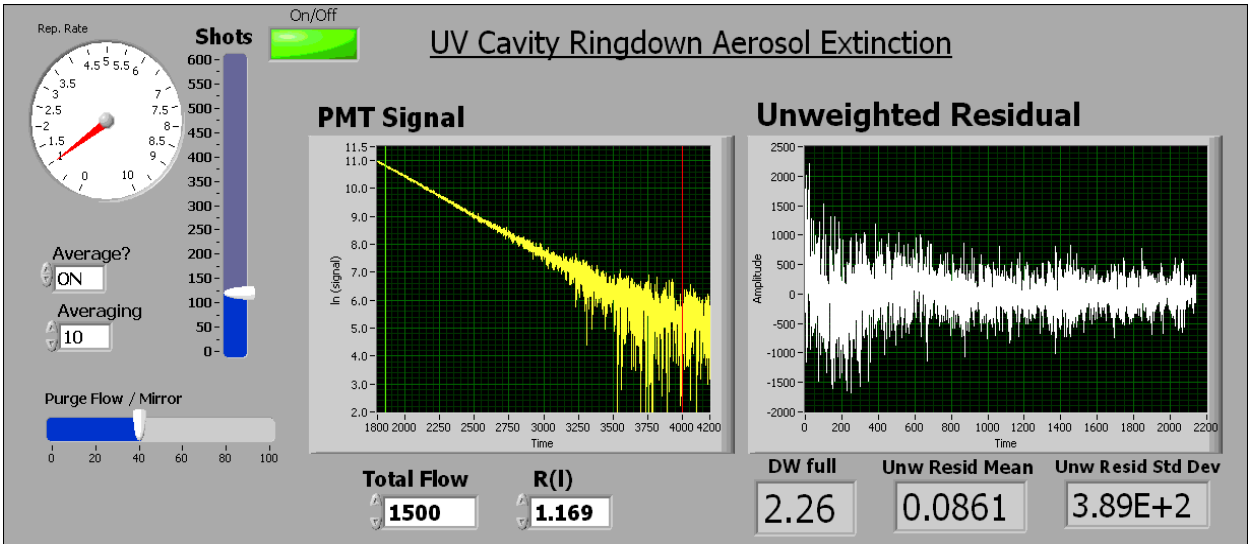

Figure B.1. Primary control panel.

The repetition rate is calculated based on the frequency of the of the laser pulse (10 Hz) and the amount of averaging of the ring-down transients. As shown, a 1 Hz "Rep. Rate" corresponds to

a 1 second average of 10 exponential decays. This is reflected in the "Average?" and "Averaging" controls. The number of "Shots" is actually the number of total averaged decay, so the figure calculates the extinction for a total of 120 one second measurements. The "PMT Signal" graph displays the ln of the PMT signal versus time (where time is actually in units based on the sampling rate). The intensity between the green and red bars is the user-selected fitting region. The purge flow and total flow controls are used to calculate an effective particle concentration inside the cavity. The graph of the residual shows the residual for each point for the fitted region, and this is a useful first-order measure of how monoexponential the fit decay is. Another useful statistical parameter that quantitatively describes the goodness-of-fit is DW (Durbin-Watson statistic). DW is discussed in further detail in Appendix C.

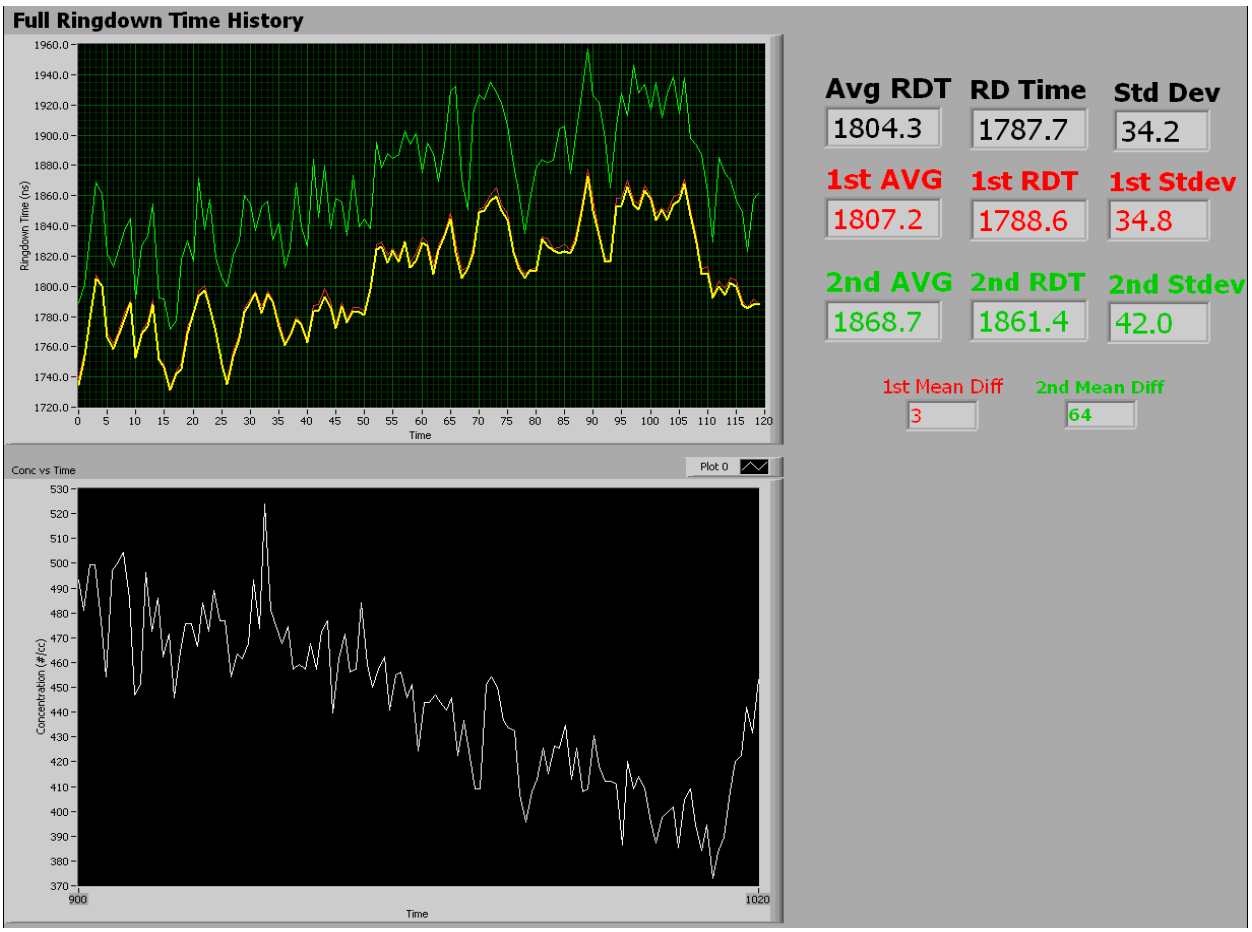

Figure B.2. Real-time recording of τ and the particle concentration.

The two graphs shows in Figure B.2. display the most recent 120 one-second measurements (or whatever shot count is selected). In this way, the averages are actually moving averages and can be recorded consecutively for a final cross section measurement. In the example ring-down time history, three lines are plotted for three distinct fitting regions. The yellow line is the full fit region (between the green and red bars in the PMT Signal graph), and the other two lines are sub-regions. Note that the "2nd AVG" is 60 ns longer than the normal fit region. This difference should not be as concerning as the difference in the measured extinction cross sections. Finally, the extinction should be inversely related to the particle concentration, and this in realized in the figure. However, and the importance cannot be overstated, a consistent particle concentration is necessary for an accurate cross section calculation. An upward or downward trend in the particle concentration will skew the cross section by several percent.

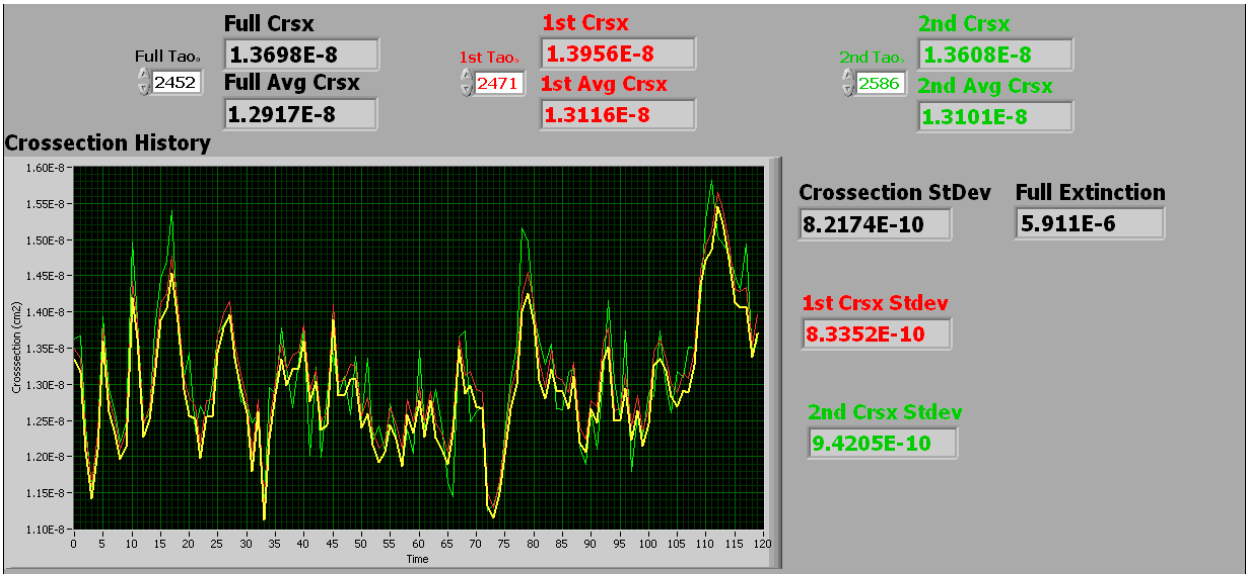

Figure B.3. Real-time extinction cross section measurement.

Lastly, the ratio of the extinction and concentration is calculated for each one second measurement and plotted similarly over the two minute interval. Once again, the different fit

regions are displayed as distinct traces and these will be identical for a perfectly monoexponential decay. The τ_o is input prior to each measurement ("Full Tao", "1st Tao", "2nd Tao") by taking the same 120 second measurement with a particle-free nitrogen flow.

B.2. Block diagrams of developed sub-VIs

The following figures depict the additional sub-Vis within the primary extinction program. First the oscilloscope must be configured prior to running the extinction calculation loop, and this requires standard interfacing commands. In addition, the user might desire to change some adjustable controls such as the averaging, sampling rate, or voltage scale. These controls have been consolidated into the Config Scope.vi, and the controls will be updated each time the program is started. These controls are fed through to the front panel of the primary program.

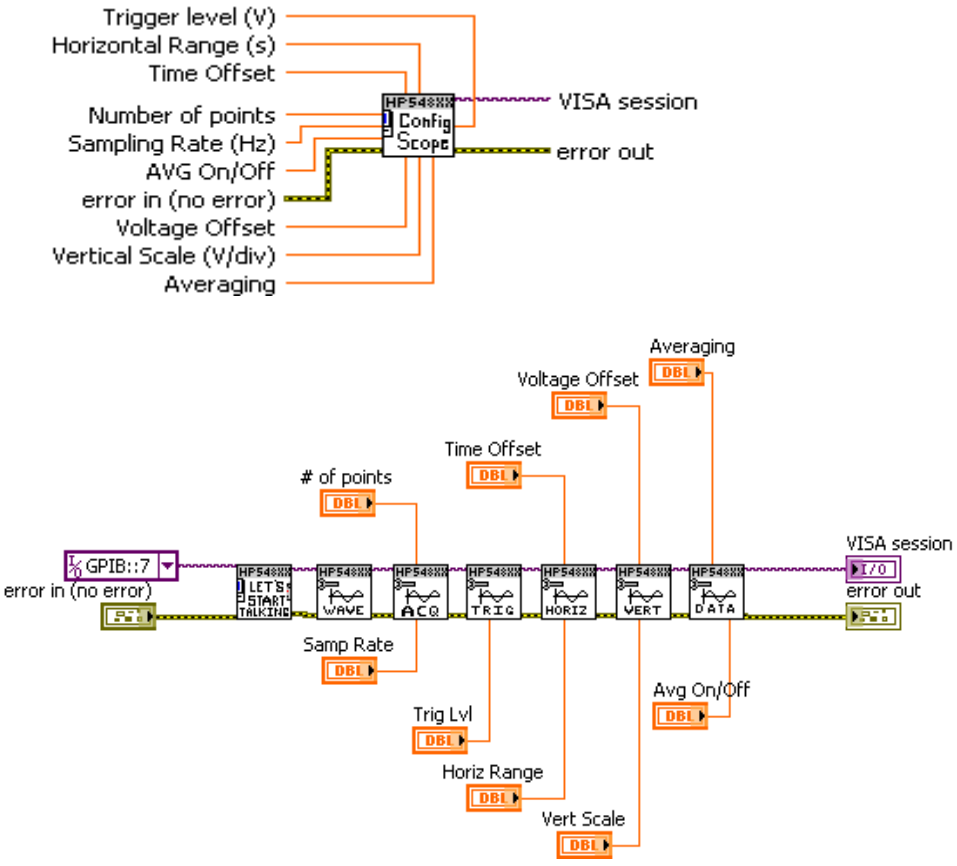

Figure B.4. Config Scope.vi terminal connector pane and block diagram.

The PMT current is converted into a voltage signal that is measured by the oscilloscope. The voltage versus time trace must be digitized by the oscilloscope, and this is achieved by "Get Waveform2.0.vi". The output array is a 2D Array with the digitized data that is used for the exponential fitting algorithm (LRS).

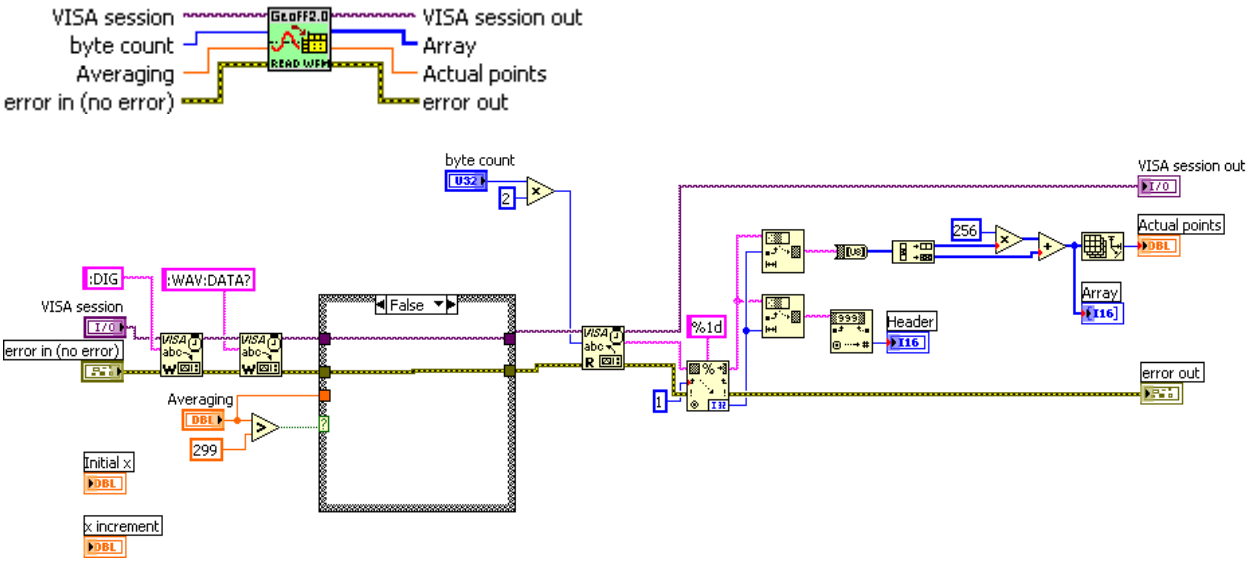

Figure B.5. Get Waveform2.0.vi terminal connector pane and block diagram.

The calculation of the extinction cross section is performed by the "Extinction consolidation1.vi". Using Equations 2.3 and 2.4, the τ and N are measured every second so that a σ_{ext} is calculated accordingly. The 1E-9 converts the ring-down times into seconds, R_l should be 1.169, and the speed of light (in nitrogen gas) is in units of cm/s. The concentration reading of the CPC is modified slightly to account for the dilution of the small mirror purge flow.

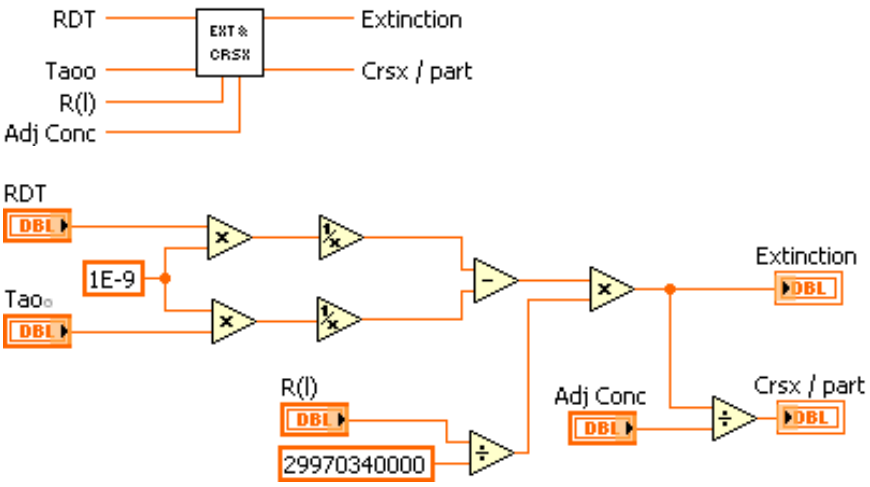

Figure B.6. Extinction consolidation1.vi terminal connector pane and block diagram.

One of the most troubling problems with programming the primary extinction calculation program was interfacing with the DMA and CPC. The standard DB-9 serial connections used with each instrument can be tested with hyperterminal software available in WindowsXP. For most issues with serial commands or functionality, the reader is refered to the manuals for each instrument. In terms of programing with LabVIEW, the critical step was including a termination character node along the VISA thread and completing commands with a carriage return. Once configured, the stand-alone sub-VI can be used by writing a single string (input) and the read buffer will be displayed (output). The DMA output was modified to allow the user to select up to three outputs for a given Write/Read command. This is important as the primary input "RMV" will output 21 comma-delimited responses. The "Index X" will output a "Read X" corresponding to the Xth output for the RMV command.

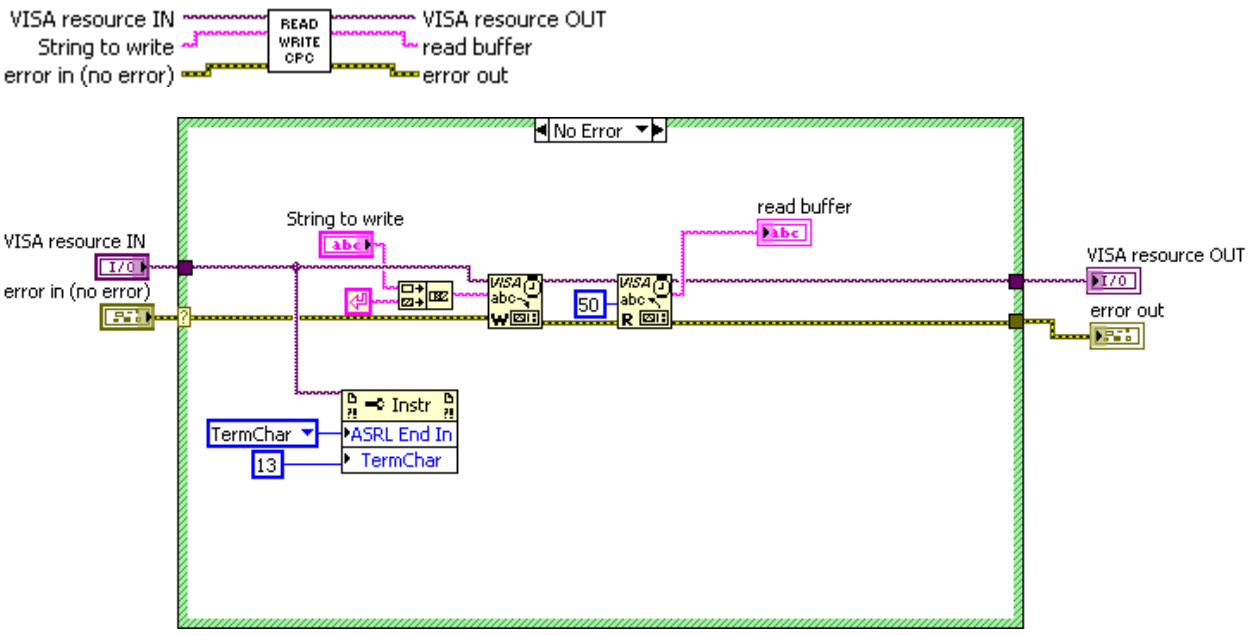

Figure B.7. Final CPC Read Write.vi terminal connector pane and block diagram.

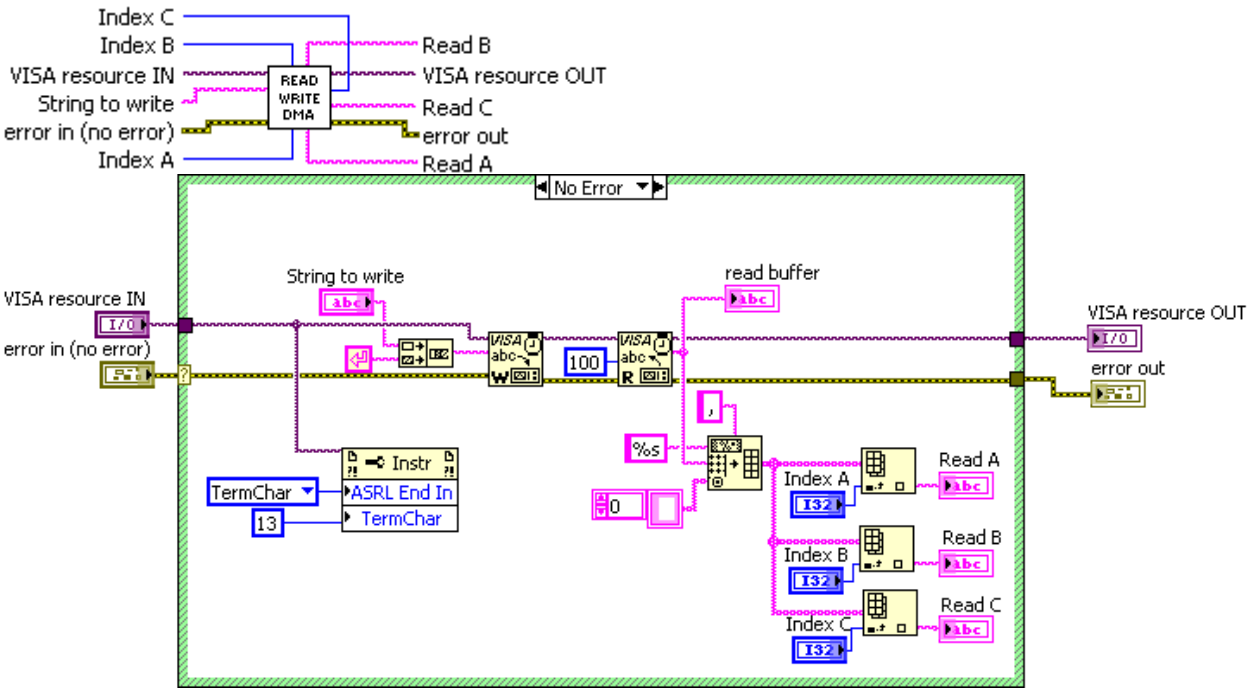

Figure B.8. Final DMA Read Write.vi terminal connector pane and block diagram.

By placing these sub-VIs in a continuous loop, the output is collected every second. The only additional input for the DMA is the command "SPD" to set the desired particle diameter. This is also inside the continuous loop so that any time the value changes the command is sent.

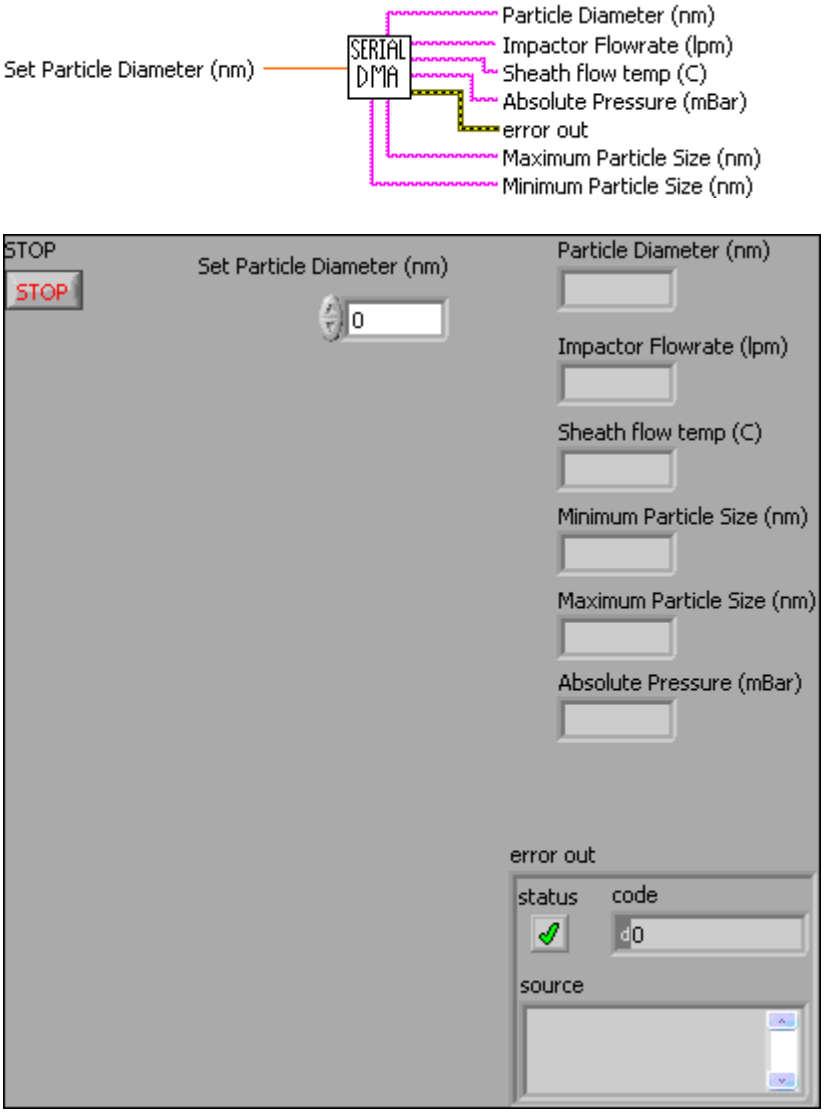

Figure B.9. Serial DMA.vi terminal connector pane and block diagram.

APPENDIX C

CRD LESSONS LEARNED

C.1. Aligning the CRD system

The CRD mirrors and optics should not normally be moved in any way between measurements; however, if the monoexponentiality of the optical cavity is compromised, adjustments must be made to ensure a proper decay transient. If necessary, the mirrors are adjusted daily prior to any measurements, though this may take an additional hour until the ring-down time settles. If the entire system needs to be re-aligned the following disassembly and assembly procedures are recommended.

Disassembly procedures:

1. Stop the LabVIEW program. Turn off laser. Turn off PMT and secure it with the magnetic mount away from the cavity.
2. Remove the top black mounting brackets and remove the magnetic mount holding the pronged base for the mounting brackets. [Stop here if simple mirror re-allignment is desired].
3. Remove the 1000μm aperture, spatial filter, and all other optics from the laser path.

Assembly and alignment procedures:

1. Using the long pulse (LP) setting on the laser, fire individual shots from the laser to line up the first wedged window inside the box. Ensure the beam dump is situated to absorb the light that passes through the wedged window (WW).

2. Roughly align the second WW so that the reflected portion of the beam is sent down field toward the CRD cell.
3. Emplace the UV filter in between the two WW and lock down the mounts securely.
4. Select Q-Switch and fire the laser to observe that there is no clipping of the beam on the cardboard shielding box and the optics. Level the beam by adjusting the WW. Mark the beam spot at the furthest possible distance downfield. Turn off the laser.
5. Emplace the spatial filter in the beam path. The focusing and collimating lenses should be placed according at their focal length from the pinhole aperture. With the assistance of someone else, fire single shots of the laser and observe the beam. Use the "Tuxedo Man" hanging alignment tool on the rail of the telescope to line up the beam. Also, a small piece of white paper glued to a long Q-tip will allow you to trace the focused beam path. DO NOT FIRE THE LASER UNTIL THE APERTURE IS ALIGNED. The aperture will be ablated if it is not centered on the most intense portion of the beam. A half-turn on the x and y-axis control knobs will move the aperture across the entire focused beam spot.
6. Adjust the magnetic base to ensure the beam is aligned as close as possible to the original beam spot downfield. Adjust the collimating lens if the beam spot is too large (i.e. diverging). Minor adjustments are required to get the best beam spot, and this is important because the spatial filter should never be moved/adjusted after the cavity is aligned.
7. Mark the entire beam spot in front of the cavity. Emplace the final 1000μm aperture on the adjustable track mount and secure the mount once the center of the beam is selected. The power meter can be used here to aid in centered the beam. The highest intensity is

measured when the aperture is centered on the beam. Also, the beam spot downfield should be aligned to the final marking after the spatial filter was locked down.

8. Carefully adjust the cavity mounts so that the front and rear openings are centered on the beam. The ¼" Teflon plugs do not offer much leeway. A useful tool is a piece of white paper with crosshairs and a dark circle marking of equivalent diameter of the cavity port. The center of the cavity should be at the crosshairs if the circle is aligned with the port. With a small hole at the center of the crosshairs, this tool can be used to align a back-reflection. Lock down the mounts. For safety reasons, be sure to turn the laser off before emplacing any optics in the beam's path.
9. Adjust the three micrometer screws on the mirror mount so that it feels like there is equal tension on each knob, and they are snug. Do not over-tighten the knobs, but they should be firm against the mirror.
10. Emplace the neutral density filter (NDF) to control the intensity of the beam spot. By turning off the overhead lights and cutting the beam with the NDF, a barely visible beam will be much easier to center, but the back-reflection is sharper at higher intensities. Use the NDF throughout the alignment procedure to make this process easier.
11. Attach the rear mirror mount to the cavity port. Use the cross hair paper to observe the back-reflection of the beam. Secure the mirror mount with its independent magnetic base and tighten the brackets. At this time it is possible to place the mirror roughly normal to the incident beam by observing its back-reflection near the 1000μm aperture. Instead of moving the screws, adjust the mounting brackets so that the back-reflection appears to be close to the incident beam. This does not need to be perfect as the screws can be used for minor adjustments. Firmly secure all mounts. With the help of someone else, closely

observe and align the back-reflection. Be aware that internal reflections inside the cavity appear similar to the true beam spot, but they will change shape as the mirror is adjusted. The true back-reflection will not change shape when moved, responds appropriately to the screw adjustments (e.g. goes down when the top of the mirror is pushed inward), and sometimes has a dark halo indicative of the shadow of the Telfon plugs.

12. As before, mount the front mirror securely and tighten all mounts when the back-reflection is roughly aligned. Make final adjustments to the front mirror with the micrometer screws.
13. Place the NDF in between the final aperture and the front mirror. The energy/pulse at the first mirror should be <15μJ / pulse with a PMT bias of -1100V.
14. Once the CRD LabVIEW program is running, the oscilloscope trace will often show a small intensity "dip" after the laser is triggered (normally at 1-2μs on the trace display). That is, the cavity is not resonating, but the alignment was good enough to create a multi-pass cell. Alignment is trivial if this small peak is observed. Slowly rotate the micrometer screws while watching the dip intensify. If this is not seen after Step 13, be careful when rotating the adjustment knobs. It is recommended to turn one knob at a time *and return to the approximate starting position* if the dip is not observed. In this way, you will not be completely blind to the original alignment position.

C.2. PMT voltage

The voltage bias for the PMT was always set to -1100V because this appeared to be an optimal region for the measured decay transient(Lab Book#1, pg 14-16, 18January2011). If the voltage bias was too low (> -900V) the RDT would be high but the shot-to-shot σ_τ would be

nearly twice as large as measured at -1100V. On the other hand, a bias too large (< -1400V) would also lead to a larger σ_τ as well as a shorter PMT lifespan.

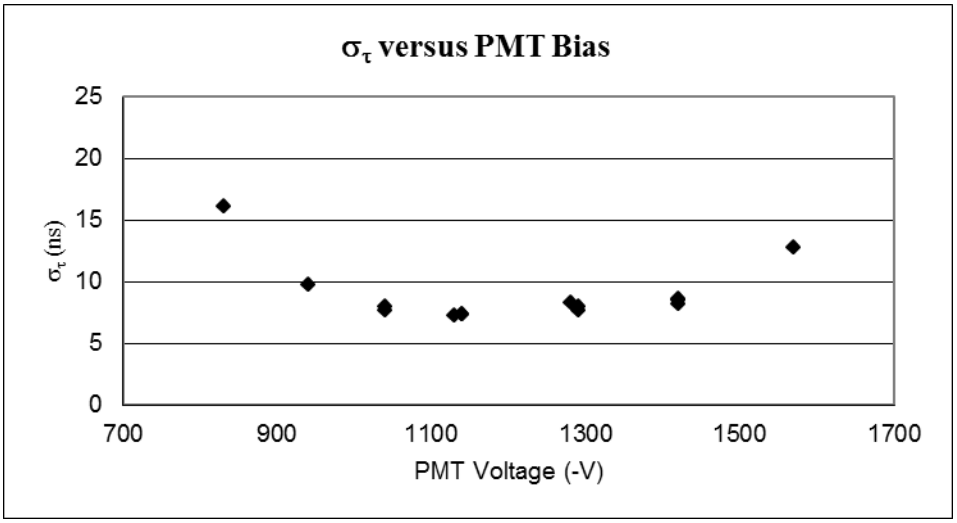

Figure C.1. Effect of varying the PMT bias voltage on the standard deviation of the RDT.

C.3. Goodness-of-fit and statistical measures

A complete discussion on the fitting of the exponential decay is available in Lab Book#1 (pg 50-61, 22March – 8April 2011), and the investigator is directed to the previously referenced articles by Halmer, Naus, Everest, and Istratov for a more complete discussion. A few lessons learned in fitting our decay transient will be briefly discussed here. First, oscillations with a period of ≈36 ns (27.1 MHz) will normally be observed through a concurrent FFT of the ring-down decay. Longer decay averaging times will increase the effect of oscillating noises. This particular 36 ns "mode beating" will also intensify and diminish according to the PMT orientation and mirror alignment. One simple rule of thumb is that the red wire (positive) should be in the "up" position on the rear of the PMT to minimize this noise. Also, careful alignment with the iris in front of the PMT will reduce this noise so that it is barely seen on the FFT trace.

By reducing the iris size and shifting the PMT mount incrementally, an optimal orientation is achieved. The iris is re-opened before the decay is actually recorded for a measurement.

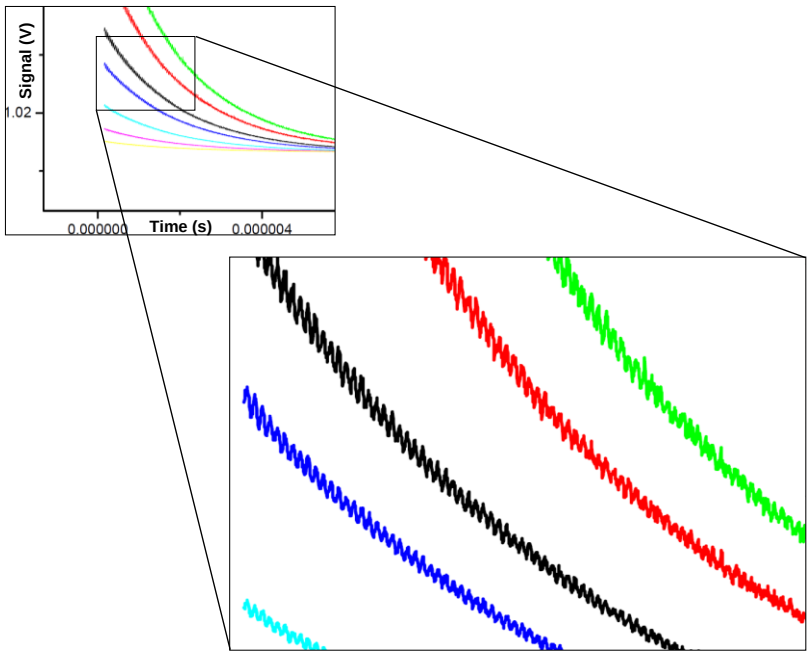

Figure C.2. 27 MHz mode beating shown for several PMT voltage biases.

Harmonics of this peak with less magnitude are visible in the FFT trace as well. This noise is attributed to the transit time of the complete laser pulse. According to the laser manual, this 355nm pulse should be 8-12ns. Also, according to the Hamamatsu manual, the PMT Electron Transit Time Spread (TTS) should be 1.228 ns, but these two times do not account for the complete picture of the current being converted into a voltage at the oscilloscope. On 4 August 2011 (Book#1, pg 85), I removed one of the CRD mirrors and collected voltage data on the oscilloscope for an individual laser pulse. The entire pulse length is from approximately 96ns – 130ns (≈36ns) and depends slightly on the PMT bias.

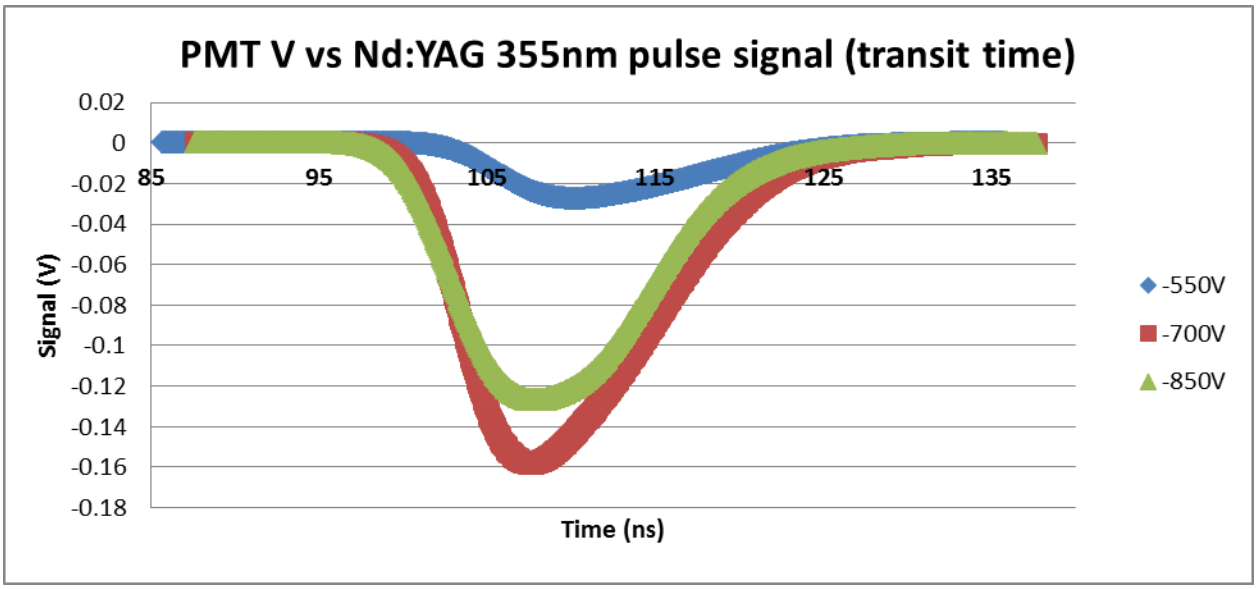

Figure C.3. Nd:YAG 355nm pulse observed on the oscilloscope.

The only other peaks in the FFT trace (i.e. noise) are the longitudinal mode of the cavity (2L/c = 145MHz) and occasionally the local radio station WUOG (90.1MHz).

Another technique in achieving a more monoexponential decay was the spatial filter. Using a FFT of an averaged decay transient and carefully selecting the TEM_{oo} mode with the final aperture allowed for less mode beating. It is important to understand that the overall alignment and beam selection was as important as the mirror alignment in reducing other transverse modes. The residual also provides a useful real-time feedback as to the overall fit. Undulations in the averaged residual will also manifest themselves by comparing the full fitting region to smaller sub-regions. In this manner, the non-exponential portions (particularly at the first 500ns of the decay) may be avoided in the fit. The fitting of the full region and two sub-regions proved to be one of the most useful techniques in monitoring the monoexponentiality of the decay *as measurements are collected.*

Alignment of the beam and preferentially selecting the TEM_{00} mode of the laser is critical in achieving the most consistent and monoexponential decay. Once the beam is aligned to the

cavity, the mirrors will be the only optics adjusted. With slight rotations of the micrometer CRD mirror screws, the ring-down time is changed substantially. When adjusting the mirrors the goal is not to achieve the highest possible τ, but rather one should optimize the alignment to achieve a single mode of resonance. In some cases, some of the statistical measures "look good" while others are "bad". In many instances a balance was struck such that the overall goodness-of-fit was presumed. Figure C.4 below demonstrates the usefulness and potential deception in using some of the recorded statistical measures. Here, the residual and "exponentiality" of each fit τ_o is taken with different average number of decays, sampling frequency, and total data points. In Figure C.4.A, 300 individual decays were averaged for each fit at 125 MSa/sec (million samples/second), and 2000 total recorded data points. Note that the residual appears to have undulations (i.e. correlation) that imply faster and slower decays for different portions of the total ring-down. This is typical and could be caused by spatial inconsistencies in the reflectivity of the mirror or by excitation of other modes. Transverse modes will, by definition, reduce the decay time, but again, this should not be the sole goal when making mirror adjustments. The exponentality trace shows the last 10 fit decays compared to the first and second half fit region. Because the residual in the second half of the decay is dropping the second half sub-region will fit a faster decay time, and this is seen with a negative "2^{nd} Exp Mean". Specifically, the full fit region has an average τ = 2101 ns, the first half region has τ_{1st} = 2131 ns (i.e. τ + 30ns), and the second half region has τ_{2nd} = 1842 ns (i.e. τ - 259ns). Therefore smaller values for the two comparison fits with the residual tell a complete story about the fit. As seen in this example, the undulations of the first half fit region are averaged such that they appear to be closer to the complete fit, yet the residual clearly indicates a non-monoexponential decay. A much more monoexponential decay is shown in Figure C.4.B. The same averaging is used, and the overall

fit and the sub-regions are much closer throughout the entire decay. Keep in mind that the 1st half exponential fit is more important than the second half fit because those points will be weighted more heavily in the fit.

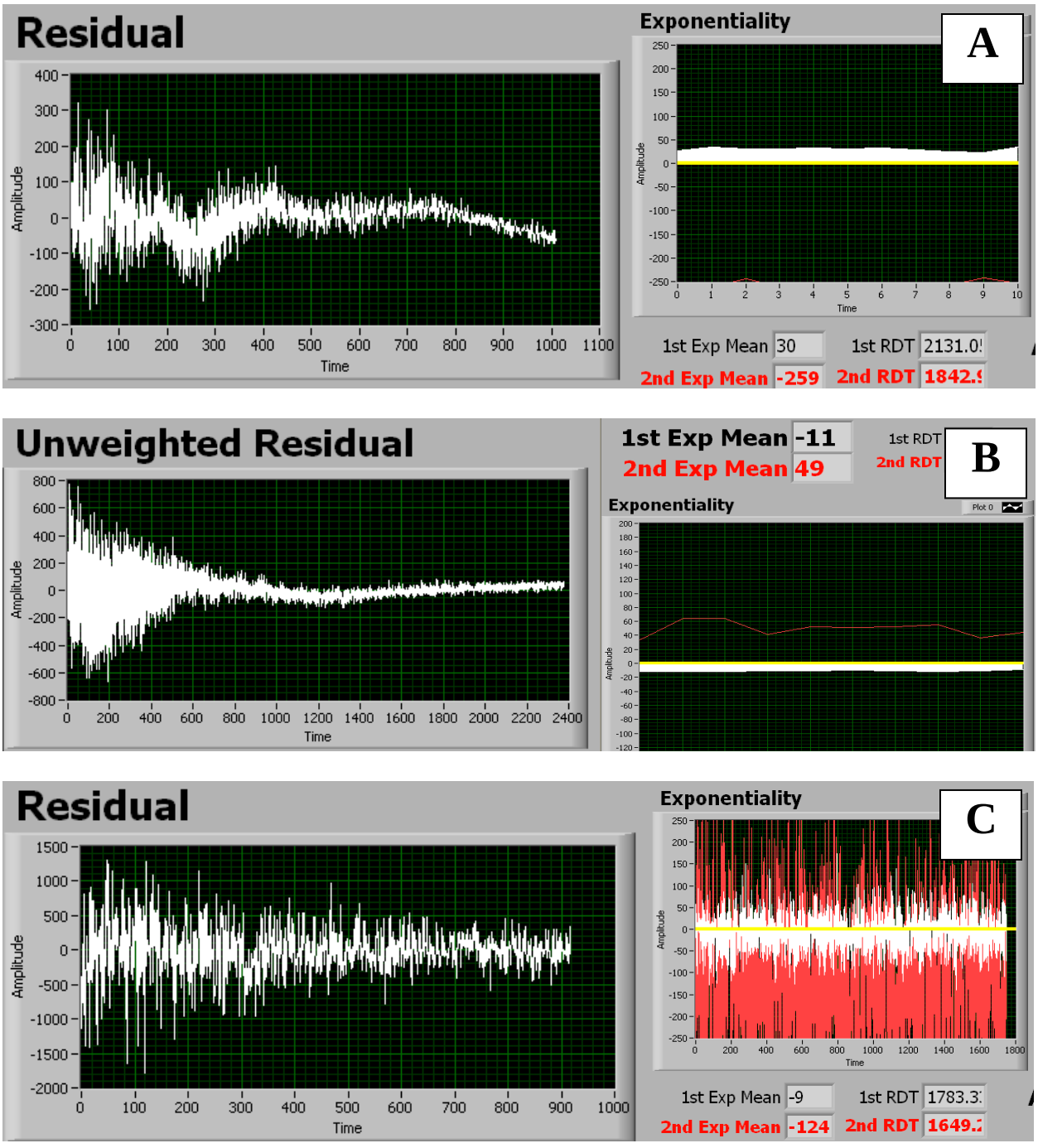

Figure C.4. Example residual and exponentiality traces.

In Figure C.4.C, only two decays are averaged which reduces the perceived undulations in the residual, but the 2nd half fit is 124 ns faster than the complete fit. This faster decay in the second half is not apparent if only the residual is used to evaluate the decay. These examples were taken for different mirror alignment and sampling rates and do not represent all possibilities. The intent is to show that the combination of several graphs and statistical measures are necessary to optimize the decay.

Finally, the Durbin-Watson (DW) statistic is used to determine the amount of correlation (sometimes referred to as autocorrelation) between measured points by comparing their residuals. A more thorough discussion of this is available in Lab Book#1 (pg53-58, 74,75, 82, and 83) and the paper by Halmer, et. al. DW is convenient in that it describes the overall correlation of measured points by assigning a single value ranging from 0 to 4 with

$$DW = \frac{\sum_{t=2}^{T}(r_t - r_{t-1})^2}{\sum_{t=1}^{T}(r_t)^2} \tag{C.1}$$

where T = total number of points, and r_t is the residual for point t. Therefore, a larger DW indicates less correlation with 4 represented anti-correlation. To make provide any statistical meaning to this value, it must be compared to a test statistic critical value. A typical benchmark is 2.0, and the fitted decay trace normally has a DW = 1.8-2.1 for a 10 shot average. The more the signal is averaged, the more pronounced the undulations of the residual are and the lower DW becomes. Because of this, this has not been as useful as merely increasing the averaging count and observing the tale-tell waviness as in Figure C.4.A. DW is most useful in determining the misalignment of the PMT and is not usually attributed to the mirror alignment.